

# Learned split-spectrum metalens for obstruction-free broadband imaging in the visible

Seungwoo Yoon<sup>1\*</sup>, Dohyun Kang<sup>2\*</sup>, Eunsue Choi<sup>1</sup>, Sohyun Lee<sup>3</sup>, Seoyeon Kim<sup>3</sup>, Minho Choi<sup>4,5</sup>, Hyeonsu Heo<sup>2</sup>, Dong-ha Shin<sup>3</sup>, Suha Kwak<sup>1</sup>, Arka Majumdar<sup>4,6</sup>, Junsuk Rho<sup>2,7,8,9,10†</sup>, Seung-Hwan Baek<sup>1†</sup>

<sup>1</sup>*Department of Computer Science and Engineering, Pohang University of Science and Technology (POSTECH), Pohang 37673, Republic of Korea*

<sup>2</sup>*Department of Mechanical Engineering, Pohang University of Science and Technology (POSTECH), Pohang 37673, Republic of Korea*

<sup>3</sup>*Graduate School of Artificial Intelligence, Pohang University of Science and Technology (POSTECH), Pohang 37673, Republic of Korea*

<sup>4</sup>*Department of Electrical and Computer Engineering, University of Washington, Seattle, 98195, WA, USA*

<sup>5</sup>*Department of Electrical Engineering, Ulsan National Institute of Science and Technology, Ulsan 44919, Republic of Korea.*

<sup>6</sup>*Department of Physics, University of Washington, Seattle, 98195, WA, USA*

<sup>7</sup>*Department of Chemical Engineering, Pohang University of Science and Technology (POSTECH), Pohang 37673, Republic of Korea*

<sup>8</sup>*Department of Electrical Engineering, Pohang University of Science and Technology (POSTECH), Pohang 37673, Republic of Korea*

<sup>9</sup>*POSCO-POSTECH-RIST Convergence Research Center for Flat Optics and Metaphotonics, Pohang 37673, Republic of Korea*

<sup>10</sup>*National Institute of Nanomaterials Technology (NINT), Pohang 37673, Republic of Korea*

*\*Equal contribution*

*†Corresponding author. E-mail: shwbaek@postech.ac.kr, jsrho@postech.ac.kr*

**Obstructions such as raindrops, fences, or dust degrade captured images, especially when mechanical cleaning is infeasible. Conventional solutions to obstructions rely on a bulky compound optics array or computational inpainting, which compromise compactness or fidelity. Metalenses composed of subwavelength meta-atoms promise compact imaging, but simultaneous achievement of broadband and obstruction-free imaging remains a challenge, since a metalens that images distant scenes across a broadband spectrum cannot properly defocus near-depth occlusions. Here, we introduce a learned split-spectrum metalens that enables broadband obstruction-free imaging. Our approach divides the spectrum of each RGB channel into pass and stop bands with multi-band spectral filtering and learns the metalens to focus light from far objects through pass bands, while filtering focused near-depth light through stop bands. This optical signal is further enhanced using a neural network. Our learned split-spectrum metalens achieves broadband and obstruction-free imaging with relative PSNR gains of 32.29% and improves object detection and semantic segmentation accuracies with absolute gains of +13.54% mAP, +48.45% IoU, and +20.35% mIoU over a**

**conventional hyperbolic design. This promises robust obstruction-free sensing and vision for space-constrained systems, such as mobile robots, drones, and endoscopes.**

Obstructions such as fences, leaves, dirt, or raindrops frequently occlude distant scenes in everyday imaging<sup>1–5</sup>. These occlusions degrade the imaging quality and reliability of downstream vision applications, especially in autonomous or compact systems where manual removal of obstacles is infeasible—for instance, cameras on drones<sup>5,6</sup>, mobile robots<sup>3,7</sup>, or endoscopes<sup>8,9</sup>. Obstruction-free imaging aims to recover distant scenes covered by near-depth obstacles. Existing computational approaches tend to hallucinate the occluded content rather than capture the true scene<sup>10–13</sup>. Optical solutions using multiple compound lenses, or synthetic apertures, can physically remove near-depth obstructions by depth-of-field control<sup>14–17</sup>. However, their bulky and costly designs hinder integration into compact imaging systems (Supplementary Note 3).

Flat diffractive optics—particularly metlenses composed of subwavelength meta-atoms—offer a promising alternative to bulky compound lenses, as ultra-thin and lightweight imaging elements<sup>18–21</sup>. Yet, achieving both broadband imaging and obstruction-free imaging with a single metlens remains fundamentally constrained by depth–wavelength symmetry; the point spread function (PSF) change induced by a wavelength shift is similar to that of an appropriate depth shift of a point light source<sup>22–27</sup>. This depth-wavelength symmetry prevents simultaneous broadband imaging and defocusing for near-depth obstructions. While hybrid diffractive-compound refractive design<sup>28,29</sup> or dispersion engineering<sup>30–35</sup> mitigate this phenomenon, bulky refractive elements negate the advantage of compactness, and dispersion control is typically restricted to micrometer-scale apertures or extremely low numerical apertures, falling short of practical imaging needs (Supplementary Note 2).

This work introduces a learned split-spectrum metlens for simultaneous obstruction-free and broadband imaging (Fig. 1). We first derive an analytical model describing the depth–wavelength symmetry in diffractive lenses. Based on this understanding, we split the spectrum of each RGB channel into pass and stop bands using a multi-band spectral filter. This spectral splitting extends the metlens design space in a depth-wavelength decoupled manner. We then computationally learn a metlens design to leverage these pass bands to focus distant scenes, while blurring near-depth obstructions via stop bands.

Our learned split-spectrum metlens achieves broadband obstruction-free imaging, yielding up to 23.90% PSNR improvement on unobstructed scenes compared to conventional hyperbolic metlenses, and 32.29% or 11.45% PSNR improvement on obstructed scenes compared to hyperbolic or learned broadband metlenses without a split-spectrum approach (broadband baseline), respectively. This capability also enhances downstream performance under obstruction, improving object detection by +13.54%/+14.12% in mAP and semantic segmentation by +48.45 %/+23.67 % in IoU, and +20.35%/+21.00% in mIoU, compared to the two baseline metlenses, underscoring the efficacy of our approach. We believe that the learned split-spectrum metlens promises robust obstruction-free imaging and perception in compact platforms such as mobile robots, drones, and

endoscopes.

## Results

**Depth-wavelength symmetry.** Let  $P_{\lambda,z}$  denote the PSF of a diffractive lens for a point light source located at depth  $z$  and wavelength of  $\lambda$ . The depth-wavelength symmetry refers to the observation<sup>23–27,36</sup> that the PSF remains invariant under a coupled shift in wavelength  $\Delta\lambda$  and depth  $\Delta z$ :

$$P_{\lambda+\Delta\lambda,z} \approx P_{\lambda,z+\Delta z}. \quad (1)$$

Here we present the first analytical model of depth-wavelength symmetry that explicitly relates the wavelength shift  $\Delta\lambda$  to the corresponding depth shift  $\Delta z$ . This model provides the theoretical foundation for the design of our learned split-spectrum metalens. We begin by considering the ideal phase profile that focuses a plane wave to a focal length  $f$  for all wavelengths  $\lambda$ . In practice, this condition is satisfied only at a design wavelength  $\lambda_d$ . For wavelengths  $\lambda > \lambda_d$ , the resulting mismatched phase can be interpreted, under the paraxial approximation, as the conjugate phase of the spherical phase of a point source located at the corresponding depth  $z$ . Consequently, if the incident light of wavelength  $\lambda$  originates from this depth  $z$  rather than infinity, its spherical wavefront counterbalances the chromatic phase mismatch, thereby yielding the sharp focus at  $f$ , as illustrated in Fig. 2a. This relationship leads to our depth-wavelength symmetry model,

$$z = \frac{\lambda_d f}{\lambda - \lambda_d}. \quad (2)$$

The complete derivation is described in Supplementary Note 1. Fig. 2b shows the focal intensity distribution of the PSFs produced by a hyperbolic metalens designed at  $\lambda_d = 450$  nm, with focal length of 4 mm and aperture diameter of 2.516 mm. Using the depth-wavelength symmetry model in Eq. (2), we overlay the predicted depth-wavelength correspondence, which shows strong agreement between the analytical prediction and the numerically observed focal behavior. We provide additional validation of the model, along with a detailed discussion on its applicability in Supplementary Notes 1 and 2.

Based on the depth-wavelength symmetry model of Eq. (2), the relationship between the wavelength shift  $\Delta\lambda$  and the depth shift  $\Delta z$  in Eq. (1) can be obtained as,

$$\Delta\lambda = \lambda_d f \left( \frac{1}{z} - \frac{1}{z - \Delta z} \right). \quad (3)$$

These expressions imply that if a metalens produces a sharp PSF for a point light source of wavelength  $\lambda$  from a far-depth  $z_{\text{far}}$ , then the PSF of a point light source corresponding to a nearer

depth  $z_{\text{near}}$  becomes similar to the far-depth PSF at a shifted wavelength  $\lambda + \Delta\lambda$ , where the shift  $\Delta\lambda$  is obtained by Eq. (3) with  $\Delta z = z_{\text{near}} - z_{\text{far}}$ .

**Design of learned split-spectrum metalens.** Obstruction-free broadband imaging requires a metalens that produces sharp PSFs for distant targets at far depth,  $z_{\text{far}}$  (typically  $z_{\text{far}} \geq 0.5$  m), while simultaneously inducing strong blur for obstructions located at near depth  $z_{\text{near}} \simeq 0.045$  m. The normally constant value of  $z_{\text{near}}$  models the prevalent scenario where obstructions adhere directly onto the optical window, such as a cover glass. Unfortunately, the depth-wavelength symmetry fundamentally limits this simultaneous far-depth sharp imaging and near-depth defocusing in the visible. If a metalens forms a sharp far-depth PSF at wavelength  $\lambda$ , the corresponding near-depth PSF at the shifted wavelength  $\lambda + \Delta\lambda$ , also becomes sharp where the wavelength shift  $\Delta\lambda$  is given by Eq. (3) with  $\Delta z = z_{\text{near}} - z_{\text{far}}$ . If this shifted wavelength  $\lambda + \Delta\lambda$  remains within the sensor's spectral response range, light from near-depth obstructions is also sharply captured, making obstruction-free imaging impossible.

To overcome this limitation, we introduce a split-spectrum design. The spectrum of each RGB channel of the sensor  $c \in \{R, G, B\}$  is divided into a high-transmission pass band  $\Lambda_{\text{pass}}^c$  and a zero-transmission stop band  $\Lambda_{\text{stop}}^c$  using a multi-band spectral filter, as illustrated in Fig. 3b,c. We design our metalens to form focused far-depth PSFs for wavelengths in  $\Lambda_{\text{pass}}^c$ . At near depth, these focused PSFs shift to wavelengths  $\lambda + \Delta\lambda$  that predominantly fall into  $\Lambda_{\text{stop}}^c$  and are therefore rejected (Fig. 3d). This spectral filtering prevents the sharp far-depth focusing behavior from transferring to the near depth, and thus we can explicitly optimize the metalens to yield strongly defocused near-depth responses over  $\Lambda_{\text{pass}}^c$ . This split-spectrum mechanism thus opens up the possibility of achieving sharp far-depth PSFs and defocused near-depth PSFs across the visible spectrum, providing a physical pathway toward obstruction-free broadband imaging. Detailed validation and the rationale for band selection are provided in Supplementary Note 1.

To find a split-spectrum metalens design that enables obstruction-free broadband imaging, we learn the metalens design map  $\theta(x, y)$ , representing the orientation of each geometric-phase meta-atom at pupil-plane coordinate  $(x, y)$  (Fig. 3a). To this end, we construct two differentiable components: (i) a differentiable PSF simulator,

$$P_z^c = f_{\text{psf}}(\theta, z, c), \quad (4)$$

which generates the PSF at depth  $z$  for a sensor color channel  $c$ , and (ii) a differentiable image simulator,

$$I_{\text{captured}} = f_{\text{img}}(\theta, I_{\text{clean}}, I_{\text{obs}}), \quad (5)$$

which synthesizes the captured RGB image from an unobstructed far-depth target image  $I_{\text{clean}}$  and a near-depth obstruction image  $I_{\text{obs}}$ . We perform importance sampling over wavelengths to reduce the computational burden of the spectral integration, using a distribution proportional to the system spectral sensitivity for each color channel  $c$ . Both  $f_{\text{psf}}$  and  $f_{\text{img}}$  are differentiable with respect to  $\theta$ ,

enabling end-to-end optimization:

$$\underset{\theta}{\text{minimize}} \mathcal{L}_{\text{img}}(I_{\text{captured}}, I_{\text{clean}}) + \mathcal{L}_{\text{psf}}(P_{z_{\text{far}}}), \quad (6)$$

where the objective function  $\mathcal{L}_{\text{img}}$  enforces similarity of  $I_{\text{captured}}$  to the target far-depth image  $I_{\text{clean}}$ , and  $\mathcal{L}_{\text{psf}}$  encourages sharp and high efficiency far-depth PSFs  $P_{z_{\text{far}}}$ . We solve Eq. (6) via a first-order optimizer using  $I_{\text{clean}}$  randomly sampled from a high-resolution image dataset DIV2K<sup>37</sup> and randomly generated obstruction images  $I_{\text{obs}}$ . Additional implementation details are provided in Supplementary Note 4.

Fig. 3e shows the training loss curve with the corresponding simulated images, demonstrating the capability of obstruction-free broadband imaging. Fig. 3d further demonstrates this by showing the  $x - \lambda$  scans of the far-depth and near-depth PSFs from the learned design, exhibiting sharp far-depth PSFs and blurry near-depth PSFs for pass-band wavelengths and the opposite behavior for stop-band wavelengths.

**Characterization of the learned split-spectrum metalens.** We employ geometric-phase anisotropic meta-atoms whose structural parameters were optimized via rigorous coupled-wave analysis to maximize conversion efficiency at the center wavelengths of the multi-band spectral filter (457 nm, 530 nm, and 628 nm). Silicon nitride ( $\text{SiN}_x$ ) is chosen as the structural material owing to its sufficiently high refractive index and low extinction coefficient across the visible spectrum (Supplementary Fig. S9). The selected geometry-period  $p = 395$  nm, height  $h = 700$  nm, width  $w = 305$  nm, and length  $l = 125$  nm—yields optimized efficiency of 78.4%, 72.9%, and 66.9% at target wavelengths (Supplementary Note 7). Furthermore, the designed meta-atoms exhibit broadband characteristics, achieving an average efficiency of 67.3% across the pass-band wavelengths (Supplementary Fig. S11)<sup>38</sup>. Based on these meta-atom characteristics, we design and fabricate three types of metalenses shown in Fig. 4b: (1) a learned split-spectrum metalens (Ours), (2) a learned broadband metalens without the split-spectrum strategy (Broadband), and (3) a hyperbolic-phase metalens designed for 532 nm (Hyperbolic). All lenses have the same configuration, with a 4 mm focal length and a 2.516 mm aperture diameter, and were fabricated using high-speed electron-beam lithography (EBL) (Fig. 4a; see Methods and Supplementary Fig. S12).

We captured near-depth and far-depth PSFs across wavelengths from 430 to 645 nm with a 5 nm step, for the three metalenses. The wavelength-dependent intensity profiles of the focal spots, normalized to the total intensity, are shown in Fig. 4c. Across the pass bands of the visible spectrum, the hyperbolic metalens suffers from incomplete broadband focusing capability as it is designed for a single wavelength. The learned broadband metalens without the split-spectrum strategy improves broadband focusing relative to the hyperbolic baseline but does not achieve simultaneous near-depth blur, thereby failing to enable obstruction-free imaging. In contrast, the learned split-spectrum metalens maintains sharp focus for far depth while blurring near depth response. The corresponding two-dimensional PSF profiles, normalized to their peak intensities, are shown in Fig. 4d. Within the pass bands highlighted by the colored boxes, our learned split-spectrum metalens produces sharp focal spots at the far depth while exhibiting strong defocus at the

near depth, confirming the effectiveness of the split-spectrum design for broadband obstruction-free imaging. More details of PSF measurement are described in the Supplementary Notes 10 and 13.

**Obstruction-free broadband imaging and vision.** We evaluate obstruction-free broadband imaging performance of the three metalenses. Fig. 5 shows both the raw sensor measurements and the reconstructed images by a neural network<sup>39</sup> trained individually for each lens. The hyperbolic-phase metalens exhibits strong chromatic aberration and visible obstruction artifacts, demonstrating its limitation in achieving broadband and obstruction-free imaging. The learned broadband metalens without the split-spectrum strategy improves broadband performance but fails to suppress near-depth obstructions that inevitably arise from the depth-wavelength symmetry. In contrast, the learned split-spectrum metalens leaves only faint obstruction traces in the raw measurements, allowing the neural network to reconstruct underlying structures reliably rather than hallucinating them. Quantitatively, the learned broadband metalens without the split-spectrum strategy attains a PSNR of 18.79 dB, corresponding to an 18.7 % improvement over the conventional hyperbolic design under obstruction. The learned split-spectrum metalens achieves a PSNR of 20.94 dB, equivalent to a 32.29 % increase, confirming the advantage of our spectrally separated design. See Supplementary Notes 5, 11, and 15 for details on the neural network, metric measurements, and additional experimental results.

We further evaluate downstream vision tasks on images captured with each fabricated metalens to assess the practical utility of obstruction-free imaging. Off-the-shelf vision models are employed without fine-tuning on our metalens-captured data to demonstrate the universality of our imaging approach. We benchmark three representative scenarios: (1) object detection<sup>40</sup> on drone-captured aerial imagery using VisDrone<sup>41</sup>, (2) semantic segmentation for medical endoscopy<sup>42</sup> on Kvasir-SEG<sup>43</sup>, and (3) semantic segmentation for autonomous driving<sup>44</sup> on Cityscapes<sup>45</sup>. As shown in Fig. 6, our learned split-spectrum metalens consistently achieves the best performance across all tasks: it attains an mAP of 0.1704 on VisDrone (vs. 0.0350/0.0292 for hyperbolic/broadband), an IoU of 0.8317 on Kvasir-SEG (vs. 0.3472/0.5950), and an mIoU of 0.6701 on Cityscapes (vs. 0.4666/0.4601) under task-specific obstruction scenarios. These results establish our learned split-spectrum metalens as a practical imaging solution for embedded and unmanned platforms such as drones, mobile robots, and endoscopic probes, where near-depth obstructions are prevalent and physical cleaning is often infeasible. We refer to Supplementary Note 12 for further details on the vision tasks.

## Discussion

This work presents a single-shot obstruction-free imaging method using a learned split-spectrum metalens. We derive an analytical model for the depth-wavelength relationship of dispersive metalenses and harness it for broadband obstruction-free imaging through split-spectrum filtering of focused near-depth lights. We learn the metalens design via a differentiable framework based on

the extended design space provided by the spectrum splitting, achieving PSNR of 20.94 dB under obstructed conditions. This corresponds to a 32.29 % or 11.45 % improvement compared to hyperbolic or learned broadband metalens without the split-spectrum strategy, respectively. Importantly, this obstruction-suppression capability does not come at the cost of the imaging performance; our system maintains high-fidelity imaging even for unobstructed scenes, achieving PSNR of 23.41 dB, which is a 23.90 % improvement over the conventional hyperbolic metalens (refer to Supplementary Note 11, 14, and 15 for detailed analysis of imaging fidelity). Furthermore, our obstruction-free imaging directly translates to robust computer vision performance; our method achieves absolute gains of +13.54 %/+14.12 % mAP, 48.45 %/23.67 % IoU, and 20.35 %/21.00 % mIoU compared to the two baseline metalenses (refer to Supplementary Note 12 for further details of the computer vision tasks).

Several avenues for future work remain. First, our analytical model for the depth-wavelength symmetry and split-spectrum strategy is also applicable to other diffractive optics applications, potentially providing a mathematical foundation to improve performance in color holography<sup>46,47</sup>, depth sensing<sup>48,49</sup>, and hyperspectral imaging<sup>27,50</sup>. Second, while we use a commercial multi-band spectral filter for high-fidelity obstruction-free broadband imaging, a promising direction is to jointly learn the metalens and a split-spectrum filter to expand the design space, improving light efficiency and reducing inter-band spectral crosstalk. Furthermore, directly optimizing the meta-atom transmittance can integrate the filtering function into a single metalens, realizing a monolithic form factor<sup>51</sup>. Third, the proposed single-cell geometric phase design features a simple structure that facilitates large-area and mass manufacturing<sup>52,53</sup>. Realizing a high-NA, mass-manufacturable obstruction-free metalens will further enhance system efficacy for low-light applications, while boosting production throughput. We anticipate that our obstruction-free broadband imaging is an important step towards robust sensing and vision, not only for unmanned systems like mobile robots, drones, and endoscopes, where manual obstruction removal is challenging, but also for applications with structure-induced occlusions, such as under-display cameras and shielded cameras.

## Methods

**Fabrication specification** A 700-nm-thick silicon nitride ( $\text{SiN}_x$ ) film was deposited on a glass substrate, pre-cleaned with deionized (DI) water, acetone, and isopropyl alcohol (IPA), using plasma-enhanced chemical vapor deposition (PECVD, BMR Technology HiDep-SC). The designed nanopattern was subsequently exposed onto a positive photoresist (ZEP 520A) using a high-speed electron beam lithography system (ELS-BODEN, ELIONIX) operated at an acceleration voltage of 50 kV and a beam current of 10 nA. The exposed nanopattern was developed in ZEP developer (ZED-N50) at 0°C for 1 minute. A 60-nm-thick chromium (Cr) layer was then deposited via electron beam evaporation (KVT, KVE-ENS4004), serving as an etching mask. The pattern was transferred into  $\text{SiN}_x$  layer by dry etching (DRM85DD, TEL) following a lift-off process. Finally, the remaining Cr mask was removed using a commercial Cr etchant (CR-7).

**Image reconstruction specifications** We adopt LocalNet<sup>39</sup> as the image reconstruction backend. High-resolution printed targets containing rich texture and color variations from the DIV2K dataset<sup>37</sup> were used to train the neural network. Obstructed scenes were captured with the metalenses, while reference ground-truth scenes (without obstructions) were acquired with a compound lens. A focal length of  $f = 8$  mm (twice that of the metalenses) was used for the ground truth captures to achieve better object space resolution<sup>54</sup>. The compound-lens captured ground-truth images serve as supervision to correct residual aberrations and remove remaining obstruction artifacts. We further incorporate positional encoding schemes<sup>55,56</sup> into the neural network<sup>39</sup> to address spatially varying aberrations. The neural networks take 946 MiB of VRAM and 41.41 milliseconds (24.15 frames per second) for the inference of  $512 \times 512$  resolution image on NVIDIA RTX 6000 Ada. The neural network can be further optimized and accelerated for edge deployment using model compression techniques, such as pruning and quantization, or by leveraging hardware accelerators, such as FPGAs and ASICs. Further details on the neural network training schemes are provided in Supplementary Note 5.

**Online content** The source code used in this study for metalens optimization and neural network training will be available via GitHub. The data used in this study will be available from the corresponding author on reasonable request.

## References

1. You, S., Tan, R. T., Kawakami, R. & Ikeuchi, K. Adherent raindrop detection and removal in video. In *Proceedings of the IEEE Conference on Computer Vision and Pattern Recognition*, 1035–1042 (2013).
2. Brophy, T. *et al.* A review of the impact of rain on camera-based perception in automated driving systems. *IEEE Access* **11**, 67040–67057 (2023).
3. Uricar, M. *et al.* Let’s get dirty: Gan based data augmentation for camera lens soiling detection in autonomous driving. In *Proceedings of the IEEE/CVF winter conference on applications of computer vision*, 766–775 (2021).
4. Liu, Y., Belkina, T., Hays, J. & Lublinerman, R. Image de-fencing. In *26th IEEE Conference on Computer Vision and Pattern Recognition, CVPR*, 26th IEEE Conference on Computer Vision and Pattern Recognition, CVPR (2008). 26th IEEE Conference on Computer Vision and Pattern Recognition, CVPR ; Conference date: 23-06-2008 Through 28-06-2008.
5. Nathan, R. J. A. A., Kurmi, I., Schedl, D. C. & Bimber, O. Through-foliage tracking with airborne optical sectioning. *Journal of Remote Sensing* (2022).
6. Chang, W., Chen, H., He, X., Chen, X. & Shen, L. Uav-rain1k: A benchmark for raindrop removal from uav aerial imagery. In *Proceedings of the IEEE/CVF Conference on Computer Vision and Pattern Recognition*, 15–22 (2024).

7. Uřičář, M., Křížek, P., Sistu, G. & Yogamani, S. Soilingnet: Soiling detection on automotive surround-view cameras. In *2019 IEEE Intelligent Transportation Systems Conference (ITSC)*, 67–72 (IEEE, 2019).
8. Nabeel, A., Al-Sabah, S. K. & Ashrafi, H. Effective cleaning of endoscopic lenses to achieve visual clarity for minimally invasive abdominopelvic surgery: a systematic review. *Surgical Endoscopy* **36**, 2382–2392 (2022).
9. Wang, C., Alaya Cheikh, F., Kaaniche, M., Beghdadi, A. & Elle, O. J. Variational based smoke removal in laparoscopic images. *Biomedical engineering online* **17**, 139 (2018).
10. Hirohashi, Y. *et al.* Removal of image obstacles for vehicle-mounted surrounding monitoring cameras by real-time video inpainting. In *Proceedings of the IEEE/CVF Conference on Computer Vision and Pattern Recognition Workshops*, 214–215 (2020).
11. Zhang, J., Fukuda, T. & Yabuki, N. Automatic object removal with obstructed façades completion using semantic segmentation and generative adversarial inpainting. *IEEE Access* **9**, 117486–117495 (2021).
12. Gupta, D., Jain, S., Tripathi, U., Chattopadhyay, P. & Wang, L. A robust and efficient image de-fencing approach using conditional generative adversarial networks. *Signal, Image and Video Processing* **15**, 297–305 (2021).
13. Hao, Z., You, S., Li, Y., Li, K. & Lu, F. Learning from synthetic photorealistic raindrop for single image raindrop removal. In *Proceedings of the IEEE/CVF International Conference on Computer Vision Workshops*, 0–0 (2019).
14. Levoy, M. *et al.* Synthetic aperture confocal imaging. *ACM Transactions on Graphics (ToG)* **23**, 825–834 (2004).
15. Joshi, N., Avidan, S., Matusik, W. & Kriegman, D. J. Synthetic aperture tracking: Tracking through occlusions. In *2007 IEEE 11th International Conference on Computer Vision*, 1–8 (IEEE, 2007).
16. Pei, Z., Chen, X. & Yang, Y.-H. All-in-focus synthetic aperture imaging using image matting. *IEEE Transactions on Circuits and Systems for Video Technology* **28**, 288–301 (2016).
17. Pei, Z. *et al.* Occluded-object 3d reconstruction using camera array synthetic aperture imaging. *Sensors* **19**, 607 (2019).
18. Chen, M. K. *et al.* Meta-lens in the sky. *IEEE Access* **10**, 46552–46557 (2022).
19. Liu, X. *et al.* Underwater binocular meta-lens. *ACS Photonics* **10**, 2382–2389 (2023).
20. Fröch, J. E. *et al.* Real time full-color imaging in a meta-optical fiber endoscope. *elight* **3**, 13 (2023).

21. Liu, X. *et al.* Stereo vision meta-lens-assisted driving vision. *ACS Photonics* **11**, 2546–2555 (2024).
22. Colburn, S., Chu, Y., Shilzerman, E. & Majumdar, A. Optical frontend for a convolutional neural network. *Applied optics* **58**, 3179–3186 (2019).
23. Fröch, J. E. *et al.* Beating spectral bandwidth limits for large aperture broadband nano-optics. *Nature communications* **16**, 3025 (2025).
24. Tan, S., Yang, F., Boominathan, V., Veeraraghavan, A. & Naik, G. V. 3d imaging using extreme dispersion in optical metasurfaces. *Acs Photonics* **8**, 1421–1429 (2021).
25. Xu, H. *et al.* A polarization-independent and broadband achromatic gallium nitride metalens based on extended depth of focus. In *Fourth International Computational Imaging Conference (CITA 2024)*, vol. 13542, 1029–1037 (SPIE, 2025).
26. Bayati, E. *et al.* Inverse designed extended depth of focus meta-optics for broadband imaging in the visible. *Nanophotonics* **11**, 2531–2540 (2022).
27. Baek, S.-H. *et al.* Single-shot hyperspectral-depth imaging with learned diffractive optics. In *Proceedings of the IEEE/CVF International Conference on Computer Vision*, 2651–2660 (2021).
28. Shi, Z. *et al.* Seeing through obstructions with diffractive cloaking. *ACM Transactions on Graphics (TOG)* **41**, 1–15 (2022).
29. Richards, C. A. *et al.* Hybrid achromatic microlenses with high numerical apertures and focusing efficiencies across the visible. *Nature communications* **14**, 3119 (2023).
30. Chen, W. T. *et al.* A broadband achromatic metalens for focusing and imaging in the visible. *Nature nanotechnology* **13**, 220–226 (2018).
31. Shrestha, S., Overvig, A. C., Lu, M., Stein, A. & Yu, N. Broadband achromatic dielectric metalenses. *Light: Science & Applications* **7**, 85 (2018).
32. Chen, W. T., Zhu, A. Y., Sisler, J., Bharwani, Z. & Capasso, F. A broadband achromatic polarization-insensitive metalens consisting of anisotropic nanostructures. *Nature communications* **10**, 355 (2019).
33. Hu, Y. *et al.* Asymptotic dispersion engineering for ultra-broadband meta-optics. *nature communications* **14**, 6649 (2023).
34. Chang, S. *et al.* Achromatic metalenses for full visible spectrum with extended group delay control via dispersion-matched layers. *Nature communications* **15**, 9627 (2024).
35. Hou, L. *et al.* High-efficiency broadband achromatic metalens in the visible. *Applied Physics Letters* **126** (2025).

36. Colburn, S., Zhan, A. & Majumdar, A. Metasurface optics for full-color computational imaging. *Science advances* **4**, eaar2114 (2018).
37. Agustsson, E. & Timofte, R. Ntire 2017 challenge on single image super-resolution: Dataset and study. In *The IEEE Conference on Computer Vision and Pattern Recognition (CVPR) Workshops* (2017).
38. Berry, M. V. Quantal phase factors accompanying adiabatic changes. *Proceedings of the Royal Society of London. A. Mathematical and Physical Sciences* **392**, 45–57 (1984).
39. Kim, W. *et al.* Paramisp: Learned forward and inverse ips using camera parameters. In *Proceedings of the IEEE/CVF Conference on Computer Vision and Pattern Recognition (CVPR)*, 26067–26076 (2024).
40. Khanam, R. & Hussain, M. Yolov11: An overview of the key architectural enhancements. *arXiv preprint arXiv:2410.17725* (2024).
41. Zhu, P. *et al.* Detection and tracking meet drones challenge. *IEEE Transactions on Pattern Analysis and Machine Intelligence* **44**, 7380–7399 (2021).
42. Zhao, X. *et al.* M2snet: Multi-scale in multi-scale subtraction network for medical image segmentation. *arxiv* 2023. *arXiv preprint arXiv:2303.10894* (2).
43. Pogorelov, K. *et al.* Kvasir: A multi-class image dataset for computer aided gastrointestinal disease detection. In *Proceedings of the 8th ACM on Multimedia Systems Conference*, 164–169 (2017).
44. Wang, W. *et al.* Internimage: Exploring large-scale vision foundation models with deformable convolutions. In *Proceedings of the IEEE/CVF conference on computer vision and pattern recognition*, 14408–14419 (2023).
45. Cordts, M. *et al.* The cityscapes dataset for semantic urban scene understanding. In *Proc. of the IEEE Conference on Computer Vision and Pattern Recognition (CVPR)* (2016).
46. Park, C., Jeon, Y. & Rho, J. 36-channel spin and wavelength co-multiplexed metasurface holography by phase-gradient inverse design. *Advanced Science* 2504634 (2025).
47. Meng, W. *et al.* Ultranarrow-linewidth wavelength-vortex metasurface holography. *Science Advances* **11**, eadt9159 (2025).
48. Shen, Z. *et al.* Monocular metasurface camera for passive single-shot 4d imaging. *Nature Communications* **14**, 1035 (2023).
49. Shen, Z., Zhao, F., Ni, Y. & Yang, Y. Extended monocular 3d imaging via the fusion of diffraction-and polarization-based depth cues. *Optica* **12**, 872–878 (2025).
50. Jeon, D. S. *et al.* Compact snapshot hyperspectral imaging with diffracted rotation (2019).

51. Lin, R., Yao, J., Wang, Z., Zhou, J. & Tsai, D. P. Resonant meta-lens in the visible. *Laser & Photonics Reviews* **19**, 2401740 (2025).
52. Kim, J. *et al.* Scalable manufacturing of high-index atomic layer–polymer hybrid metasurfaces for metaphotonics in the visible. *Nature Materials* **22**, 474–481 (2023).
53. So, S. *et al.* Multicolor and 3d holography generated by inverse-designed single-cell metasurfaces. *Advanced Materials* **35**, 2208520 (2023).
54. Engelberg, J. & Levy, U. Generalized metric for broadband flat lens performance comparison. *Nanophotonics* **11**, 3559–3574 (2022).
55. Vaswani, A. *et al.* Attention is all you need. *Advances in neural information processing systems* **30** (2017).
56. Mildenhall, B. *et al.* Nerf: Representing scenes as neural radiance fields for view synthesis. *Communications of the ACM* **65**, 99–106 (2021).

**Acknowledgements** S.-H.B. acknowledges the Institute of Information & Communications Technology Planning & Evaluation (IITP) grants (RS-2024-0045788, IITP-2026-RS-2024-00437866) and the National Research Foundation of Korea (NRF) grants (RS-2024-00438532, RS-2023-00211658), funded by the Ministry of Science and ICT (MSIT) of the Korean government. J.R. acknowledges the Samsung Research Funding & Incubation Center for Future Technology grant (SRFC-IT1901-52) funded by Samsung Electronics, the POSCO-POSTECH-RIST Convergence Research Center program funded by POSCO, the NRF grants (RS-2024-00356928, RS-2024-00337012, RS-2024-00416272, NRF-2022M3C1A3081312) funded by the MSIT of the Korean government, and the Korea Evaluation Institute of Industrial Technology (KEIT) grant (No. 1415185027/20019169, Alchemist project) funded by the Ministry of Trade, Industry and Energy (MOTIE) of the Korean government.

**Author Contributions** S.-H.B. and S.Y. conceived the idea. S.Y. designed the depth-wavelength symmetry model. S.Y., S.-H.B., and H.H. verified the depth-wavelength symmetry model. S.Y., D.K., E.C., H.H., and M.C. performed the metalens design. S.Y. and D.S. implemented the metalens simulation. S.Y. and D.K. implemented the experimental prototype. S.L. and S.K. performed computer vision tasks. D.K. fabricated the devices. S.K. advised the computer vision experiments. A.M. advised the metalens design process. J.R. guided the material characterization and device fabrication. All authors participated in discussions and contributed to writing the manuscript. S.-H.B. and J.R. guided all aspects of the work.

**Competing Interests** The authors declare no competing financial interests.

**Supplementary Information** Supplementary Information accompanies this manuscript as part of the submission files.

**Correspondence** Correspondence should be addressed to S.-H.B. or J.R.

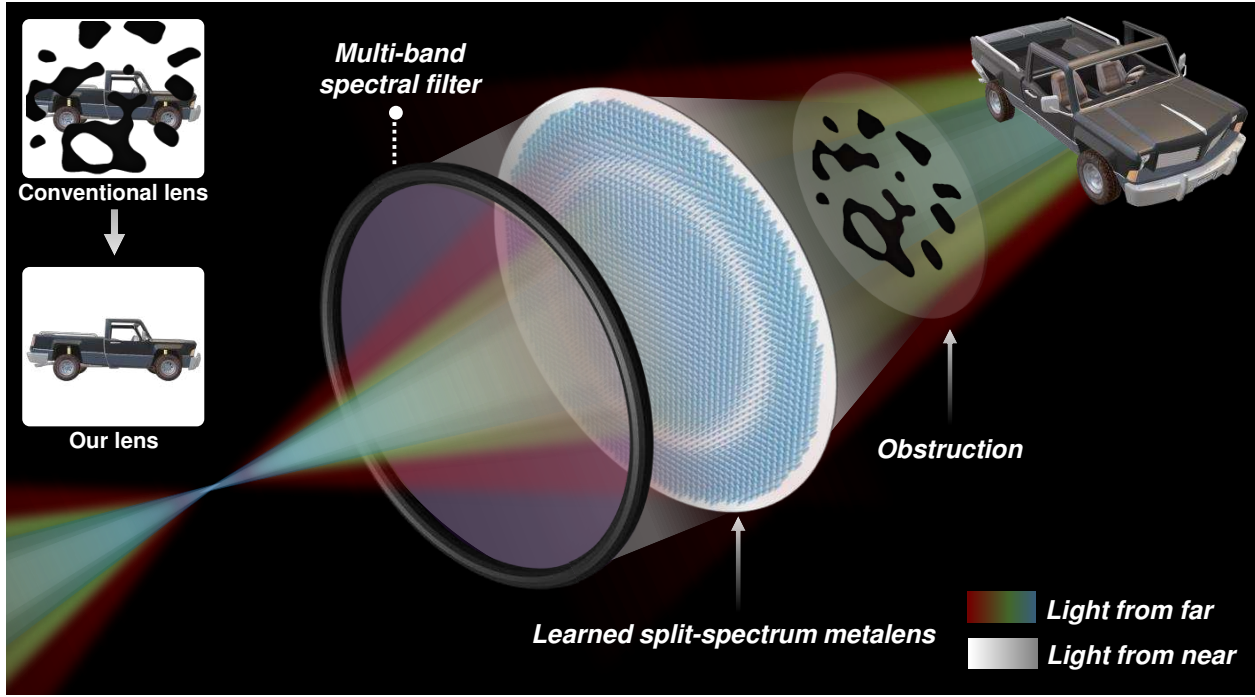


**Fig. 1: Learned split-spectrum metasurface for obstruction-free broadband imaging.** Our learned metasurface enables obstruction-free broadband imaging by filtering out the focused light from near depth with a multi-band spectral filter that selectively transmits far-focused light.

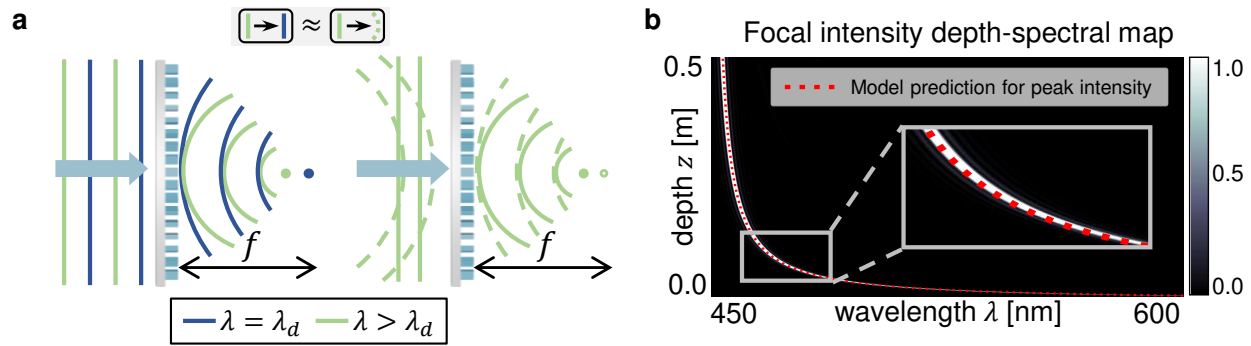


**Fig. 2: Depth-wavelength symmetry.** **a** Schematic of the depth-wavelength relationship of diffractive lenses. (Left) An incident wavelength  $\lambda$  longer than the design wavelength  $\lambda_d$  ( $\lambda > \lambda_d$ ) of the lens causes a phase mismatch, resulting in a focal front shift. (Right) This focal front shift can be compensated for by the spherical phase of an incident wave originating from a near depth, leading to an opposing focal back shift. **b** Focal point intensity map for point light sources of wavelength,  $\lambda$ , and depth,  $z$ , incident on a hyperbolic ( $\lambda_d = 450$  nm) metasurface, computed with Rayleigh-Sommerfeld diffraction, and overlaid with our depth-wavelength symmetry model.

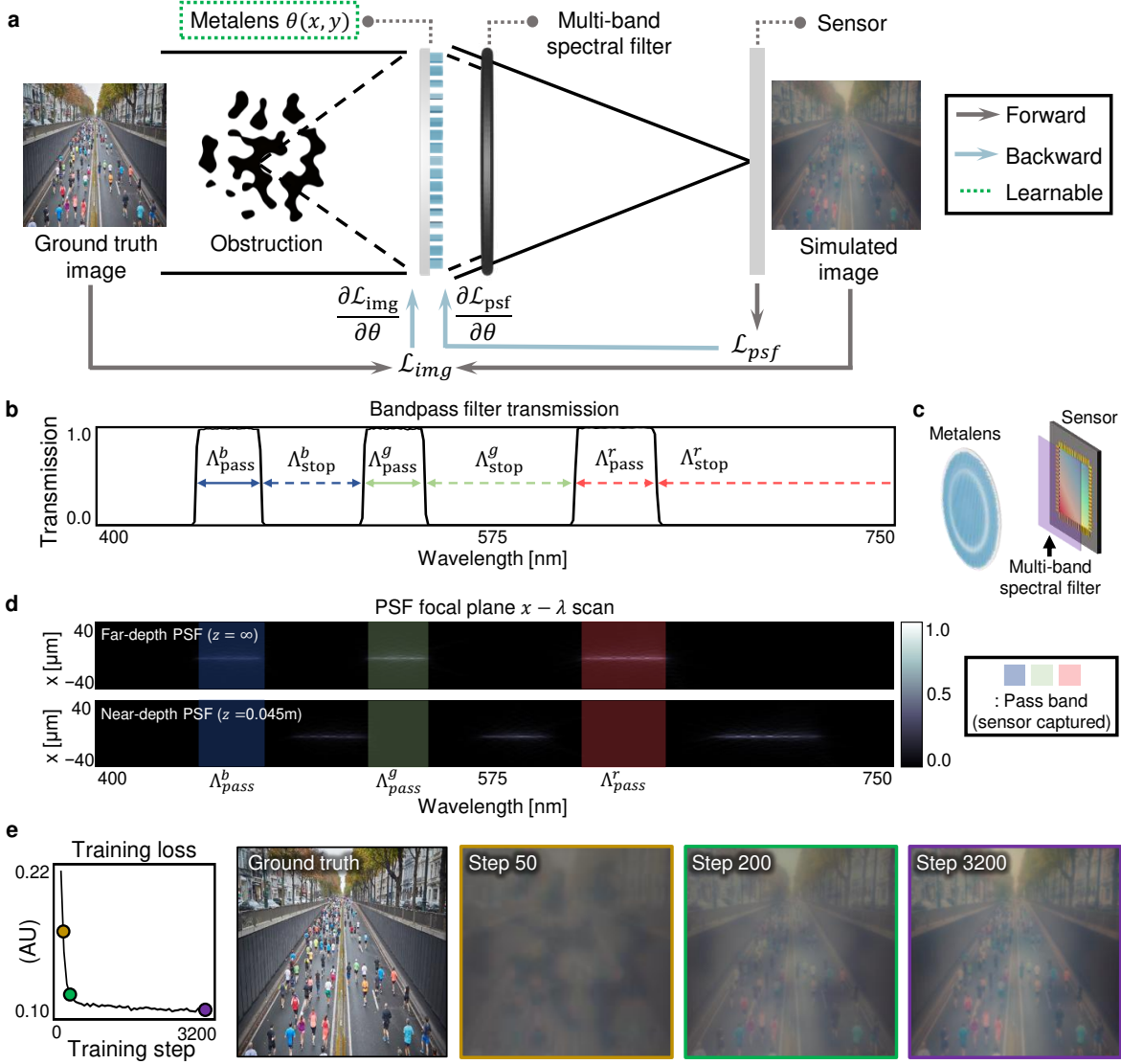


**Fig. 3: Learning split-spectrum metasurface for obstruction-free broadband imaging.** **a** Overview of the metasurface optimization pipeline. The metasurface design map  $\theta(x, y)$  is learned for the obstruction-free broadband imaging. **b** Transmission of the multi-band spectral filter, separating each color channel into the pass band  $\Lambda_{pass}^c$  and the stop band  $\Lambda_{stop}^c$ , providing extended design space for obstruction-free imaging. **c** Our imaging system consists of a metasurface, a color sensor, and a multi-band spectral filter. **d**  $x - \lambda$  scan result of the learned metasurface for far PSFs and near PSFs in simulation. **e** Training loss and visual convergence during learning. The sequence of the simulated sensor images (step 50, 200, 3200) illustrates the learning of the metasurface. Initial results exhibit significant blur and interference from obstructions, while the final optimized metasurface effectively blurs the near-depth obstructions and maintains a sharp focus on the far-depth scene.

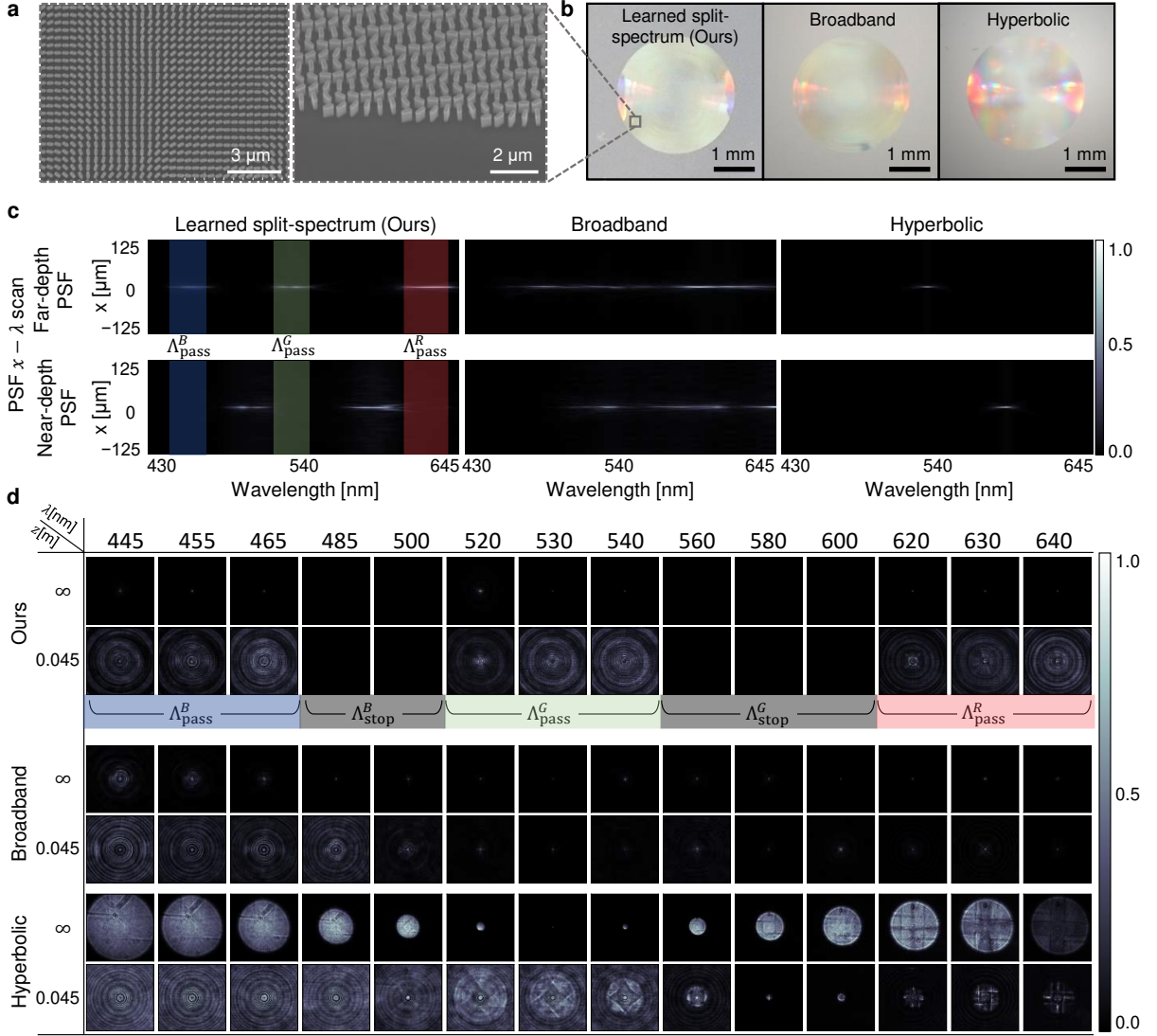


**Fig. 4: Characterization of the learned split-spectrum metalens.** **a** Scanning electron microscope (SEM) images of the learned split-spectrum metalens with the top-down view (left) and tilted view (right). **b** Photograph of the three fabricated metalenses. From left to right: the learned split-spectrum metalens (Ours), the learned broadband metalens without the split-spectrum strategy (Broadband), and the conventional hyperbolic-phase metalens (Hyperbolic). **c** PSF  $x - \lambda$  scan results normalized to the total intensity. Pass bands are highlighted. Far-depth focused lights of the obstruction-free metalens (Ours) can be transmitted and captured on the sensor, while near-depth focused lights are filtered out, enabling obstruction-free imaging. **d** 2D PSFs of metalenses for different depths, normalized to their peak intensities. The stop band PSFs of Ours are marked with black boxes. **c, d** Our far-depth PSFs remain sharp in the pass bands, enabling clear imaging of the originally occluded scene, while the near-depth PSFs are blurry. The hyperbolic metalens suffers from severe chromatic aberrations. The broadband metalens fails to achieve the near-depth blur required for obstruction-free imaging.

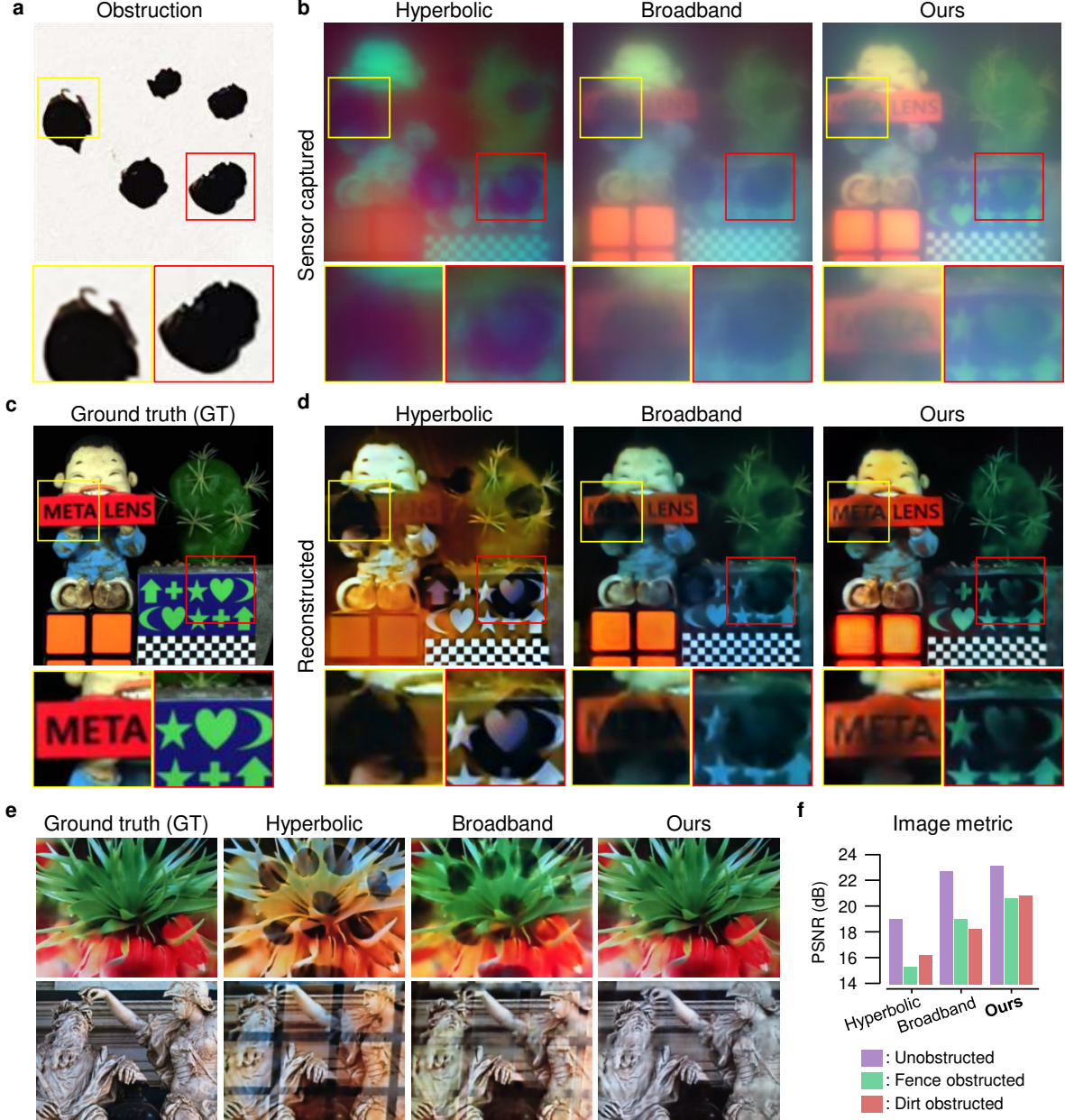


**Fig. 5: Experimental evaluation of obstruction-free broadband imaging.** **a** Near-depth obstruction pattern used for the experiment. **b** Raw sensor captured images under the obstruction for the three metalens designs. Insets provide a magnified view of the regions highlighted by yellow and red boxes. **c** Ground-truth (GT) unobstructed reference image captured with a compound lens with  $f = 8$  mm (two times longer than those of metalenses) for better object plane resolution. **d** Reconstructed images using the neural network trained for each metalelens. **e** Reconstructed image comparisons of representative printed 2D image captures under fence and dirt obstructions. **f** PSNRs measured on the printed image dataset. **b, d, e, f** Our design suppresses obstructions better than other metalens baselines, achieving superior performance across all conditions.

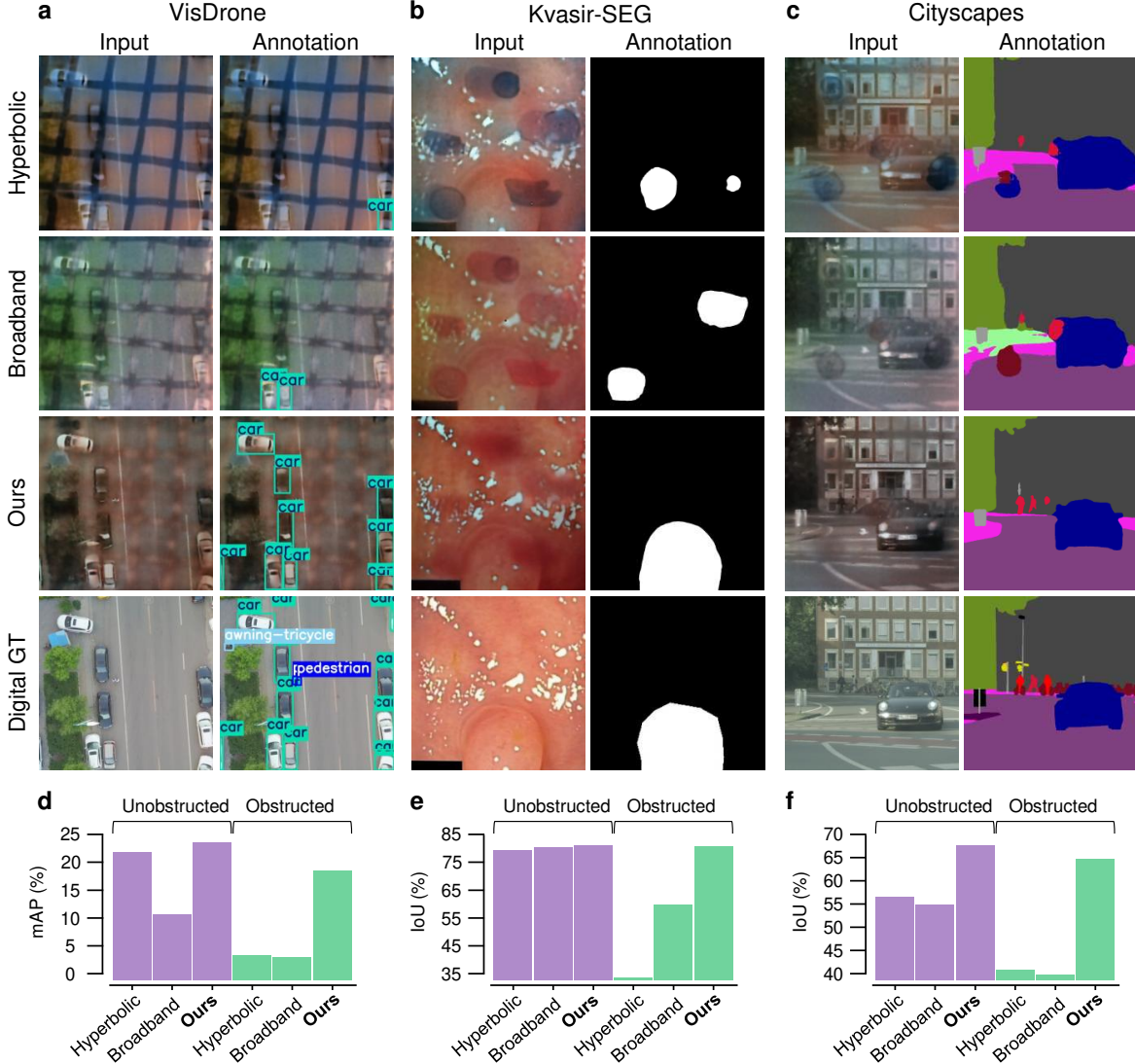


**Fig. 6: Obstruction-free visual perception.** **a–c** Input images captured with each fabricated metalens design acquired by imaging the printed Digital GT, together with the corresponding original digital images (rows: Hyperbolic, Broadband, Ours, Digital GT) under different obstructions (fence, blood drop, dirt) and the corresponding downstream task outputs (Annotation) predicted by computer vision models on three benchmarks and ground-truth label: **a** UAV-view object detection<sup>40</sup> on VisDrone<sup>41</sup>, **b** Endoscopy polyp segmentation<sup>42</sup> on Kvasir-SEG<sup>43</sup>, and **c** Driving scene semantic segmentation<sup>44</sup> on Cityscapes<sup>45</sup>. The bottom row (Digital GT) shows the original digital images and their ground-truth labels for reference. **d–f** Quantitative performance under unobstructed (purple) and obstructed (green) imaging conditions: **d** detection mAP on VisDrone, **e** intersection-over-union (IoU) on Kvasir-SEG, and **f** mean IoU (mIoU) on Cityscapes over multiple classes. Across all tasks, our learned split-spectrum metalens exhibits minimal performance degradation under obstructed conditions.

# Learned split-spectrum metalens for obstruction-free broadband imaging in the visible

Seungwoo Yoon<sup>1\*</sup>, Dohyun Kang<sup>2\*</sup>, Eunsue Choi<sup>1</sup>, Sohyun Lee<sup>3</sup>, Seoyeon Kim<sup>3</sup>, Minho Choi<sup>4,5</sup>, Hyeonsu Heo<sup>2</sup>, Dong-ha Shin<sup>3</sup>, Suha Kwak<sup>1</sup>, Arka Majumdar<sup>4,6</sup>, Junsuk Rho<sup>2,7,8,9,10†</sup>, Seung-Hwan Baek<sup>1†</sup>

<sup>1</sup>*Department of Computer Science and Engineering, Pohang University of Science and Technology (POSTECH), Pohang 37673, Republic of Korea*

<sup>2</sup>*Department of Mechanical Engineering, Pohang University of Science and Technology (POSTECH), Pohang 37673, Republic of Korea*

<sup>3</sup>*Graduate School of Artificial Intelligence, Pohang University of Science and Technology (POSTECH), Pohang 37673, Republic of Korea*

<sup>4</sup>*Department of Electrical and Computer Engineering, University of Washington, Seattle, 98195, WA, USA*

<sup>5</sup>*Department of Electrical Engineering, Ulsan National Institute of Science and Technology, Ulsan 44919, Republic of Korea.*

<sup>6</sup>*Department of Physics, University of Washington, Seattle, 98195, WA, USA*

<sup>7</sup>*Department of Chemical Engineering, Pohang University of Science and Technology (POSTECH), Pohang 37673, Republic of Korea*

<sup>8</sup>*Department of Electrical Engineering, Pohang University of Science and Technology (POSTECH), Pohang 37673, Republic of Korea*

<sup>9</sup>*POSCO-POSTECH-RIST Convergence Research Center for Flat Optics and Metaphotonics, Pohang 37673, Republic of Korea*

<sup>10</sup>*National Institute of Nanomaterials Technology (NINT), Pohang 37673, Republic of Korea*

*\*Equal contribution*

*†Corresponding author. E-mail: shwbaek@postech.ac.kr, jsrho@postech.ac.kr*

## Table of contents

**Supplementary Note 1.** Derivation and validation of the depth-wavelength symmetry model.

**Supplementary Note 2.** Broadband metalens design in the visible.

**Supplementary Note 3.** Comparison with other obstruction-free imaging methods.

**Supplementary Note 4.** Details on image simulation and metalens learning.

**Supplementary Note 5.** Details on image reconstruction neural network.

**Supplementary Note 6.** Measured complex refractive index of the  $\text{SiN}_x$  film.

**Supplementary Note 7.** Simulated conversion efficiency under variation of geometric parameters.

**Supplementary Note 8.** Broadband property across the visible wavelength of the designed meta-atom.

**Supplementary Note 9.** Fabrication process of learned split-spectrum metalens.

**Supplementary Note 10.** Details on the experimental setup.

**Supplementary Note 11.** Details on the image quality assessment.

**Supplementary Note 12.** Details on the downstream vision tasks.

**Supplementary Note 13.** Metalens point spread functions and optical MTFs.

**Supplementary Note 14.** Slanted edge MTFs.

**Supplementary Note 15.** Additional experimental imaging results.

## Supplementary Note 1: Derivation and validation of the depth-wavelength symmetry model

**Derivation.** We start with the ideal broadband focusing phase profile:

$$\phi(x, y, \omega) = -\frac{\omega}{c}(\sqrt{x^2 + y^2 + f^2} - f), \quad (\text{S1})$$

where  $x, y$  denote pupil-plane coordinate,  $\omega$  is the angular frequency,  $c$  is the speed of light, and  $f$  is the focal length.

The ideal lens profile is expanded around a certain design angular frequency  $\omega_d$  as

$$\phi(x, y, \omega) = \phi(x, y, \omega_d) + \frac{\partial \phi(x, y, \omega)}{\partial \omega} \Big|_{\omega=\omega_d} (\omega - \omega_d), \quad (\text{S2})$$

The residual first-order derivative term  $\frac{\partial \phi(x, y, \omega)}{\partial \omega} \Big|_{\omega=\omega_d} (\omega - \omega_d)$  induces chromatic aberration and our intuition is that the first-order derivative term can be matched with the conjugate phase of the spherical phase of a point source. Specifically, the spherical phase profile of a monochromatic point light source of frequency  $\omega_t$  positioned at depth  $z$  and normally incident on a metalens is defined by the following:

$$\phi_s(x, y, z, \omega_t) = \frac{\omega_t}{c} \sqrt{x^2 + y^2 + z^2}. \quad (\text{S3})$$

We simplify Equation (S3) using the paraxial approximation:

$$\phi_s(x, y, z, \omega_t) = \frac{\omega_t z}{c} \sqrt{\frac{x^2 + y^2}{z^2} + 1} \simeq \frac{\omega_t}{c} \left( z + \frac{x^2 + y^2}{2z} \right) = \frac{\omega_t}{c} \frac{x^2 + y^2}{2z}, \quad (\text{S4})$$

where the global constant phase term  $\frac{\omega_t}{c} z$  is ignored.

For the derivation of Equation (S4), the paraxial approximation used is as follows

$$\sqrt{1 + b} = 1 + \frac{b}{2} - \frac{b^2}{8} + \dots \simeq 1 + \frac{b}{2}. \quad (\text{S5})$$

The approximated spherical wave term in Equation (S4) is now equated with the first-order derivative term of the phase profile  $\frac{\partial \phi(x, y, \omega)}{\partial \omega} \Big|_{\omega=\omega_d} (\omega - \omega_d)$  as

$$\frac{\partial \phi(x, y, \omega)}{\partial \omega} \Big|_{\omega=\omega_d} (\omega_t - \omega_d) = \frac{\omega_t}{c} \frac{x^2 + y^2}{2z}, \quad (\text{S6})$$

where  $\frac{\partial\phi(x,y,\omega)}{\partial\omega}\bigg|_{\omega=\omega_d} = -\frac{1}{c}(\sqrt{x^2+y^2+f^2}-f)$ . Solving Equation (S6) with the paraxial approximation ( $\sqrt{x^2+y^2+f^2} = f\sqrt{\frac{x^2+y^2}{f^2}+1} \simeq \frac{x^2+y^2}{2f} + f$ ) yields the following relationship:

$$\begin{aligned} z &= \frac{x^2+y^2}{\frac{2c}{\omega_t}\frac{\partial\phi(x,y,\omega)}{\partial\omega}\bigg|_{\omega=\omega_d}(\omega_t-\omega_d)} \\ &= \frac{(x^2+y^2)\lambda_d}{2(\sqrt{x^2+y^2+f^2}-f)(\lambda_t-\lambda_d)} \simeq \frac{1}{2}\frac{(x^2+y^2)\lambda_d}{\left(\frac{x^2+y^2}{2f}\right)(\lambda_t-\lambda_d)} = \frac{\lambda_d f}{(\lambda_t-\lambda_d)}, \end{aligned} \quad (S7)$$

where  $\omega = \frac{2\pi c}{\lambda}$ . Finally, the relationship between  $\Delta\lambda$  and  $\Delta z$  of the depth-wavelength symmetry is derived from Equation (S7) by defining  $\Delta\lambda = \lambda_1 - \lambda_2$ , and  $\Delta z = z_1 - z_2$ :

$$\Delta\lambda = \lambda_1 - \lambda_2 = \lambda_d f \left( \frac{1}{z_1} - \frac{1}{z_2} \right) = \lambda_d f \left( \frac{1}{z_1} - \frac{1}{z_1 - \Delta z} \right). \quad (S8)$$

**Validation of the approximations.** In the derivation process, we have applied paraxial approximation to the spherical wave and hyperbolic lens phase profiles. While using paraxial approximation is a common strategy in many derivation processes in optics, we evaluate the phase and diffraction angle errors to justify the paraxial approximations in our optical configuration ( $f = 4$  mm and aperture size of 2.516 mm). We compute the diffraction angle map using the phase map gradients<sup>1,2</sup> as

$$(\theta_x, \theta_y) = \left( \arcsin \left( \frac{\lambda}{2\pi} \cdot \frac{d}{dx} \phi(x, y) \right), \arcsin \left( \frac{\lambda}{2\pi} \cdot \frac{d}{dy} \phi(x, y) \right) \right). \quad (S9)$$

Figure S1a,b,c visualizes the phase map of the spherical light source  $\phi_s(x, y, z, \omega_t)$  emitted from a depth of  $z = 0.045$  m, its approximation  $\frac{\omega_t}{c} \frac{x^2+y^2}{2z}$ , and the difference between the two, along with the diffraction angle map calculated from the phase map and their differences. The maximum value of the diffraction angle map error ratio  $\frac{|O-A|}{|O|}$ , (O: original, A: approximated) is of 0.03911 %. The negligible magnitude of the error validates the use of the approximation for the spherical wavefront.

Next, we examine the approximation of the metalens phase profile. Note that the approximation ( $\sqrt{x^2+y^2+f^2} = f\sqrt{\frac{x^2+y^2}{f^2}+1} \simeq \frac{x^2+y^2}{2f} + f$ ) is approximating the hyperbolic phase map ( $-\frac{\omega}{c}(\sqrt{x^2+y^2+f^2}-f)$ ) to the quadratic phase map ( $-\frac{\omega}{c} \frac{x^2+y^2}{2f}$ ) using the paraxial approximation<sup>2</sup>. Figure S2a,b,c compare the exact hyperbolic profile at  $\lambda = 532$  nm with its quadratic approximation. In this case, the maximum value of the diffraction angle map error ratio increases to 4.997 %, indicating the presence of spherical aberration in the quadratic phase map. However, the goal of our model is to predict the focal point shift, rather than the exact PSF structure. Since both the hyperbolic and quadratic phase profiles are defined by the same focal length  $f$ , the axial positions of

their focal points remain almost consistent despite the aberration introduced by the approximation. Consequently, the approximation does not compromise the validity of our depth-wavelength symmetry model. We further validate this claim in Figure S3, which demonstrates that the predicted focal shifts of hyperbolic phase metalenses align well with numerical simulations across various numerical apertures (NA).

**Depth-wavelength symmetry model for propagation-phase metalenses.** While our main implementation uses geometric-phase meta-atoms, propagation-phase (dynamic-phase) meta-atoms are another widely used route to realize metasurfaces. The phase delay of a propagation-phase meta-atom can be written as

$$\phi(x, y, \omega) = \frac{\omega}{c} n_{\text{eff}}(x, y, \omega) h \pmod{2\pi},$$

where  $n_{\text{eff}}(x, y, \omega)$  denotes the effective refractive index of the meta-atom at  $(x, y)$  and  $h$  is the meta-atom height. The hyperbolic phase metalens can be implemented by the propagation phase meta-atoms, and for the design angular frequency  $\omega_d$ , the following holds:

$$\phi(x, y, \omega_d) = \frac{\omega_d}{c} n_{\text{eff}}(x, y, \omega_d) h = -\frac{\omega_d}{c} (\sqrt{x^2 + y^2 + f^2} - f) \pmod{2\pi}.$$

The corresponding first-order derivative (group-delay term) at the design frequency  $\omega_d$  is defined by the following:

$$\frac{\partial \phi(x, y, \omega)}{\partial \omega} \bigg|_{\omega=\omega_d} = \frac{1}{c} n_{\text{eff}}(x, y, \omega_d) h + \frac{\omega_d}{c} \frac{\partial n_{\text{eff}}(x, y, \omega)}{\partial \omega} \bigg|_{\omega=\omega_d} h.$$

The first term corresponds to the  $\omega$ -dependent optical path length (OPL) contribution to the group delay, whereas the second term captures the additional contribution from the dispersion of  $n_{\text{eff}}$ .

Similar to the geometric-phase case, standard propagation-phase metalenses without dispersion engineering do not provide the required group-delay profile for broadband achromatic focusing<sup>3</sup>, leading to chromatic focal shifts. Practically, the OPL-related term provides the dominant spatial trend of the group-delay profile, and the  $n_{\text{eff}}$ -dispersion term acts as a minor correction<sup>4</sup>. Motivated by this observation, one can match the residual first-order term with the spherical-wave phase contribution of a finite-depth point source to obtain an approximation of the depth-wavelength symmetry mapping in Equation (S7), given a meta-atom library (or a surrogate model) for  $n_{\text{eff}}$  and  $h$ .

We empirically validate this behavior using a publicly available proxy model for propagation-phase meta-atoms<sup>5</sup> in Figure S4 using the same configuration as in the main text ( $D = 2.516$  mm,  $f = 4$  mm), where the model prediction closely agrees with the numerically computed focal shift maps. These results provide a useful leading-order description of chromatic focal shifts in propagation-phase metalenses, supporting the applicability of our model beyond geometric-phase implementations, while the accuracy may depend on the strength of  $n_{\text{eff}}$  dispersion and the operating bandwidth.

**Expansion of the depth-wavelength symmetry model to the broadband case.** The relationship given in Equation (S7) implies that a phase map designed to focus a plane light source of  $\lambda_d$  also focuses a spherical light source of  $\lambda_t$  from depth  $z = \frac{\lambda_d f}{\lambda_t - \lambda_d}$  at same focal plane distant at  $f$ . We extend this principle to a broadband diffractive lens, which is designed to focus plane waves across a continuous spectrum  $[\lambda_{\min}, \lambda_{\max}]$ . This is achieved by spatially multiplexing the phase profiles  $\phi(x, y, \omega_d)$  corresponding to  $\lambda_d \in [\lambda_{\min}, \lambda_{\max}]$ . Consequently, such a lens is expected to focus light from a finite depth  $z$  over a shifted broadband spectrum  $[\frac{\lambda_{\min}f}{z} + \lambda_{\min}, \frac{\lambda_{\max}f}{z} + \lambda_{\max}]$  following the depth-wavelength symmetry. To demonstrate this behavior, we define a broadband phase profile by spatially interleaving hyperbolic phase maps:

$$\begin{aligned} \phi(x, y)_{\text{broadband}} &= \sum_{i=0}^{N-1} \phi_i(x, y) \cdot \mathbb{I}_i(r), \\ \text{where } \phi_i(x, y) &= \frac{2\pi}{\lambda_i} \left( \sqrt{x^2 + y^2 + f^2} - f \right), \\ \lambda_i &= 450 \text{ nm} + i \cdot \Delta\lambda, \quad (N = 201, \Delta\lambda = 1 \text{ nm}), \\ \mathbb{I}_i(r) &= \begin{cases} 1, & \lfloor r/\Delta r \rfloor \equiv i \pmod{N} \\ 0, & \text{otherwise.} \end{cases} \end{aligned} \quad (\text{S10})$$

The phase profiles are configured with a focal length  $f = 4$  mm and lens diameter  $D = 2.516$  mm. The design spectrum  $\lambda \in [450 \text{ nm}, 650 \text{ nm}]$  is sampled at 1 nm intervals, resulting in  $N = 201$  interleaved hyperbolic profiles. Figure S5a visualizes the simulated focal point intensity map of this broadband lens. The overlaid analytical curves derived from our depth-wavelength symmetry model accurately predict the high-intensity focal trajectories of the broadband lens. This agreement confirms that our depth-wavelength symmetry model is applicable to diffractive lenses with arbitrary design spectra, effectively predicting the focal shift behavior essential for our split-spectrum strategy and the extended depth-of-field behaviors observed in other studies<sup>6-11</sup>.

The focal intensity maps of the phase profiles in the main text and Figure S5a are computed using a circularly symmetric Rayleigh-Sommerfeld integral<sup>8</sup>:

$$E(r, z) = 2\pi \int_0^R E(r', 0) \frac{e^{ikr}}{r} \frac{z}{r} \left(1 + \frac{i}{kr}\right) r' dr', \quad (\text{S11})$$

where  $r = \sqrt{(x - x')^2 + (y - y')^2 + z^2}$ .

The core mechanism of our obstruction-free imaging is to ensure that the sharp PSFs, optimized for far-depth targets within the pass bands, are spectrally shifted into the stop bands when the source is located at near depth. This configuration guarantees that the sharp focal components are rejected by the filter; consequently, the remaining optical response for near-depth obstructions within the pass bands becomes dominated by the defocused profiles, effectively rendering the obstructions blurry.

**Selection of pass bands and stop bands.** The mechanism of our obstruction-free imaging is to ensure that the sharp PSFs, designed for far-depth targets within the pass bands, are spectrally shifted into the sensor’s stop bands when the source is located at near depth; consequently, these sharp components are rejected, and provide the flexibility to enforce strong blur for near-depth obstructions within the pass bands. We use a commercially available multi-band spectral filter (Edmund Optics, 457, 530 & 628 nm, 50 mm Dia., Tri-Band Filter) whose transmission bandwidths are 22 nm, 20 nm, and 28 nm at center wavelengths 457 nm (B), 530 nm (G), and 628 nm (R). This determines the placement of pass bands,  $\Lambda_{\text{pass}}^c$  and stop band,  $\Lambda_{\text{stop}}^c$ , which is illustrated in Figure S5b. Based on the depth-wavelength symmetry, the condition for obstruction removal requires that the focused near-depth PSFs are spectrally shifted to fall within the stop bands for every color channel. This can be formalized using Equation (S7) as a set of inequalities:

$$\begin{aligned} f \cdot \frac{\min \Lambda_{\text{pass}}^b}{z_{\text{near}}} + \min \Lambda_{\text{pass}}^b &> \min \Lambda_{\text{stop}}^b, \\ f \cdot \frac{\max \Lambda_{\text{pass}}^b}{z_{\text{near}}} + \max \Lambda_{\text{pass}}^b &< \min \Lambda_{\text{pass}}^g, \\ f \cdot \frac{\min \Lambda_{\text{pass}}^g}{z_{\text{near}}} + \min \Lambda_{\text{pass}}^g &> \min \Lambda_{\text{stop}}^g, \\ f \cdot \frac{\max \Lambda_{\text{pass}}^g}{z_{\text{near}}} + \max \Lambda_{\text{pass}}^g &< \min \Lambda_{\text{pass}}^r, \\ f \cdot \frac{\min \Lambda_{\text{pass}}^r}{z_{\text{near}}} + \min \Lambda_{\text{pass}}^r &> \min \Lambda_{\text{stop}}^r. \end{aligned}$$

As depicted in Figure S5b, our chosen configuration with ( $z_{\text{near}} = 0.045$  m,  $f = 4$  mm) satisfies these conditions. The dashed horizontal line at  $z = 0.045$  m intersects the spectral curves in regions that align with the gray stop bands, or outside the sensor sensitivity. This ensures that the sharp focal components corresponding to the far-depth focus are spectrally shifted into the stop bands and rejected, thereby granting us the design freedom to explicitly optimize the remaining pass-band response for strong defocus at near depth.

Note that since Equation (S7) contains an asymptote, fixing  $z_{\text{near}}$  does not uniquely determine  $z_{\text{far}}$ ; we set the threshold of the  $z_{\text{far}}$  as 0.5 m, and depth value  $z$  greater than 0.5 m will satisfy the relationship, and the working range for sharp imaging is not limited. The configuration  $z_{\text{near}}$  and  $f$  can be flexibly determined using Equation (S7). Custom-designing the multi-band spectral filter would offer additional degrees of freedom to select the placement and bandwidth of each band. Specifically, we can split the spectra of each color channel into more than two bands and interleave the pass bands.

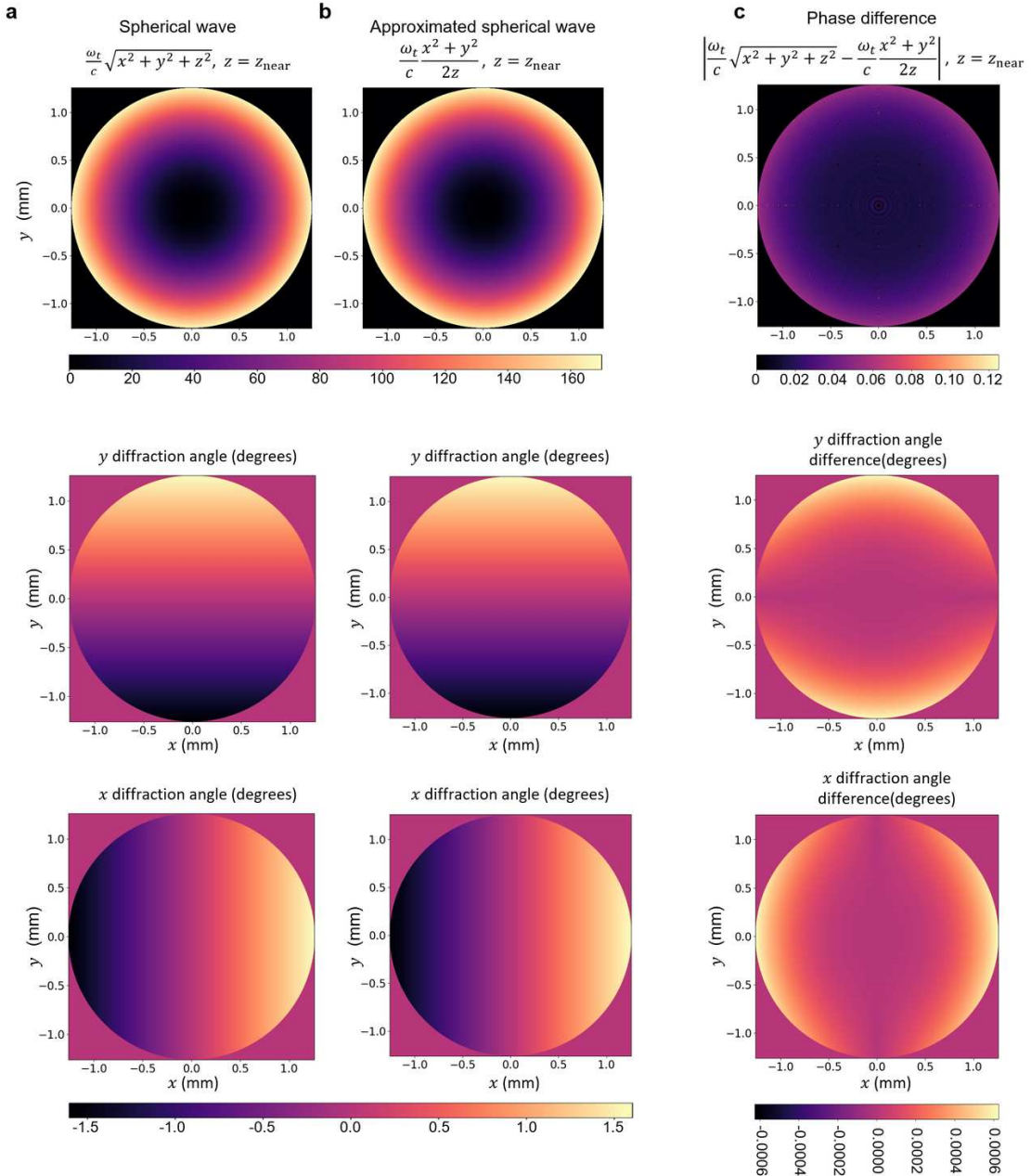


**Figure S1: Validation of the paraxial approximation for the spherical light source.**  
 First row: Phase maps, second row:  $y$ -axis diffraction angle maps from the phase maps, third row:  $x$ -axis diffraction angle maps. **a** The exact phase map and diffraction angle map of a spherical wave emitted from  $z_{\text{near}} = 0.045$  m, and **b** its paraxial approximation. **c** The absolute difference between the exact and the approximated maps.

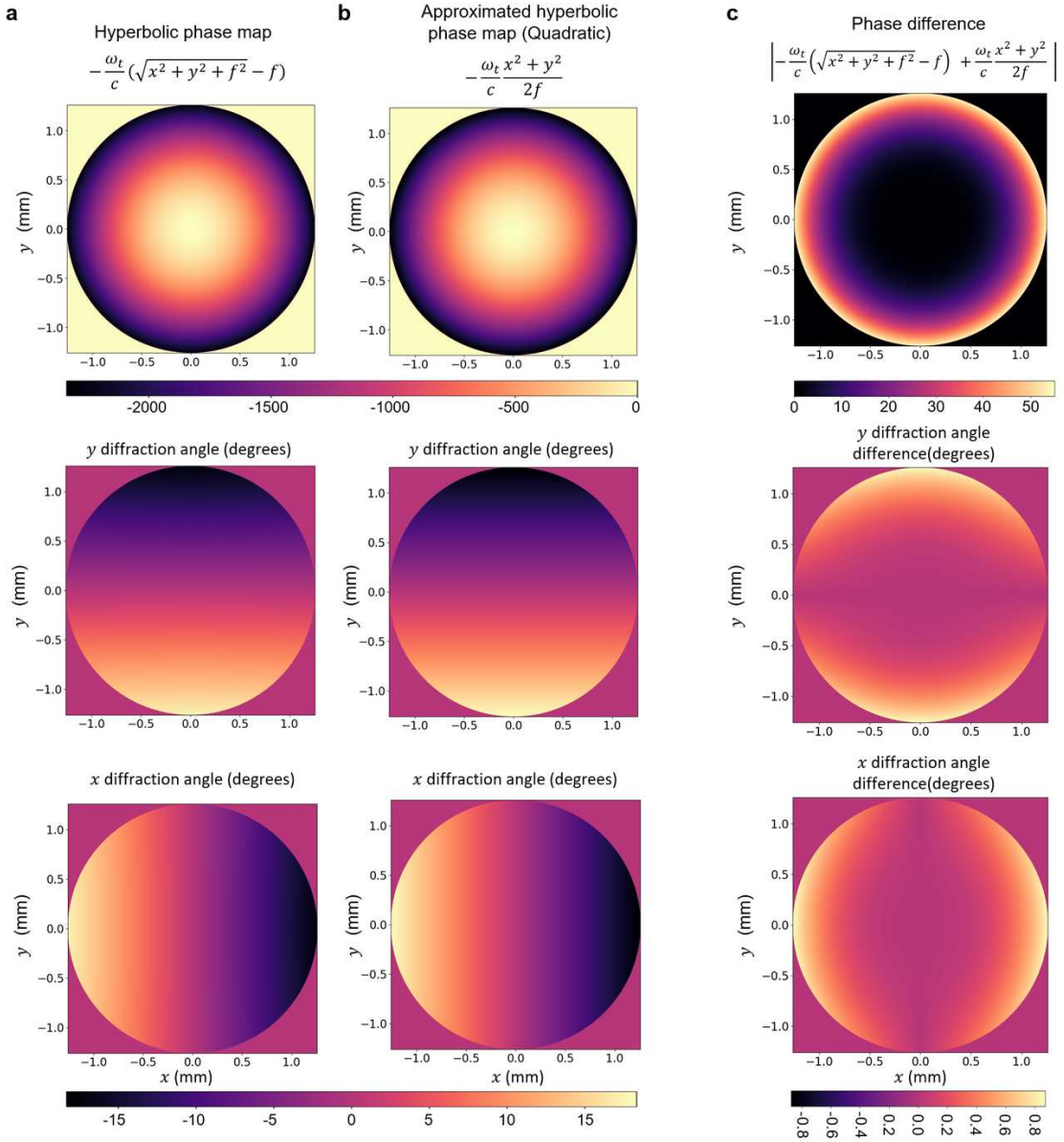


**Figure S2: Validation of the paraxial approximation for the hyperbolic phase.** First row: Phase maps, second row:  $y$ -axis diffraction angle maps from the phase maps, third row:  $x$ -axis diffraction angle maps. **a** The exact phase map and diffraction angle map of a hyperbolic phase profile designed for a focal length  $f = 4$  mm, at  $\lambda = 532$  nm and **b** its paraxial approximation. **c** The absolute difference between the exact and the approximated maps.

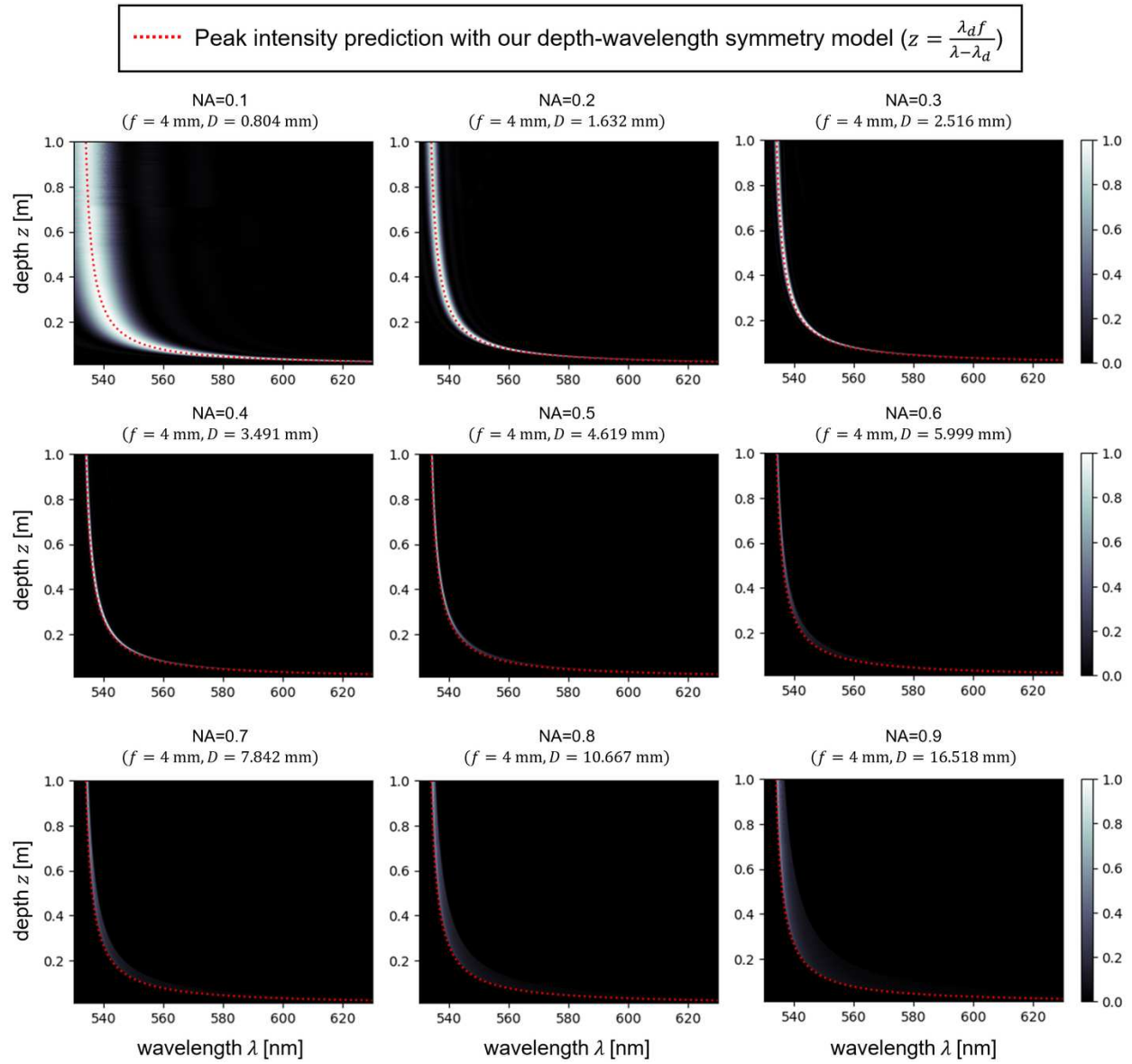


**Figure S3: Robustness of depth-wavelength symmetry model across various Numerical Apertures (NA).** The focal point intensity depth-spectral maps of hyperbolic phase metasurfaces are simulated for different NA configurations by varying the lens aperture size while fixing the focal length. The dashed lines indicate the theoretical focal shifts predicted by our depth-wavelength symmetry model. The close agreement between the simulated high-intensity regions and the theoretical curves confirms that the proposed model accurately predicts the focal shift regardless of the approximation errors in the high-NA regime.

Focal intensity depth-spectral map for propagation phase hyperbolic metalenses

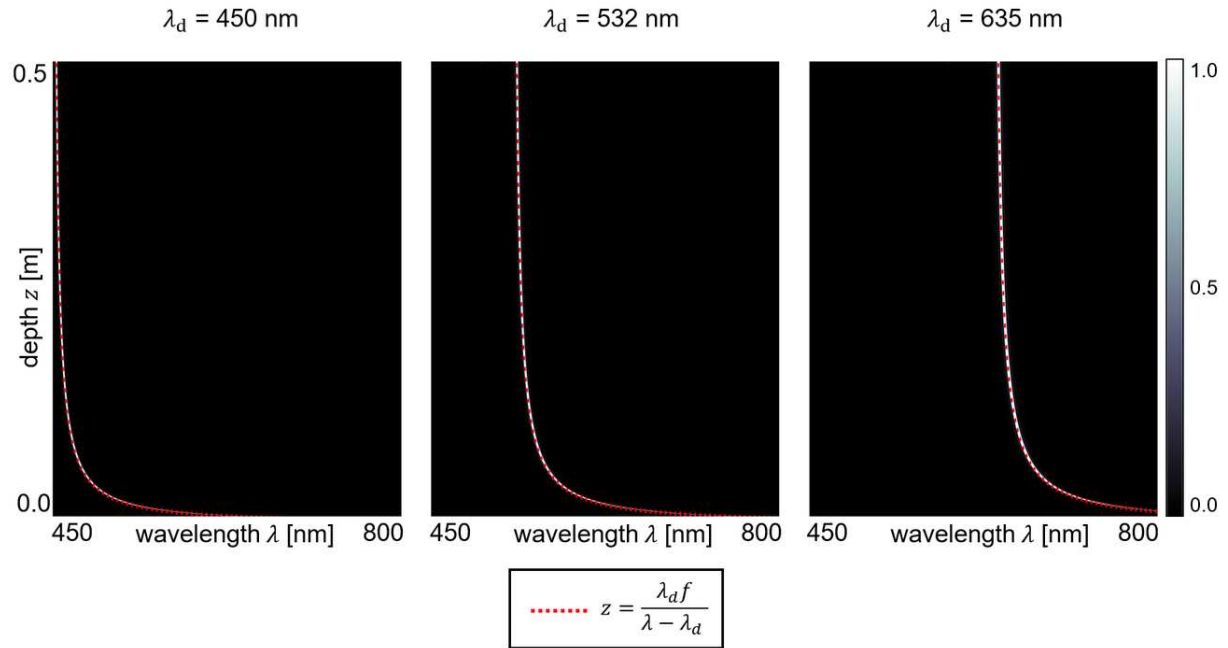


**Figure S4: Depth-wavelength symmetry in propagation-phase hyperbolic metalenses.**

Focal intensity depth-spectral maps of propagation-phase hyperbolic metalenses designed at three different design wavelengths,  $\lambda_d = 450$  nm (left),  $532$  nm (middle), and  $635$  nm (right), computed under the same configuration as in the main text (focal length,  $f = 4$  mm and aperture diameter,  $D = 2.516$  mm). The predicted depth-wavelength symmetry curve (red dotted) from the equation, (S7) closely matches the high-intensity regions.

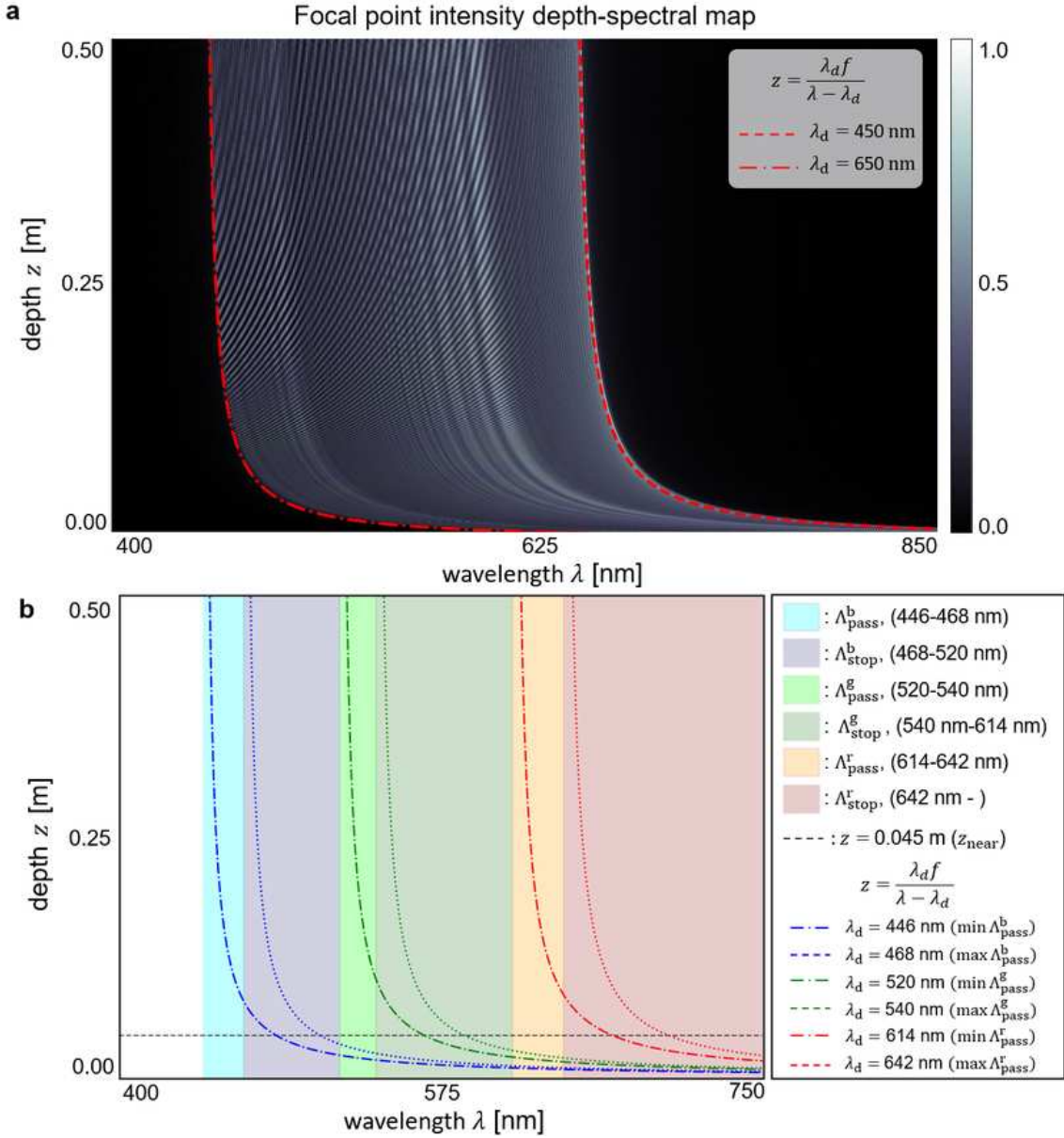


**Figure S5: Validation of the depth-wavelength symmetry model and band selection for obstruction-free imaging** **a** The simulated focal point intensity map of the broadband metalens plotted against wavelength and depth. The overlaid dashed red curves represent the theoretical focal shifts predicted by our depth-wavelength symmetry model for lower and upper spectral limits of the design spectrum, which align with the leftmost and rightmost curves of the simulated high-intensity regions. **b** The spectral configuration of pass bands and stop bands determined by the multi-band spectral filter. The dashed curves indicate the wavelength shift of the focused light for design wavelengths ( $\lambda_d$ ) of lower limits and upper limits of the pass bands. The horizontal line at  $z_{\text{near}} = 0.045 \text{ m}$  illustrates that the sharp near-depth focal points shifted from the far-depth sharp far-depth pass bands are located within the stop bands, or outside the sensor's sensitivity range, enforcing strong blur for the near-depth obstruction while enabling the maintenance of sharp focus for far-depth targets.

## Supplementary Note 2: Broadband metalens design in the visible

Table S1 provides a comparative benchmark of recent visible broadband diffractive lens studies based on their NA, aperture size, achromaticity, and reliance on computational backend. Our approach, aligned with other high-performance computational imaging systems, exhibits depth-wavelength symmetry and leverages a computational backend to achieve a significantly larger aperture of  $2500\ \mu\text{m}$  and a high NA of 0.3. The derivation provided in the Supplementary Note 1 assumes that the diffractive lens is chromatic, or the diffractive lens cannot satisfy the focusing phase profiles for wavelengths other than  $\lambda_d$ . The depth-wavelength symmetry model we propose is not applied to achromatic diffractive lenses. The achromatic diffractive lenses are typically achieved by dispersion-engineering that controls phase delays along with the group delay and group delay dispersion. However, the dispersion engineering strategy to achieve achromatic diffractive lenses is fundamentally constrained by low numerical aperture and small diameters<sup>12,13</sup>, limiting their application to real-world imaging systems. Therefore, numerous studies that aim for real-world metaoptics or diffractive optics imaging used chromatic diffractive lenses to achieve large-aperture and high NA, or fast lens, and were aided by a computational backend to correct aberrations. Therefore, diffractive lenses of the practical scale will exhibit the depth-wavelength symmetry we propose.

Reference	NA	Aperture ( $D, \mu\text{m}$ )	Dispersion engineering ( $\Delta\lambda, \text{nm}$ )	Computational backend	Depth-wavelength symmetry
Chen et al. <sup>14</sup>	0.02	220	Yes (470–670)	No	No
Chen et al. <sup>15</sup>	0.2	26.4	Yes (460–700)	No	No
Hu et al. <sup>16</sup>	0.164	50	Yes (400–1000)	No	No
Chang et al. <sup>3</sup>	0.02	400	Yes (400–700)	No	No
Colburn et al. <sup>6</sup>	0.46	200	No	Yes	Yes
Huang et al. <sup>7</sup>	0.45	200	No	Yes	Yes
Bayati et al. <sup>11</sup>	0.46	1000	No	Yes	Yes
Fröch et al. <sup>8</sup>	0.24	10000	No	Yes	Yes
<b>This work</b>	<b>0.30</b>	<b>2500</b>	<b>No</b>	<b>Yes</b>	<b>Yes</b>

**Table S1: Comparison of visible broadband diffractive optics imaging systems.** The table benchmarks their optical specifications, including numerical aperture (NA), aperture size, achromaticity, computational backend reliance, and depth-wavelength symmetry.

### Supplementary Note 3: Comparison with other obstruction-free imaging methods

Table S2 compares representative obstruction-free imaging paradigms using four practical criteria: module compactness, hallucination risk (whether the pipeline must synthesize occluded content rather than directly measure it), and whether the method is single-shot and single-view.

Single-image inpainting methods are attractive for compact deployment because they operate on a single captured image (single-shot, single-view). However, they inherently solve an ill-posed completion problem and may synthesize unseen structures, which introduces fidelity risks and typically incurs high computational cost. Multi-view (or burst) occlusion layer separation reduces hallucination risk by leveraging parallax or motion cues, but it generally requires multiple viewpoints and/or multiple frames, leading to capture overhead and sensitivity to layer/flow estimation errors. Crucially, such approaches are fundamentally inapplicable to obstructions fixed relative to the camera system—such as the cover-glass contaminants targeted in this work—as the absence of relative motion precludes the generation of necessary parallax cues.

Optical approaches based on synthetic apertures can physically suppress near-depth occluders via depth-of-field control and refocusing with low hallucination risk, but they usually require large baselines or camera arrays, resulting in bulky and costly setups that are difficult to integrate into compact platforms. Hybrid diffractive–compound refractive systems can remain single-shot and single-view, yet often rely on bulky compound optics to compensate for limited optical suppression, which negates the advantage of the compactness of the diffractive optics.

In contrast, our learned split-spectrum metalens is designed to achieve a favorable operating point: a single-layer metalens with a monolithic form factor that is both single-shot and single-view with low hallucination risk.

Approach	Compact <sup>a</sup>	Halluc. <sup>b</sup>	Single-shot <sup>c</sup>	Single-view <sup>c</sup>	Short notes
Inpainting / generative removal <sup>17–19</sup>	Yes	High	Yes	Yes	Synthesize unseen content (fidelity risk), high computational cost.
Multi-view (or burst) occlusion layer separation <sup>20–25</sup>	Yes	Moderate	No	No	Relies on parallax/flow; capture overhead, layer/flow estimation errors, typically high computational cost, inapplicable to obstructions fixed relative to the camera system.
Synthetic aperture / camera array <sup>26–29</sup>	No	Low	Yes	No	Physically suppresses near obstructions via DoF/refocusing, but bulky/costly setups.
Compound–diffractive optics <sup>30</sup>	Moderate	Low	Yes	Yes	Single-view capture, but needs compound optics.
<b>This work: learned split-spectrum metalens</b>	<b>Yes</b>	<b>Low</b>	<b>Yes</b>	<b>Yes</b>	Single-layer metalens-enabled monolithic form-factor. Pass/stop-band splitting paradigm enables far focus while rejecting focused near-depth light in a single-layer chromatic metalens.

<sup>a</sup> **Compact:** easy integration into space-constrained camera modules without large baselines/arrays or bulky compound optics.

<sup>b</sup> **Hallucination risk:** whether the pipeline must synthesize occluded content rather than directly measure it.

<sup>c</sup> **Single-shot / single-view:** one temporal capture / one viewpoint-sensor (no stereo/array/motion parallax dependence).

**Table S2:** Comparison of obstruction-free imaging approaches using compactness, hallucination risk, and capture/viewpoint requirements.

## Supplementary Note 4: Details on image simulation and metalens learning

This section describes the details of the image simulation, loss functions, and metalens learning.

**Meta-atom phase.** We choose a geometric phase<sup>31</sup> for our metalens design. The geometric phase achieves phase delay solely through the rotation angle of the meta-atoms, regardless of the wavelength of the incident light, making them inherently broadband-working and providing efficient computational modeling. The metalens phase delay,  $\phi_{\text{meta}}(x, y)$  is directly mapped from the rotation angle of the meta-atom,  $\theta_{\text{meta}}(x, y)$  as:

$$\phi_{\text{meta}}(x, y) = 2\theta_{\text{meta}}(x, y). \quad (\text{S12})$$

**PSF simulation.** The PSF is computed for a given metalens design map  $\theta_{\text{meta}}(x, y)$ , depth of the spherical light source  $z$ , and color channel  $c \in \{R, G, B\}$  as:

$$P_z^c = f_{\text{psf}}(\theta_{\text{meta}}, z, c).$$

The band-limited Angular Spectrum Method<sup>1</sup> is used to propagate spherical light source  $\phi_S$  modulated by the metalens phase to the sensor plane as:

$$f_{\text{psf}}(\theta_{\text{meta}}, z, c) = |f_{\text{ASM}}(\phi_S(x, y, z, \lambda) + \phi_{\text{meta}}(x, y))|^2.$$

The wavelength  $\lambda$  is sampled from the spectral sensitivity function  $S^c(\lambda)$ :

$$S^c(\lambda) = \text{CRF}^c(\lambda) \cdot T_{\text{BPF}}(\lambda) \cdot \eta_{\text{meta}}(\lambda),$$

where  $\text{CRF}^c(\lambda)$  is the camera response function of the color channel  $c$ ,  $T_{\text{BPF}}(\lambda)$  is the spectral filter transmission, and  $\eta_{\text{meta}}(\lambda)$  is the meta-atom conversion efficiency computed from rigorous coupled-wave analysis simulation. Each component of the spectral sensitivity function is presented in Figure S6. PSFs calculated for each color channel are concatenated to form a three-channel PSF,  $P_z$ .

**Image simulation.** The sensor-captured image  $I_{\text{captured}}$  is simulated by an obstruction-aware alpha-blending model<sup>30</sup> with the simulated PSF as:

$$I_{\text{captured}} = \alpha \odot (P_{z_{\text{near}}} * I_{\text{obs}}) + (1 - \alpha) \odot (P_{z_{\text{far}}} * I_{\text{clean}}),$$

$$\alpha = \mathbf{1}\{I_{\text{obs}}(x, y) \neq 0\} * P_{z_{\text{near}}},$$

where  $*$  is the convolution operator,  $\odot$  is the pixel-wise Hadamard product operator, and  $\mathbf{1}\{\cdot\}$  is the indicator function. High-resolution three-channel image  $I_{\text{clean}}$  is sampled from training set of DIV2K<sup>32</sup> images, and  $I_{\text{obs}}$  is randomly generated following the Perlin Noise-based dirt model<sup>30,33</sup>.  $z_{\text{near}}$  is sampled from [0.04 m, 0.05 m] and  $z_{\text{far}}$  is sampled from [1 m, 20 m]. The convolution operation and the Hadamard product are done in a channel-wise manner.

**Image similarity loss.** The image similarity loss  $\mathcal{L}_{\text{img}}$  encourages the simulated sensor-captured image  $I_{\text{captured}}$  to be similar to the clean ground-truth image  $I_{\text{clean}}$ :

$$\mathcal{L}_{\text{img}}(I_{\text{captured}}, I_{\text{clean}}) = \mathcal{L}_{\text{L1}}(I_{\text{captured}}, I_{\text{clean}}) + \mathcal{L}_{\text{SSIM}}(I_{\text{captured}}, I_{\text{clean}}) + \mathcal{L}_{\text{DA}}(I_{\text{captured}}, I_{\text{clean}}),$$

where  $\mathcal{L}_{\text{L1}}$  is the pixel-wise L1 loss between the two images,  $\mathcal{L}_{\text{SSIM}}$  is the structural similarity index measure loss defined by  $1 - \text{SSIM}(I_1, I_2)$ , and  $\mathcal{L}_{\text{DA}}$  is the Domain Adaptation loss<sup>34</sup>, which is a L1 loss computed between image features extracted by DeepLabv3+<sup>35</sup>.

**PSF loss.** In addition to the image similarity losses, the PSF-based loss  $\mathcal{L}_{\text{psf}}$  is used as a regularizer to help the metalens learning:

$$\begin{aligned} \mathcal{L}_{\text{psf}} &= \mathcal{L}_{\text{bright}} + \mathcal{L}_{\text{sharp}}, \\ \mathcal{L}_{\text{bright}} &= \frac{3N}{\sum_x \sum_y P_{z_{\text{far}}}(x, y)} - 1, \\ \mathcal{L}_{\text{sharp}} &= \frac{N}{\sum_{i=-2}^2 \sum_{j=-2}^2 P_{z_{\text{far}}}(x_c + i, y_c + j)} - 1, \end{aligned}$$

where  $\mathcal{L}_{\text{bright}}$  encourages input energy is conserved at the sensor plane for  $P_{z_{\text{far}}}$ , and  $\mathcal{L}_{\text{sharp}}$  prefers sharp  $P_{z_{\text{far}}}$ .  $N$  is the number of pixels computed by  $\sum_{x,y} 1$ . Note that  $\sum_x \sum_y P_{z_{\text{far}}}(x, y) = 3N$  when light energy is conserved at the sensor plane, or the incident light energy does not leak out of the sensor, since PSF is three-channel.  $(x_c, y_c)$  is the center position of the PSF. We use a sensor of pitch  $1.85 \mu\text{m}$  and resolution  $512 \times 512$ . We empirically found that the configurations used in  $\mathcal{L}_{\text{sharp}}$  balances between the sharp far-PSFs and blurry near-PSFs; otherwise, far-PSFs and near-PSFs are both likely to be sharp.

**Metalens learning.** The final objective function to learn the metalens is defined as follows:

$$\underset{\theta}{\text{minimize}} \mathcal{L}_{\text{img}}(I_{\text{captured}}, I_{\text{clean}}) + \mathcal{L}_{\text{psf}}(P_{z_{\text{near}}}, P_{z_{\text{far}}}). \quad (\text{S13})$$

We optimize this objective function with the first-order AdamW optimizer<sup>36</sup>. We select a learning rate of 0.1 and use the cosine annealing<sup>37</sup> for the learning rate scheduler, where  $T_{\text{max}}$  is selected as 5000 steps. The training takes 26 hours on an NVIDIA A6000 GPU.

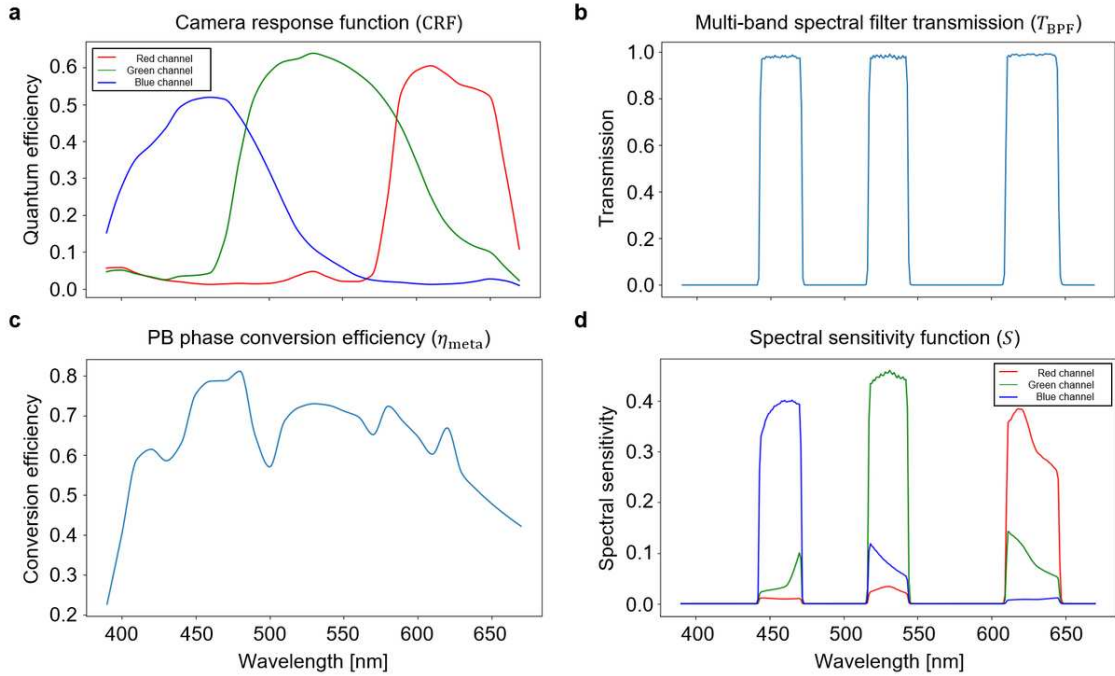


**Figure S6: Spectral characterization of the imaging system.** **a** Camera response functions for the RGB color channels provided by the camera vendor. **b** Multi-band spectral filter transmission graph provided by the vendor. **c** Metasurface conversion efficiency computed with rigorous coupled wave analysis simulation. **d** The resulting spectral sensitivity of the imaging system obtained as the product of **a**, **b**, and **c**.

## Supplementary Note 5: Details on image reconstruction neural network

While dispersion engineering for broadband achromatic diffractive lenses is fundamentally limited by low NA and small diameter, the chromatic lens-based broadband diffractive imaging suffers from aberrations. Therefore, numerous studies co-design the optics with a computational backend or support the optics with neural networks to improve image quality. We use the light-weight neural network<sup>38</sup> that can be integrated into edge devices for compact obstruction-free imaging. We train a separate neural network for each metalens. This section describes the image reconstruction neural network specifications.

**Neural network architecture.** Figure S7 shows the detailed architecture of the image reconstruction network. The neural network is based on U-Net<sup>39</sup> architecture, and incorporates CBAM modules<sup>40</sup>. The network predicts a residual and adds it to the input image for reconstruction. Additional input features, including gradient map, soft histogram, over-exposure mask, and positional encodings<sup>41,42</sup>, are used to enhance the restoration quality. The positional encodings are especially helpful in addressing spatially varying aberrations of the metalens.

**Training details.** The objective function of the neural network training is defined by as follows:

$$\mathcal{L}_{\text{total}} = \mathcal{L}_{\text{L1}} + \lambda_{\text{SSIM}} \mathcal{L}_{\text{SSIM}} + \lambda_{\text{LPIPS}} \mathcal{L}_{\text{LPIPS}}, \quad (\text{S14})$$

where  $\mathcal{L}_{\text{LPIPS}}$  is the LPIPS loss<sup>43</sup>, and we set  $\lambda_{\text{SSIM}}$  and  $\lambda_{\text{LPIPS}}$  as 0.1. The neural network was trained with 4 NVIDIA RTX 6000 Ada GPUs for 60 hours. We employed the AdamW<sup>36</sup> optimizer. We set the learning rate  $\eta$  to  $5 \times 10^{-6}$ , which is adjusted following a cosine annealing schedule with warm-up and restart<sup>37</sup>, where  $T_{\text{max}}$  is set to 4000, and the linear warm-up from  $0.1\eta$  is applied for the first 10 epochs. The training is performed with a batch size of 14 per GPU. Each image was randomly cropped to a patch size of  $424 \times 424$  pixels. We applied random vertical and horizontal flips, along with random rotations. Random augmentations to brightness and contrast were applied, along with Gaussian noise with a standard deviation of  $\sigma = 5 \times 10^{-3}$ . The Gaussian noise is designed to model sensor noise, preventing the network from overfitting to the ground-truth data. Meanwhile, the photometric augmentations (brightness and contrast) are crucial for compensating for potential inconsistencies between the metalens and the ground-truth compound lens cameras. Since factors such as auto-exposure and white balancing can vary independently between the two optical systems, these augmentations encourage the network to focus on structural recovery rather than global intensity mapping, ensuring robust reconstruction performance across diverse lighting conditions.

**Training dataset.** We use printed high-resolution images with rich structural and color content from the DIV2K dataset<sup>32</sup> as ground-truth scenes for the training dataset. Obstructed scenes were captured using the metalenses, and the ground-truth scenes were acquired with a compound lens with a focal length of  $f = 8$  mm. The focal length of the compound lens is twice that of the metalenses to achieve better object space resolution<sup>44</sup>. Note that the *printed* images are used as

training data, rather than digitally displayed images, to ensure spectral fidelity in broadband imaging. Displays typically exhibit narrow spectral peaks corresponding to their RGB channels. In contrast, printed images reflect a continuous and significantly broader spectrum. Figure S8 compares the spectral radiance distribution of the printed image under a white LED light source against a display (LG 22-inch LCD monitor) for each color. This broader spectral content is essential for accurately characterizing broadband metalenses, as it prevents spectral undersampling.

The dataset is composed of 200 training and 10 validation scenes from the DIV2K dataset for each lens. For each scene, we captured one clean image and an average of six obstructed counterparts, resulting in a total of 1,400 training and 70 validation images for each metalens. Figure S30 shows the obstructions used for the neural network training. Precise pixel-wise alignment between the obstructed metalens captures and the ground-truth compound lens images is essential for the supervised learning. To acquire such alignment, we use the stereo configuration for our dataset capture setup (Figure S14). We employ a homography-based warping strategy to compensate for the spatial offset and scaling differences between the two optical paths. Since our training scenes are planar, the depth-dependent parallax remains negligible, and the spatial relationship between the two lenses are accurately modeled by a homography transformation. The homography is estimated using a set of corresponding feature points from a learning-based feature extractor<sup>45</sup> and the RANSAC<sup>46</sup> algorithm.

**Inference time and memory consumption.** We benchmarked the image reconstruction network's inference performance and memory footprint on an NVIDIA RTX 6000 Ada GPU to evaluate the practical viability of the imaging system for edge deployment. The benchmark was conducted at a resolution of  $512 \times 512$  pixels, which is a standard input resolution scale for neural networks. As summarized in Table S3, our model exhibits a throughput of 24.15 FPS when optimized, showing its suitability for high-speed imaging. The high-performance efficiency, coupled with a manageable memory footprint of 946 MiB, underscores the potential for integration into compact edge devices. Note that the throughput could be increased up to 75.44 FPS when batch-processed, with the memory consumption of 4,118 MiB.

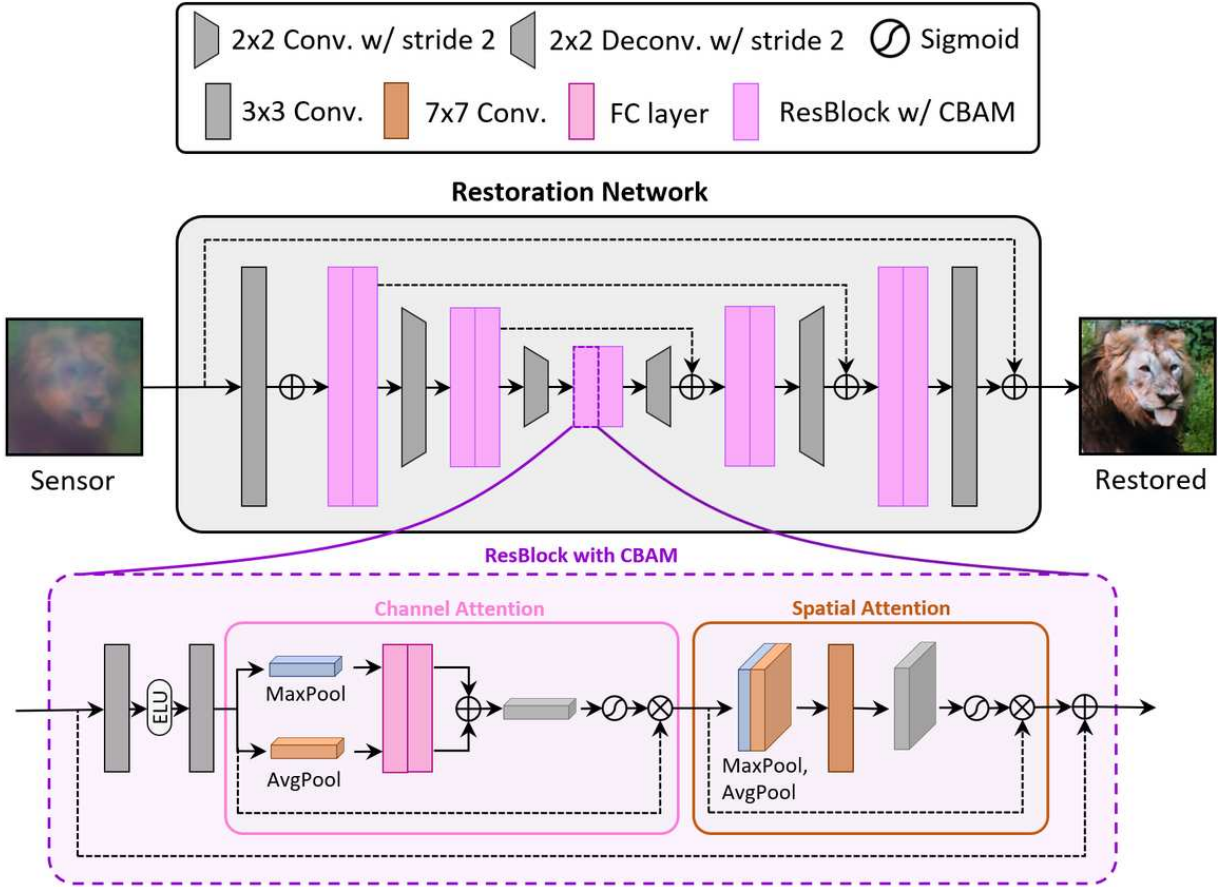


**Figure S7: Detailed architecture of the image reconstruction network.**

Precision	Batch size	Input size (pixels)	Latency (per image, ms)	Throughput (FPS)	Memory (MiB)
FP32	1	512 × 512	42.96	23.28	1,178
FP32	8	512 × 512	21.13	47.33	7,136
FP16	1	512 × 512	41.41	24.15	946
FP16	8	512 × 512	13.26	75.44	4,118

**Table S3:** Inference performance and memory (VRAM) consumption of the image reconstruction network. Benchmarks were measured on an NVIDIA RTX 6000 Ada Generation GPU at a resolution of 512 × 512 pixels. Throughput and memory footprint highlight the lightweight nature of the proposed architecture for real-time edge-device applications.

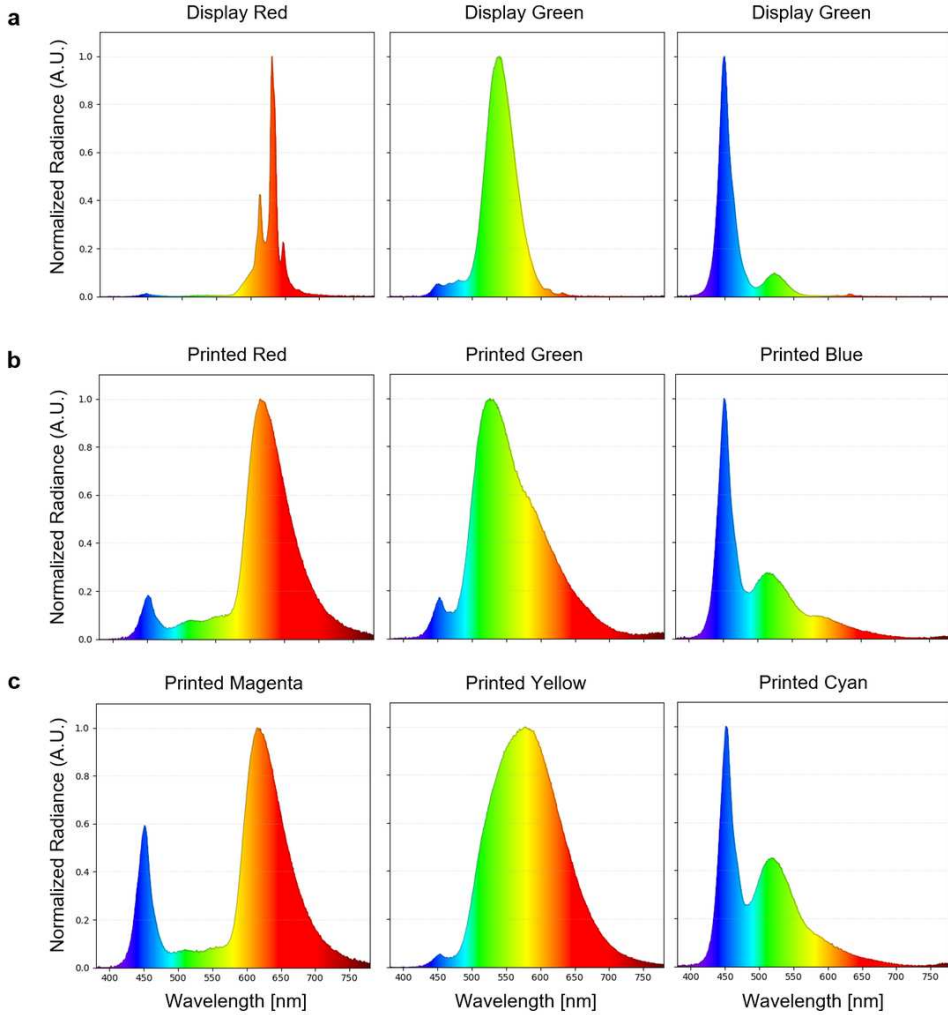


**Figure S8: Comparison of spectral radiance distribution between printed images and digital displays.** The spectral radiance of each primary color (Red, Green, and Blue) was measured with a spectroradiometer (JETI specbos 1211-2) to ensure spectral fidelity for broadband metalens characterization. **a** The digital display (LG 22-inch LCD monitor) shows narrow spectral peaks corresponding to its RGB channels, failing to represent the full continuous spectrum required for accurate broadband modeling. **b, c** Printed images under an LED light source exhibit a continuous and significantly broader spectrum, which is essential for preventing spectral undersampling during broadband imaging. We show red, green, and blue spectra along with magenta, yellow, and cyan, which are the basis colors for the printing. All curves are normalized to their respective peak intensities for clear comparison of the spectral width.

**Supplementary Note 6: Measured complex refractive index of the  $\text{SiN}_x$  film**

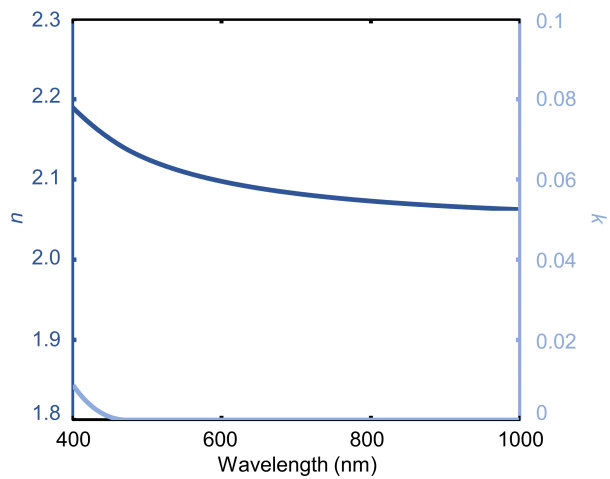


**Figure S9:** Measured refractive index and extinction coefficient of the  $\text{SiN}_x$  film.

### Supplementary Note 7: Simulated conversion efficiency under variation of geometric parameters

In this study, phase modulation is achieved using geometric phase, where each anisotropic meta-atom with an in-plane orientation  $\theta$  imparts a spatially varying phase of  $2\theta$  to the cross-polarized transmitted field. These meta-atoms are designed to function as subwavelength half-wave plates to maximize polarization conversion efficiency, which requires a  $\pi$  phase retardation between the two orthogonal eigenmodes. We evaluated the conversion efficiency using rigorous coupled-wave analysis (RCWA) by sweeping the width  $w$  from 210 nm to 360 nm and the length  $l$  from 40 nm to 190 nm, while fixing the period at  $p = 395$  nm and the height at  $h = 700$  nm, consistent with fabrication constraints. Figure S10 presents the calculated efficiency at the target wavelengths of 457 nm, 530 nm, and 628 nm. Based on these results, we selected a geometry with  $w = 305$  nm and  $l = 125$  nm, which ensures high efficiency while accommodating a fabrication tolerance of 10 nm. This design yields conversion efficiencies of 78.4%, 72.9%, and 66.9% at 457, 530, and 628 nm, respectively.

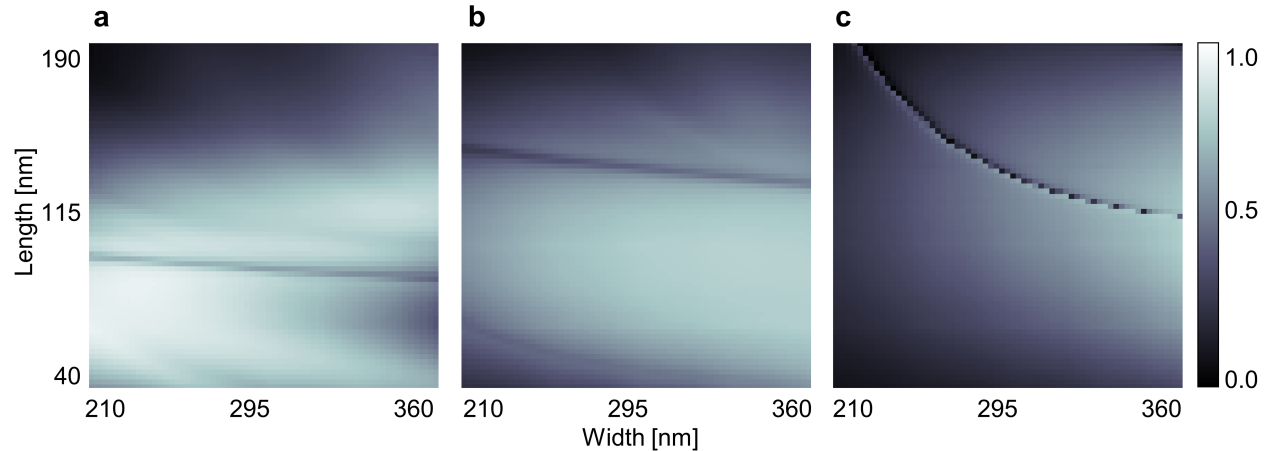


**Figure S10:** Calculated conversion efficiency of meta-atoms at wavelengths of 457 nm, 530 nm, and 628 nm, for a fixed period of 395 nm and a height of 700 nm, as function of the meta-atom width and length.

**Supplementary Note 8: Broadband property across the visible wavelength of the designed meta-atom**

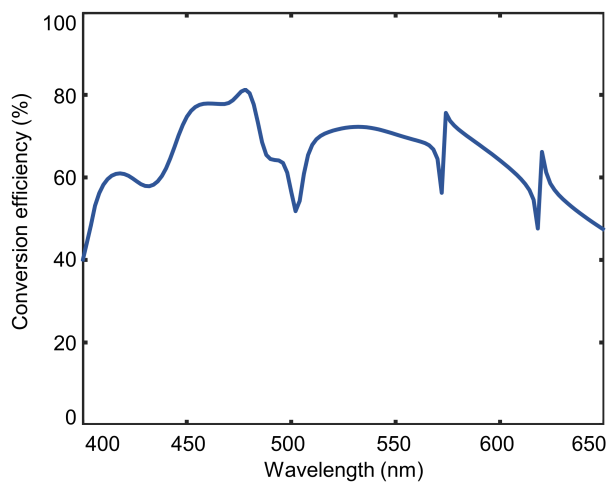


**Figure S11:** Calculated conversion efficiency of the designed meta-atom from 400 nm to 650 nm.

### Supplementary Note 9: Fabrication process of learned split-spectrum metalens

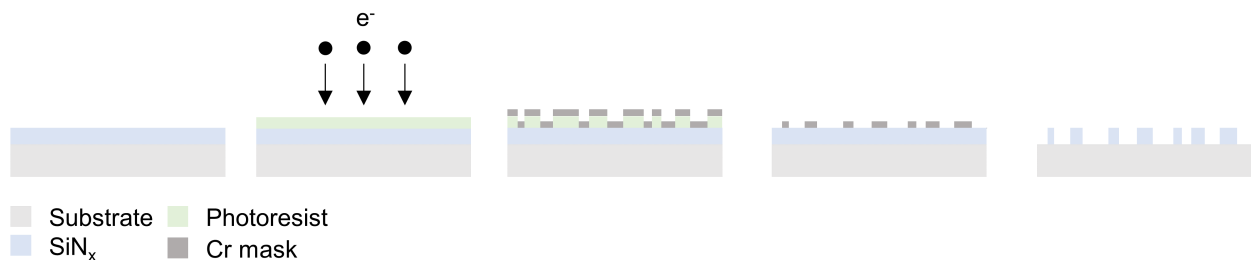


**Figure S12:** Fabrication process of learned split-spectrum metalens.

## Supplementary Note 10: Details on the experimental setup

**PSF measurement setup.** To evaluate the near- and far-depth PSFs of the proposed metalenses, we constructed a custom optical setup, as shown in Figure S13a. Specific wavelengths were selected using a supercontinuum laser (SuperK FIANIUM, NKT Photonics) combined with a tunable bandpass filter (LLTF contrast, NKT Photonics). After the left-handed circularly polarized (LCP) beam was generated using a linear polarizer (Thorlabs, LPVISE050-A) and a quarter-wave plate (Thorlabs, AQWP05M-600), the beam was expanded and spatially cropped to uniformly illuminate the metalens aperture. Under normal incidence, the metalenses focused the incident beam, and the focal distribution was imaged onto an sCMOS camera (pco.panda 4.2 bi UV, Excelitas Technologies) using a commercial objective lens (Olympus, LUCPLFLN20X) and a tube lens (TTL180-A, Thorlabs). An analyzer suppressed the co-polarized component, such that only the cross-polarized PSF was recorded.

For near-depth measurements, a concave lens was inserted between the iris and the metalens to generate a spherical wavefront, while the remainder of the setup remained unchanged (Figure S13b). A hyperbolic metalens was used to define the reference focal plane at 4 mm and a near-depth distance of 0.045 m, under which the PSFs of both learned metalenses were measured. Minor wavelength-dependent shifts and slight focusing degradation are attributed to the non-ideal FWHM (1.5 nm) of the supercontinuum laser’s spectral filter, the interpolation effect of 5 nm spectral resolution, and subtle misalignment among optical components.

**Imaging setup.** Figure S14 illustrates our imaging prototype, which consists of a dual-path (stereo) setup to allow simultaneous capture of ground-truth (GT) and metalens-based images. A high-resolution 2D scene target from the DIV2K dataset or in-the-wild objects are illuminated by an LED light source. The ground-truth path utilizes a high-quality compound lens with a focal length of  $f = 8$  mm, while the other path employs our metalens with a focal length of  $f = 4$  mm. This focal length ratio (2:1) is chosen to provide superior object-space resolution for the ground truth reference<sup>44</sup>. The metalens imaging arm contains the near-depth obstruction (mimicking dirt, blood, and fences) placed at a distance of  $z_{\text{near}} = 0.045$  m from the metalens plane. The far-depth target is located at  $z_{\text{far}} \simeq 0.6$  m. LCP filter and RCP analyzer, consist of a linear polarizer (Edmund Optics, XP42-18) and a quarter-wave plate (50.8 mm Dia, 450 - 650 nm,  $\lambda/4$  Achromatic Waveplate), are employed to fulfill the conditions for the Pancharatnam-Berry (PB) phase modulation. A 10 $\times$  microscope objective (Nikon, N10X-PF) and tube lens (Thorlabs, TTL100-A) are employed as a relay optic to accommodate the placement of intermediate optic elements. The multi-band spectral filter (Edmund Optics, 457, 530 & 628 nm, 50 mm Dia., Tri-Band Filter) is adopted for the learned split-spectrum metalens captures, and removed for baseline metalens captures. Sony IMX226 CMOS is employed for the compound lens camera, and Sony IMX304 CMOS is used for the metalens camera. Note that the optical filters can be designed to be thin and flat, allowing them to be attached directly to the sensor to maintain a compact form factor.

Images are captured at 1 fps for in-the-wild scenes and at 1.5 fps for printed targets. Due to the  $10\times$  objective lens, the incident light is reduced by approximately  $\frac{1}{100}$ , which in principle allows the frame rate to be increased by up to  $\sim 100\times$  (i.e., to 100 fps and 150 fps for the two capture settings, respectively).

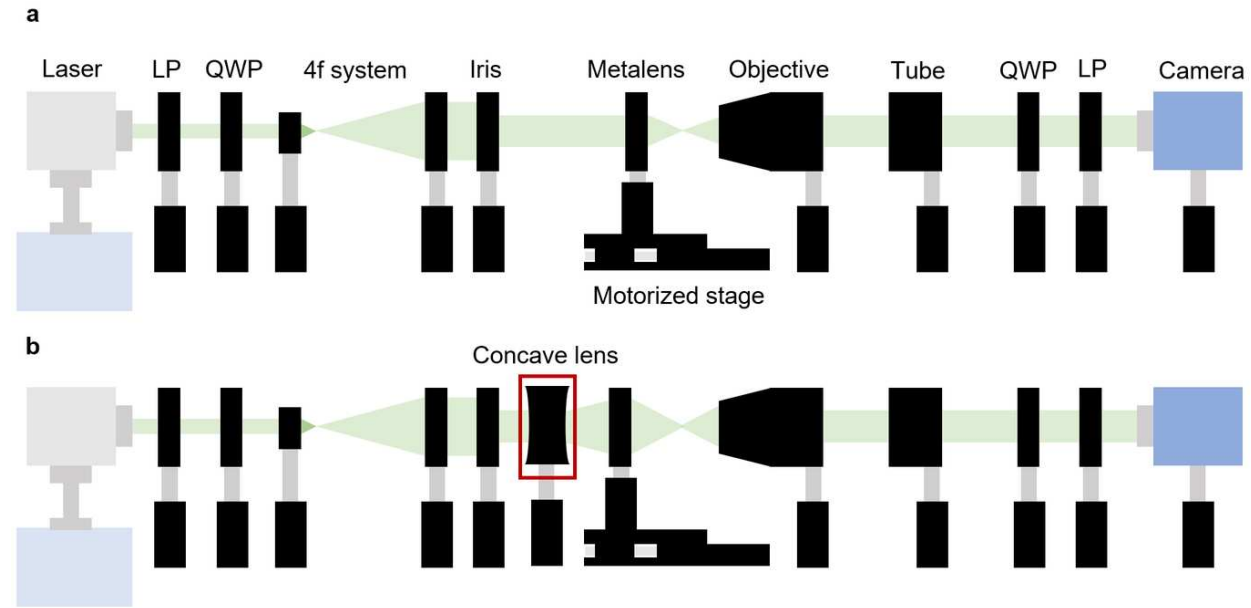


**Figure S13: Schematic of the custom-built PSF measurement system.** The setup includes a supercontinuum source, polarization control optics (LP and QWP), and a beam expansion stage. **a** Configuration for far-depth characterization under normal collimated incidence. **b** Near-depth measurement configuration where a concave lens is utilized to generate a spherical wave.

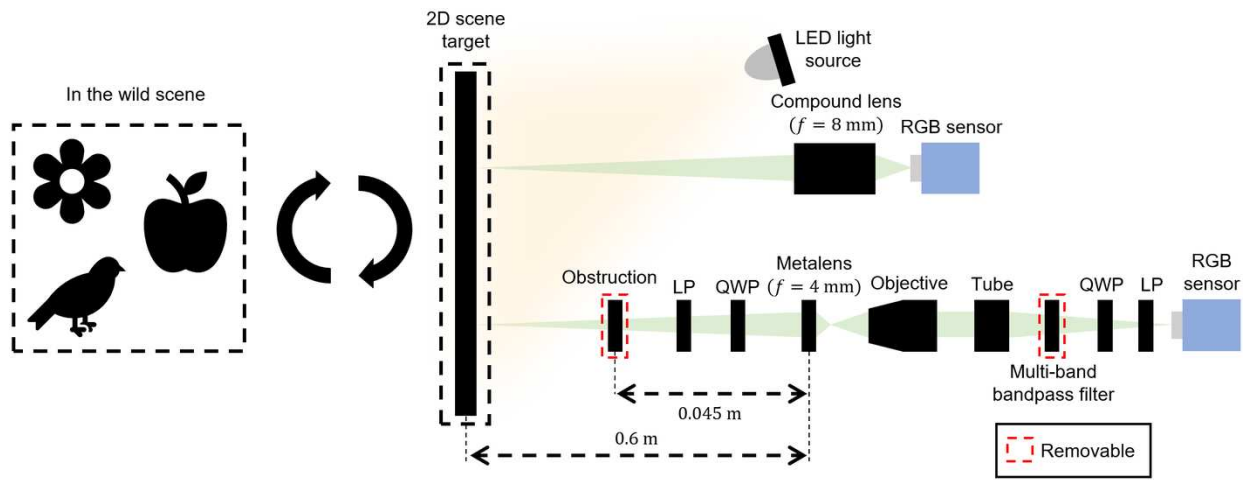


**Figure S14: Schematic of the custom-built imaging system.** The imaging system is configured in a stereo setup to capture ground-truth (GT) and metalens-based images simultaneously. The GT path utilizes a high-quality compound lens to acquire GT reference images of the targets, ensuring superior object-space resolution. The metalens path contains the fabricated metalens for obstruction-free imaging. The scene is placed at a distance of approximately 0.6 m,  $z_{\text{far}}$ , from the lenses, and removable near-depth obstructions are positioned at 0.045 m,  $z_{\text{near}}$ , from the metalens plane. The multi-band spectral filter is adopted for the learned split-spectrum metalens captures, and removed for baseline metalens captures. The targets are illuminated by an LED light source.

## Supplementary Note 11: Details on the image quality assessment

We measure PSNR, SSIM, and LPIPS<sup>43</sup> for two representative obstructions: dirt (blob-like occluders) and fence (thin and structured occluders), which jointly span common near-depth obstruction geometries that provide a generalizable assessment of imaging fidelity. We consider (i) the compound lens GT image, (ii) the metalens unobstructed capture, (iii) the metalens obstructed capture, and (iv) the reconstructed output produced by the corresponding method. We compute metrics for each lens design: hyperbolic phase metalens (Hyperbolic), learned broadband metalens without the split-spectrum strategy (Broadband), and the learned split-spectrum metalens (Ours, split-spectrum), and for each obstruction type (e.g., fence, dirt) using the same alignment protocol described below, ensuring fair comparisons across all conditions. Due to the time-intensive nature of the optical acquisition process, we evaluate a subset of  $N = 10$  printed scenes per obstruction type and per lens design. For each scene, we capture both unobstructed and obstructed metalens images, and we additionally evaluate the corresponding reconstructed outputs. Qualitative examples are shown in Figures S27 and S28, and quantitative results are summarized in Table S4. The quantitative results demonstrate that our split-spectrum design achieves superior robustness against obstructions compared to baseline methods. Analyzing the performance gap ( $\Delta$ ) between unobstructed and obstructed conditions, our method overall exhibits the minimal degradation across all metrics and conditions, validating the resilience of our method against obstructions.

**Precise alignment for image quality measurement.** Because these metrics assume pixel-wise correspondence, accurate geometric alignment between the two imaging paths is critical. We employ a two-stage warping procedure: a global homography for coarse alignment (consistent with the neural network training pipeline in Supplementary Note 5), followed by a non-linear refinement for precise metric measurements. While a homography is sufficient for planar alignment in principle, we observed small residual misregistrations that can bias full-reference metrics, due to practical factors such as mild lens distortion, imperfect planarity of printed targets. Therefore, we apply an additional non-linear warping step based on a thin-plate spline (TPS) deformation field initialized from the homography-aligned pair. All reported metrics in Table S4 are computed after applying this identical alignment procedure across all lenses, obstructions, and image conditions.

**Photometric normalization for fair full-reference evaluation.** Full-reference metrics such as PSNR, SSIM, and LPIPS assume not only pixel-wise geometric correspondence but also comparable photometric scaling. In our setting, images are acquired through different optical paths and re-captured from printed targets, which can introduce global exposure and contrast shifts unrelated to imaging performance. To mitigate such global photometric offsets, we apply a temporary per-image photometric normalization prior to metric computation: given an aligned reference image and a target image, we estimate an affine intensity transform (gain and bias) using the luminance mean and standard deviation of the reference, and apply the same gain/bias to the target image. All reported PSNR/SSIM/LPIPS values are computed after this photometric matching, while the underlying geometry and spatial content remain unchanged. We apply the same procedure

consistently across all lens designs, obstruction types, and conditions (raw/reconstructed, unobstructed/obstructed) to ensure fair comparisons. This normalization only compensates for global brightness differences and does not correct local artifacts or structural misalignment; therefore, it does not artificially improve the metrics beyond removing trivial photometric bias.

**Qualitative observations.** As shown in Figures S27 and S28, obstruction patterns (dirt blobs and fence-like grids) strongly corrupt raw metalens captures and can propagate into reconstructions for baseline lens designs. In contrast, the split-spectrum metalens maintains visually consistent reconstructions across unobstructed and obstructed inputs, exhibiting substantially reduced obstruction imprint and improved structural fidelity. These qualitative trends align with the quantitative improvements in PSNR/SSIM and reductions in LPIPS reported in Table S4, particularly under obstructed conditions.

Lens design	Capture Condition	Dirt Obstruction			Fence Obstruction		
		PSNR (↑)	SSIM (↑)	LPIPS (↓)	PSNR (↑)	SSIM (↑)	LPIPS (↓)
		Unobs.	0.2840	0.8890	10.89	0.2873	0.8800
Hyperbolic	Raw	Obs.	9.73	0.2678	0.9201	10.56	0.2756
		Δ (Drop)	-1.08	-0.0162	-0.0311	-0.33	-0.0117
		Unobs.	18.77	0.7034	0.4640	19.01	0.7108
	Recon.	Obs.	15.98	0.6261	0.5419	15.67	0.6074
		Δ (Drop)	-2.79	-0.0773	-0.0779	-3.34	-0.1034
		Unobs.	15.00	0.3804	0.8478	14.98	0.3783
Broadband	Raw	Obs.	14.14	0.3553	0.8799	14.36	0.3537
		Δ (Drop)	-0.86	-0.0251	-0.0321	-0.62	-0.0246
		Unobs.	22.77	0.7521	0.4023	22.97	0.7526
	Recon.	Obs.	18.40	0.6725	0.4775	19.17	0.6498
		Δ (Drop)	-4.37	-0.0796	-0.0752	-3.80	-0.1028
		Unobs.	15.58	0.4458	0.7221	15.30	0.4256
Ours (Split-spectrum)	Raw	Obs.	15.15	0.4198	0.7559	14.72	0.4020
		Δ (Drop)	-0.43	-0.0260	-0.0338	-0.58	-0.0236
		Unobs.	23.60	0.8282	0.2939	23.21	0.8129
	Recon.	Obs.	21.20	0.7803	0.3529	20.67	0.7316
		Δ (Drop)	-2.40	-0.0479	-0.0590	-2.54	-0.0813
		Unobs.	23.60	0.8282	0.2939	23.21	0.8129

**Table S4: Quantitative comparison of obstruction robustness.** We consider (i) the compound lens GT image, (ii) the metalens unobstructed capture, (iii) the metalens obstructed capture, and (iv) the reconstructed output produced by the corresponding method. We compute metrics for each lens design: hyperbolic phase metalens (Hyperbolic), learned broadband metalens without the split-spectrum strategy (Broadband), and the learned split-spectrum metalens (Ours, split-spectrum), and for each obstruction type (e.g., fence, dirt). We define the metric gap as  $\Delta = \text{Obs} - \text{Unobs}$  for PSNR/SSIM and  $\Delta = \text{Unobs} - \text{Obs}$  for LPIPS, so that a more negative  $\Delta$  indicates larger degradation under obstruction and values closer to zero indicate higher robustness.

## Supplementary Note 12: Details on the downstream vision tasks

We assess the practical utility and impact of obstruction-free imaging beyond perceptual image quality by evaluating downstream vision tasks on the images captured with the three metalenses: hyperbolic phase metalens (Hyperbolic), learned broadband metalens without the split-spectrum strategy (Broadband), and the learned split-spectrum metalens (Ours). We assess the detrimental effect of obstructions by presenting the performance under both unobstructed and obstructed conditions, alongside the performance drop  $\Delta$  and its relative ratio. We benchmark three scenarios: (1) Object detection<sup>47</sup> on drone-captured aerial imagery using VisDrone<sup>48</sup>, occluded by fence obstruction, (2) Semantic segmentation for medical endoscopy<sup>49</sup> on Kvasir-SEG<sup>50</sup>, occluded by blood drops, and (3) Autonomous driving<sup>51</sup> on Cityscapes<sup>52</sup> occluded by dirt obstruction. These scenarios reflect common deployment settings in compact systems where near-depth occluders (e.g., fences, dirt, droplets) can persist, and manual cleaning is undesirable or infeasible due to space constraints, which demands optical obstruction-free imaging, such as UAVs, mobile robots, and endoscopic probes. We visualize the obstructions used for the image captures in Figure S30. Each task differs fundamentally, ranging from bounding box localization for object detection to pixel-wise classification for semantic segmentation, including both single-class and multi-class settings; therefore, we report distinct, widely accepted metrics tailored to each domain. We do not fine-tune any models on our metalens-captured data; instead, we evaluate using the released model implementations trained on their original datasets, providing only our captured images as test inputs to ensure universality.

We follow a consistent evaluation protocol for all three downstream tasks: we print the validation images from each benchmark dataset and then re-capture the printed targets using each fabricated metalens under both unobstructed and obstructed capture settings. Due to the time-intensive nature of the optical acquisition process, we evaluate on a randomly sampled subset of the validation images. Specifically, for Cityscapes and VisDrone, we capture 10 unobstructed and 10 obstructed validation images for each lens. For Kvasir-SEG, we capture 14 unobstructed and 14 obstructed validation images for each lens. For evaluation, we warp the digital ground truth images and labels onto the metalens-captured images, as described in Supplementary Note 5.

**Object Detection: VisDrone.** We utilize the VisDrone dataset<sup>48</sup> for the aerial surveillance scenario, which presents significant challenges due to small object scales and high density. We simulate fence obstruction for this scenario and employ YOLOv11<sup>47</sup>, a state-of-the-art real-time object detector, for prediction. We utilize Recall and Mean Average Precision (mAP) as evaluation metrics. Recall measures the model’s ability to capture all present objects, while mAP provides a holistic measure of localization and classification accuracy. We report mAP at IoU threshold of 0.5 (mAP<sub>50</sub>) and averaged from 0.5 to 0.95 (mAP<sub>50-95</sub>). Table S5 presents the metrics and performance degradation  $\Delta$ . Our split-spectrum metalens consistently exhibits superior performance and robustness.

Consistent with the quantitative trends in Table S5, the qualitative visualizations in Figures S15 and S16 show that the fence occluder severely disrupts object detection for the Hyperbolic and Broadband baselines, resulting in missed detections and unstable bounding box localization. In contrast, our split-spectrum metalens maintains visually consistent predictions between the unobstructed and obstructed captures, demonstrating robustness to near-depth fence occlusion.

We report  $mAP_{50}$  as the primary metric in the main text, as it better reflects object visibility recovery without heavily penalizing minor localization errors from structural variations in restored regions.

**Semantic Segmentation: Kvasir-SEG.** We utilize the Kvasir-SEG dataset<sup>50</sup> to evaluate obstruction-free imaging in a medical endoscopy scenario, where reliable delineation of polyps is critical for downstream diagnosis and intervention. This task corresponds to single-class (binary) semantic segmentation, where each pixel is classified as polyp or background. To emulate realistic near-depth occlusions encountered in endoscopy, we simulate blood drop obstructions placed close to the imaging system, which degrade contrast and obscure fine boundaries. We employ a dedicated medical segmentation model, MS2Net<sup>49</sup> to produce predictions from the captured images. We report Intersection-over-Union (IoU) and F1 score (Dice) as evaluation metrics. IoU measures the overlap between the predicted and ground-truth masks relative to their union, while F1 score (Dice) normalizes by the average size of the two masks. Table S6 summarizes the performance under unobstructed and obstructed conditions, together with the performance drop  $\Delta$  and its relative ratio. Our split-spectrum metalens maintains segmentation accuracy under blood-drop occlusions, while baseline designs suffer substantial performance degradation.

The training strategy for the released model utilizes only minimal geometric augmentations (e.g., RandomCrop, RandomFlip, and RandomRotation), which limits its generalization capability against the domain shifts—such as color bias and sensor noise—introduced by our print-and-capture setup. To assess the system performance using a segmentation network optimized to its full potential, we retrained the model on the original Kvasir-SEG training dataset with a comprehensive augmentation strategy. We incorporated ColorJitter, GaussianNoise, MotionBlur, GaussianBlur, ElasticDeform, and RandomScale, in addition to the original RandomCrop, RandomFlip, and RandomRotation.

As shown in Table S6, the split-spectrum metalens achieves reliable segmentation performance in both IoU and F1 metrics across unobstructed and obstructed conditions, while baseline designs suffer substantial degradation under blood-drop occlusions.

This robustness is also evident in the qualitative results (Figures S17–S18 (obstructed) and Figures S19–S20 (unobstructed)). Under blood-drop occlusion, the Hyperbolic and Broadband baselines often exhibit visibly corrupted masks, where occluder-induced appearance changes either distort polyp boundaries or introduce spurious activations; in several cases, the obstruction pat-

tern is effectively baked into the predicted segmentation. In contrast, our split-spectrum metalens produces segmentations that remain consistent between unobstructed and obstructed captures, as reported in Table S6.

**Semantic Segmentation: Cityscapes.** We utilize the Cityscapes dataset<sup>52</sup> to evaluate obstruction-free imaging in an autonomous driving scenario, where reliable multi-class semantic segmentation is essential for scene understanding. This task corresponds to multi-class pixel-wise classification over diverse urban categories (e.g., roads, pedestrians, vehicles, and traffic infrastructure). We simulate dirt obstruction placed close to the imaging system, which is a realistic near-depth contamination encountered in outdoor sensing that introduces spatially varying attenuation and color bias and can severely corrupt safety-critical regions. We employ a state-of-the-art semantic segmentation model, InternImage-H (using the Mask2Former segmentation method)<sup>51</sup> to produce predictions from the captured images.

We report average accuracy (aAcc) and mean Intersection-over-Union (mIoU) as evaluation metrics. aAcc reflects pixel-level classification correctness aggregated across classes, whereas mIoU averages the per-class IoU to provide a metric robust to class imbalance, preventing large-area classes from dominating the score. Table S7 summarizes performance under unobstructed and obstructed conditions, together with the performance drop  $\Delta$  and its relative ratio.

When reporting mIoU, we exclude classes with NaN or 0 IoU values to avoid instability from limited sampling. In our setting, NaN typically arises when the ground-truth contains no pixels of a class, yielding an undefined IoU (divide by zero). In contrast, an IoU of 0 occurs when the ground-truth for a class is absent ( $TP = 0$ ), but the model produces non-zero predictions, resulting in  $0/N = 0$ . We apply this filtering consistently across all lens designs for a fair comparison. Specifically, the excluded classes are [Wall, Fence, Traffic Light, Terrain, Truck, Train, Motorcycle]. Table S8 reports the full per-class IoU and the corresponding drop, highlighting that our split-spectrum metalens maintains strong performance, especially for safety-critical classes such as Person, Rider, Car, and Bus. We also report pixel-level average accuracy (aAcc), which aggregates correctness over all pixels and provides a stable measure of overall segmentation performance.

Qualitative comparisons further support these trends (Figures S21 and S22). For the Hyperbolic and Broadband baselines, the near-depth dirt occluders introduce strong spatially varying attenuation and color bias that propagate to the predictions, producing holes and spurious regions; the occluder is partially baked into the predicted labels. In contrast, our split-spectrum metalens yields predictions that remain visually consistent across unobstructed and obstructed captures, with minimal degradation in both scene layout and safety-critical categories, aligning with the smaller drops in Table S7.

<b>Lens Design</b>	<b>Condition</b>	<b>Recall (↑)</b>	<b>mAP<sub>50</sub> (↑)</b>	<b>mAP<sub>50-95</sub> (↑)</b>
Hyperbolic	Unobstructed	0.2347	0.2175	0.1308
	Obstructed	0.1109	0.0350	0.0170
	Δ (Drop)	-0.1238 (-52.7%)	-0.1825 (-83.9%)	-0.1138 (-87.0%)
Broadband	Unobstructed	0.0893	0.1066	0.0644
	Obstructed	0.0178	0.0292	0.0135
	Δ (Drop)	-0.0715 (-80.1%)	-0.0774 (-72.6%)	-0.0509 (-79.0%)
<b>Ours (Split-spectrum)</b>	<b>Unobstructed</b>	<b>0.2331</b>	<b>0.2427</b>	<b>0.1354</b>
	<b>Obstructed</b>	<b>0.1784</b>	<b>0.1704</b>	<b>0.0889</b>
	Δ (Drop)	-0.0546 (-23.4%)	-0.0723 (-29.8%)	-0.0465 (-34.3%)

**Table S5: Quantitative comparison of downstream object detection performance on VisDrone under unobstructed and obstructed imaging conditions.** We report Recall and mean average precision (mAP) at multiple IoU thresholds for three metalens designs. Due to acquisition constraints, evaluation is performed on 10 sampled validation images.

**Metric Definitions:**

**Recall (↑):** The ratio of correctly predicted positive observations to all observations in the actual class, representing the ability of the lens to capture all objects in the scene.

**mAP<sub>50</sub> (↑)** Mean Average Precision calculated at an Intersection over Union (IoU) threshold of 0.5 averaged over classes, where the Precision is the ratio of correctly predicted positive observations to the total predicted positives, indicating the accuracy of the detection.

**mAP<sub>50-95</sub> (↑)** Mean Average Precision averaged over multiple IoU thresholds (from 0.5 to 0.95) averaged over classes, providing a comprehensive measure of localization and classification accuracy.

**Δ (Drop):**  $\Delta = \text{Obstructed} - \text{Unobstructed}$  (negative values indicate performance degradation). The **Drop ratio** is computed as  $\frac{\Delta}{\text{Unobstructed}} \times 100\%$ .

<b>Lens Design</b>	<b>Condition</b>	<b>IoU (↑)</b>	<b>F1 score (↑)</b>
Hyperbolic	Unobstructed	0.8080	0.8616
	Obstructed	0.3472	0.6100
	Δ (Drop)	-0.4608 (-57.0%)	-0.2516 (-29.2%)
Broadband	Unobstructed	0.8199	0.9042
	Obstructed	0.5950	0.8036
	Δ (Drop)	-0.2249 (-27.4%)	-0.1006 (-11.1%)
<b>Ours (Split-spectrum)</b>	<b>Unobstructed</b>	<b>0.8356</b>	<b>0.9075</b>
	<b>Obstructed</b>	<b>0.8317</b>	<b>0.9154</b>
	Δ (Drop)	-0.0039 (-0.5%)	+0.0079 (0.9%)

**Table S6: Quantitative comparison of downstream semantic segmentation performance on Kvasir-SEG under unobstructed and obstructed imaging conditions.** We report Intersection-over-Union (IoU) and F1 score (Dice) for Kvasir-SEG segmentation results obtained from images captured with three metalens designs. Due to acquisition constraints, evaluation is performed on 14 sampled validation images.

**Metric Definitions:**

**IoU (↑):**  $\text{IoU} = \frac{|P \cap G|}{|P \cup G|} = \frac{\text{TP}}{\text{TP} + \text{FP} + \text{FN}}$ , where  $P$  and  $G$  denote the predicted and ground-truth masks, respectively.

**F1 score (↑):**  $\text{F1} = \frac{2|P \cap G|}{|P| + |G|} = \frac{2\text{TP}}{2\text{TP} + \text{FP} + \text{FN}}$  (equivalently, the Dice coefficient).

**Δ (Drop):**  $\Delta = \text{Obstructed} - \text{Unobstructed}$  (negative values indicate performance degradation). The **Drop ratio** is computed as  $\frac{\Delta}{\text{Unobstructed}} \times 100\%$ .

<b>Lens Design</b>	<b>Condition</b>	<b>aAcc (↑)</b>	<b>mIoU (↑)</b>
Hyperbolic	Unobstructed	0.8516	0.6001
	Obstructed	0.7288	0.4666
	Δ (Drop)	-0.1228 (-14.4%)	-0.1335 (-22.2%)
Broadband	Unobstructed	0.8410	0.5942
	Obstructed	0.7339	0.4601
	Δ (Drop)	-0.1071 (-12.7%)	-0.1341 (-22.6%)
<b>Ours (Split-spectrum)</b>	<b>Unobstructed</b>	<b>0.9088</b>	<b>0.7080</b>
	<b>Obstructed</b>	<b>0.8835</b>	<b>0.6701</b>
	Δ (Drop)	-0.0253 (-2.8%)	-0.0379 (-5.4%)

**Table S7: Quantitative comparison of downstream semantic segmentation performance on Cityscapes under unobstructed and obstructed imaging conditions.** This table evaluates the segmentation fidelity across three metalens designs using average accuracy (aAcc) and mean intersection over union (mIoU). mIoU is calculated by excluding classes reported as outliers (zero or NaN values) to ensure statistical reliability. Due to acquisition constraints, evaluation is performed on 10 sampled validation images.

**Metric Definitions:**

**aAcc (↑):** Average Accuracy, representing the mean of the correctly classified pixels for each class across the scene.

**mIoU (↑):** Mean Intersection over Union, the average of the ratios between the intersection and union of the predicted and ground-truth segments. In this report, mIoU values are calculated by excluding outlier classes with zero or NaN values to provide a more stable performance comparison.

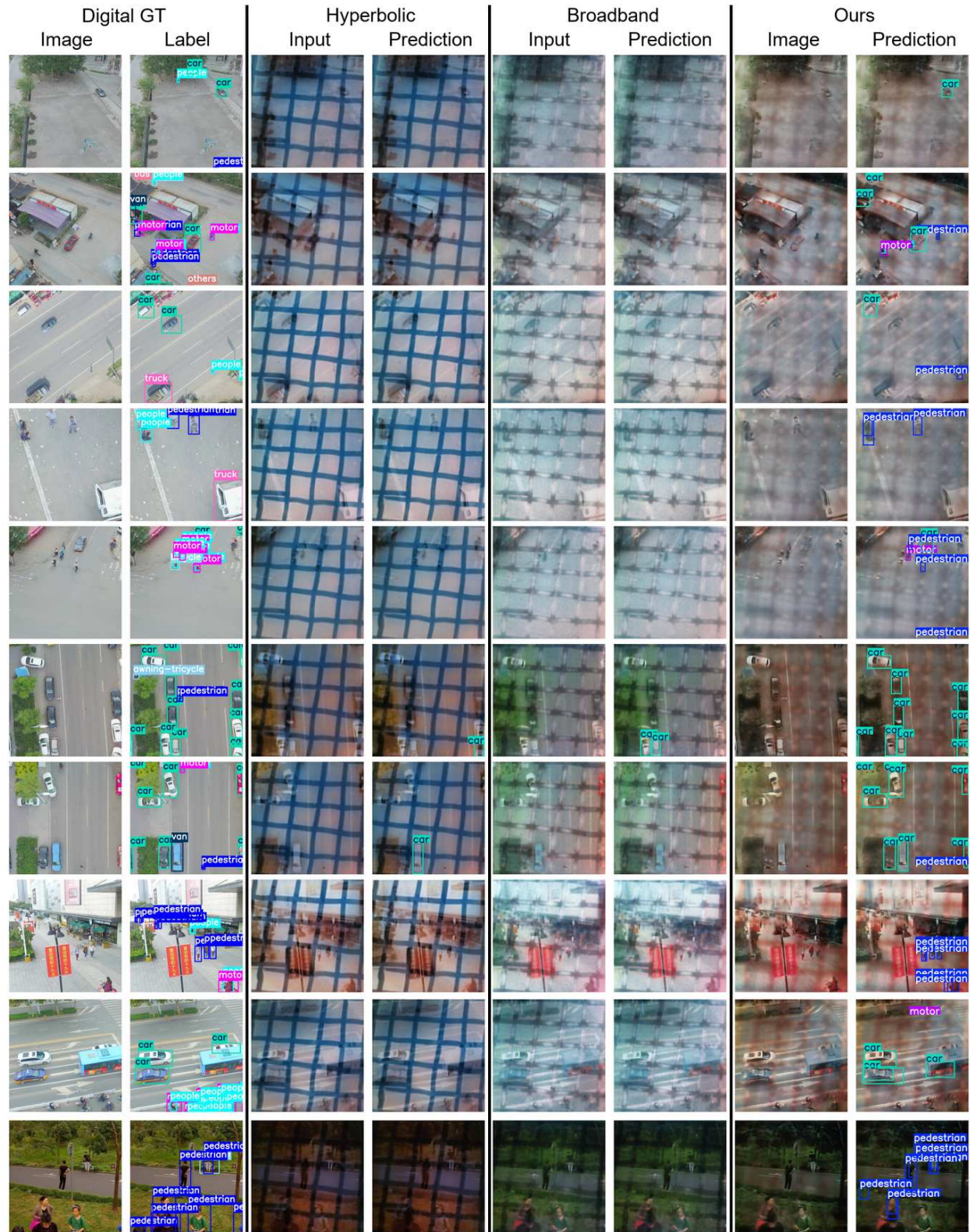
**Δ (Drop):**  $\Delta = \text{Obstructed} - \text{Unobstructed}$  (negative values indicate performance degradation). The **Drop ratio** is computed as  $\frac{\Delta}{\text{Unobstructed}} \times 100\%$ .

Class	Hyperbolic			Broadband			Ours (Split-spectrum)		
	Unobs.	Obs.	$\Delta$ (Drop)	Unobs.	Obs.	$\Delta$ (Drop)	Unobs.	Obs.	$\Delta$ (Drop)
Road	0.8484	0.7070	-0.1414 (-16.7%)	0.8408	0.7200	-0.1208 (-14.4%)	0.9662	0.8579	-0.1083 (-11.2%)
Sidewalk	0.2128	0.1019	-0.1109 (-52.1%)	0.2025	0.1034	-0.0991 (-48.9%)	0.6262	0.2275	-0.3987 (-63.7%)
Building	0.6965	0.5298	-0.1667 (-23.9%)	0.6477	0.5172	-0.1305 (-20.1%)	0.7165	0.7915	+0.0750 (+10.5%)
Wall	0.1108	0.0000	-0.1108 (-100.0%)	0.6940	0.5147	-0.1793 (-25.8%)	0.2630	0.7013	+0.4383 (+166.7%)
Pole	0.1165	0.0844	-0.0321 (-27.6%)	0.1425	0.1027	-0.0398 (-27.9%)	0.2436	0.1899	-0.0537 (-22.0%)
Traffic Light	0.3179	0.1622	-0.1557 (-49.0%)	0.0000	0.0000	+0.0000 (N/A)	0.6312	0.3940	-0.2372 (-37.6%)
Traffic Sign	0.0728	0.0540	-0.0188 (-25.8%)	0.1045	0.0561	-0.0484 (-46.3%)	0.4265	0.4175	-0.0090 (-2.1%)
Vegetation	0.7614	0.5622	-0.1992 (-26.2%)	0.7237	0.6008	-0.1229 (-17.0%)	0.8740	0.8243	-0.0497 (-5.7%)
Terrain	0.0000	0.0000	+0.0000 (N/A)	0.0000	0.0000	+0.0000 (N/A)	0.2667	0.2382	-0.0285 (-10.7%)
Sky	0.8923	0.5635	-0.3288 (-36.8%)	0.9184	0.6647	-0.2537 (-27.6%)	0.9267	0.9227	-0.0040 (-0.4%)
Person	0.8509	0.6881	-0.1628 (-19.1%)	0.8212	0.5956	-0.2256 (-27.5%)	0.8561	0.8720	+0.0159 (+1.9%)
Rider	0.6871	0.4328	-0.2543 (-37.0%)	0.6474	0.3223	-0.3251 (-50.2%)	0.6971	0.6724	-0.0247 (-3.5%)
Car	0.8604	0.7776	-0.0828 (-9.6%)	0.8579	0.7899	-0.0680 (-7.9%)	0.8935	0.8872	-0.0063 (-0.7%)
Bus	0.9006	0.9159	+0.0153 (+1.7%)	0.9301	0.9109	-0.0192 (-2.1%)	0.9600	0.9551	-0.0049 (-0.5%)
Motorcycle	0.5852	0.0000	-0.5852 (-100.0%)	0.4893	0.0000	-0.4893 (-100.0%)	0.3199	0.6894	+0.3695 (+115.5%)
Bicycle	0.3101	0.1819	-0.1282 (-41.3%)	0.2937	0.1380	-0.1557 (-53.0%)	0.3091	0.4297	+0.1206 (+39.0%)

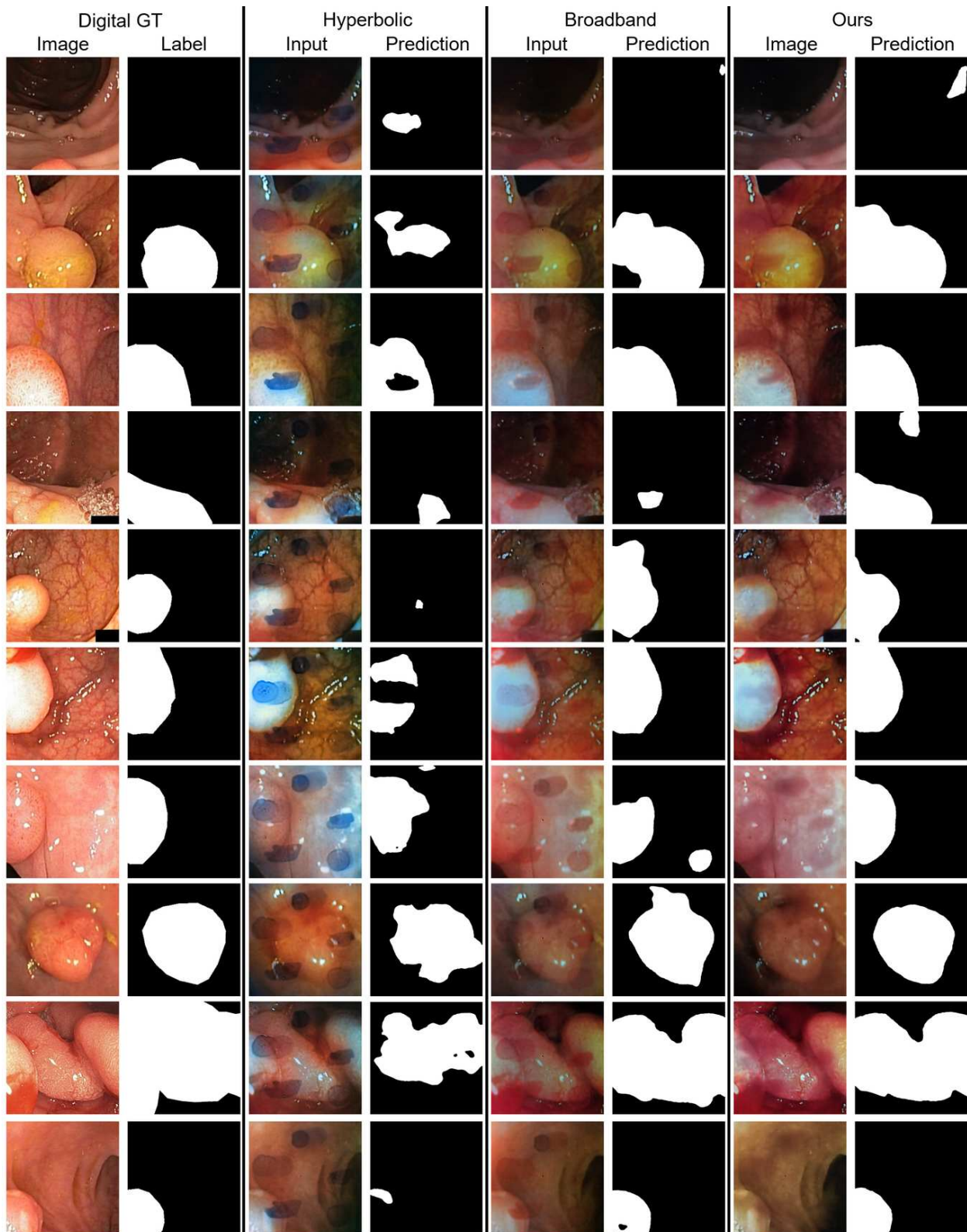
**Table S8: Class-wise semantic segmentation performance (per-class IoU) on Cityscapes under unobstructed and obstructed imaging conditions.** Per-class Intersection-over-Union (IoU) is reported for three lens designs.  $\Delta$  (Drop):  $(\Delta = \text{IoU}_{\text{obs}} - \text{IoU}_{\text{unobs}})$  represents the performance change, with the relative change (Drop ratio) shown in parentheses as  $(\Delta/\text{IoU}_{\text{unobs}}) \times 100\%$ . The entry N/A (Not Applicable) indicates that a relative ratio could not be determined due to a zero denominator. Classes that are not included in the ground-truth label in the captured subset (Fence, Truck, and Train) are not presented in the table.

**Metric definition:**

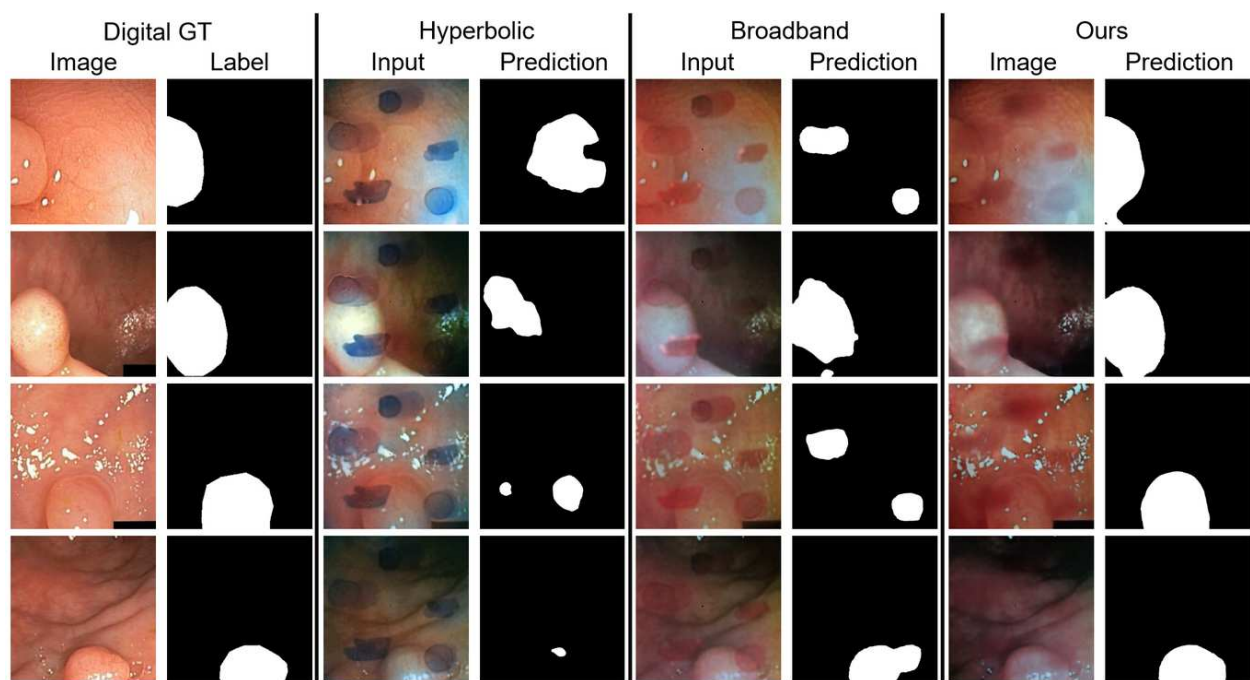
**N/A:** Denotes missing data or undefined statistical ratios, ensuring clear distinction from zero-value measurements.  
 **$\Delta$  (Drop):** The signed percentage change relative to the unobstructed baseline; a smaller negative value indicates higher lens robustness against obstructions.



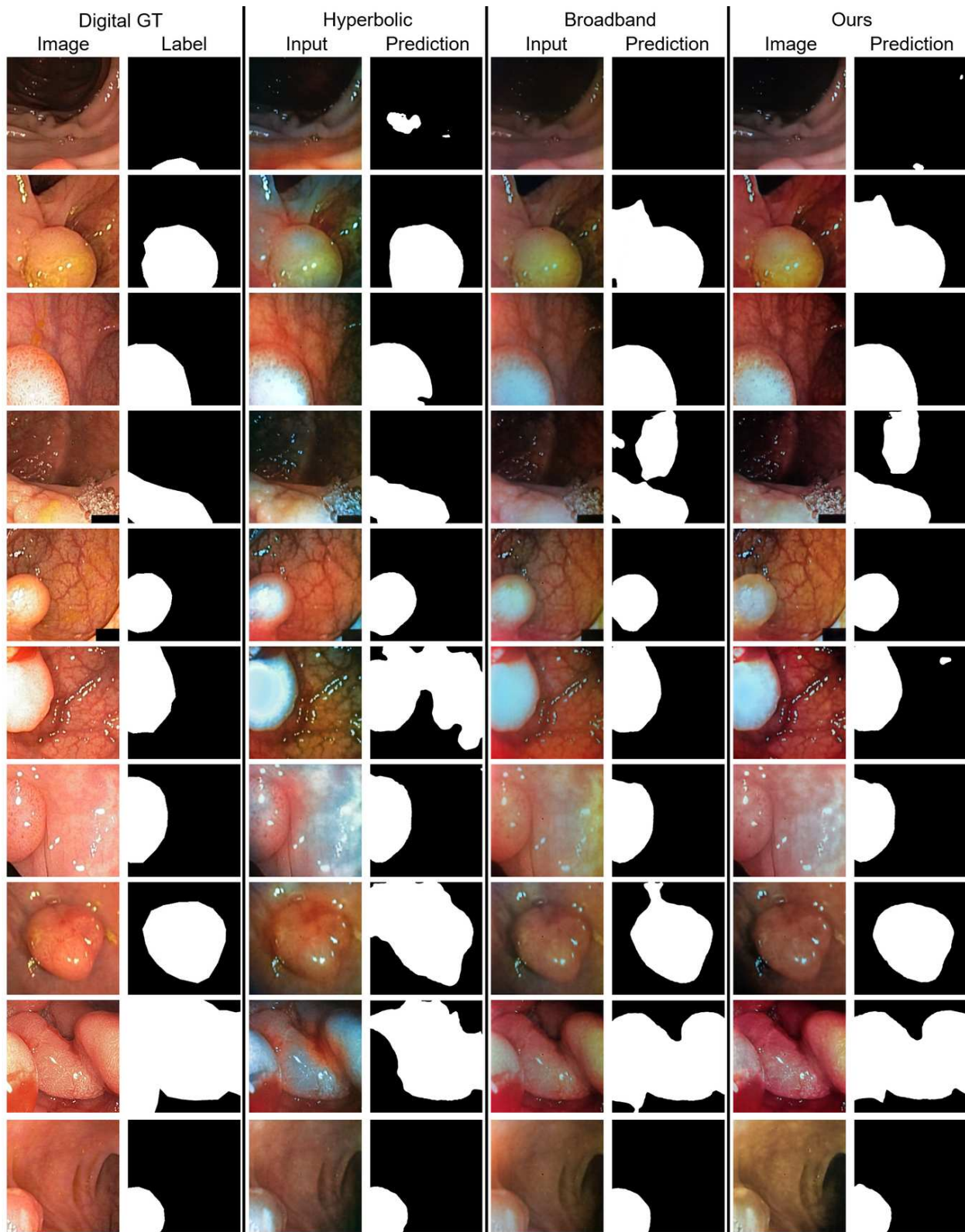




**Figure S17: Visualization of the vision task results on Kvasir-SEG obstructed by blood drops.**



**Figure S18: Visualization of the vision task results on Kvasir-SEG obstructed by blood drops.**



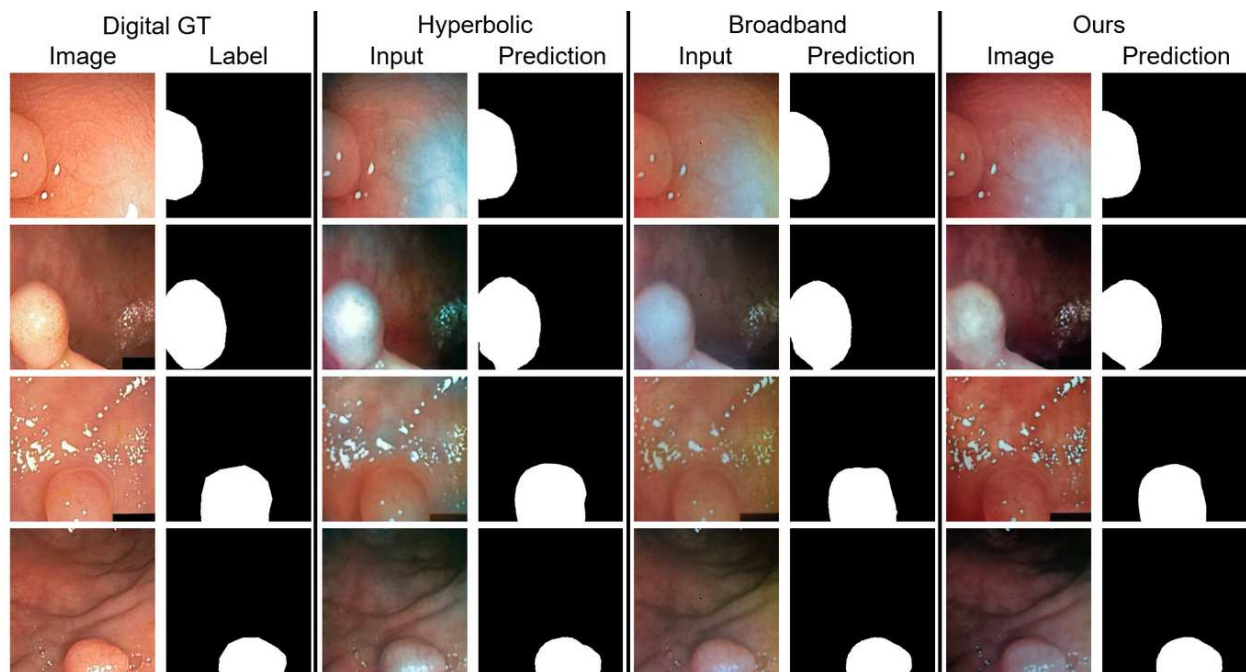


**Figure S20: Visualization of the vision task results on Kvasir-SEG, unobstructed.**

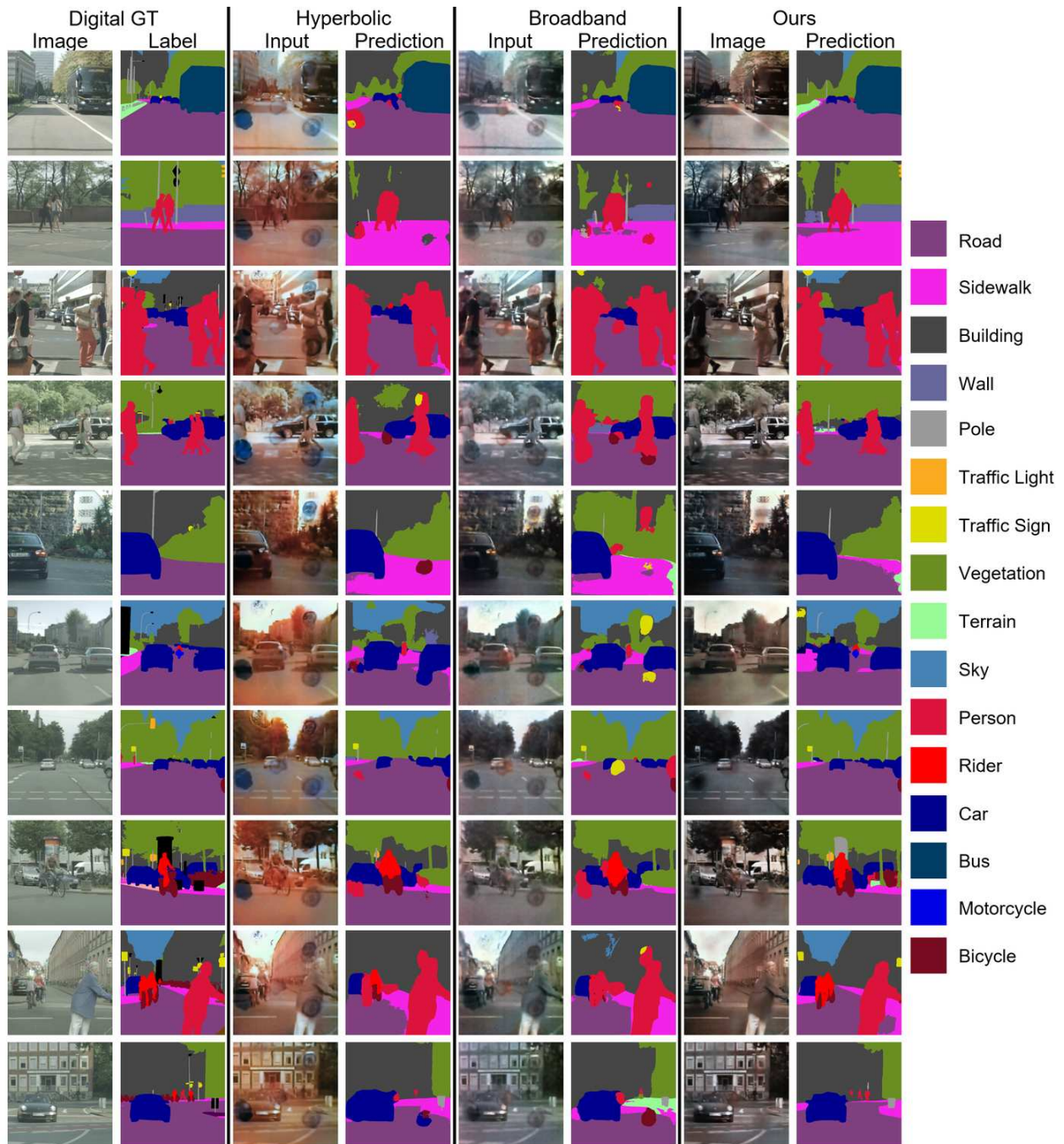
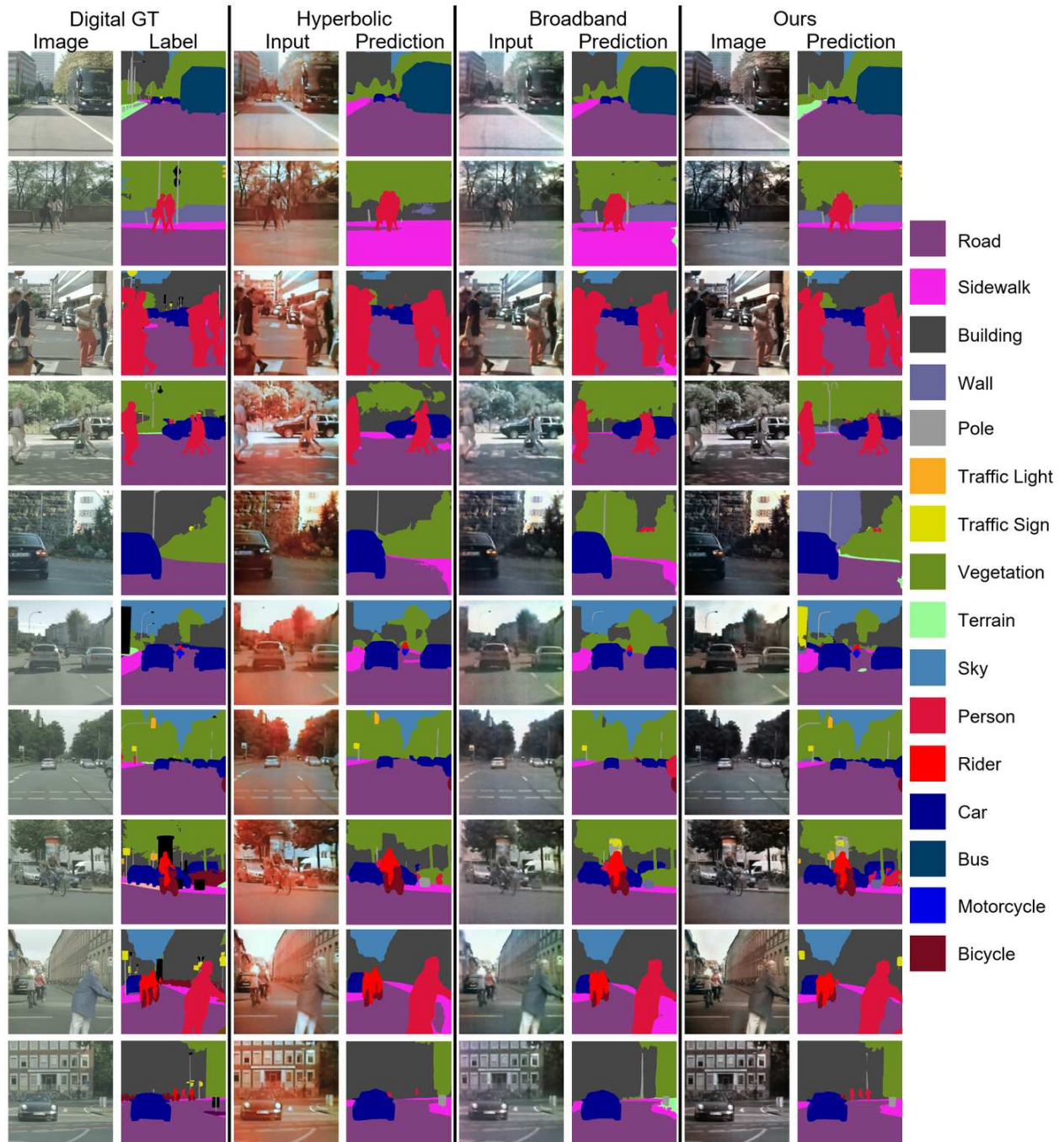


**Figure S21: Visualization of the vision task results on Cityscapes obstructed by dirt occlusions.**



### Supplementary Note 13: Metalens point spread functions and optical MTFs

We plot the wavelength-dependent point spread functions (PSFs) of metalenses: hyperbolic phase metalens (Hyperbolic), learned broadband metalens without the split-spectrum strategy (Broadband), and the learned split-spectrum metalens (Ours), for the light sources at far depth and near depth in Figure S23. The plot reveals the distinct spectro-optical characteristics of our design. The Hyperbolic metalens exhibits a standard diffractive behavior where a sharp PSF is confined strictly to its design wavelength. In contrast, the Broadband metalens effectively reduces chromatic aberration, maintaining consistently sharp far-depth PSFs across the majority of the visible spectrum. Our split-spectrum metalens, however, introduces a unique spectral modulation strategy. It is optimized to maintain sharp characteristic peaks only at specific pass bands for the far-depth sources. Crucially, at these same pass bands, the near-depth PSFs are strongly defocused (blurred). This contrast-sharp far-depth PSFs versus blurred near-depth PSFs—validates our spectral interleaving strategy, which allows the background information to be preserved while optically erasing the obstruction. Furthermore, consistent with claims in the main text and Supplementary Note 1, we observe a spectral shift in the focusing behavior as the depth of the incident light source changes; specifically, as the depth decreases (moving from far depth to near depth), the focused wavelengths shift toward the longer ones (red shift).

**PSF-based MTFs.** We computed the Modulation Transfer Function (MTF) from the measured point spread functions (PSFs) to quantitatively analyze the spectral focusing performance of the fabricated metalenses. Figures S24 and S25 show the characteristics of the Hyperbolic, Broadband, and learned split-spectrum (Ours) metalenses across the visible spectrum. The results highlight distinct spectral behaviors inherent to each design strategy: (i) the hyperbolic-phase metalens exhibits the strongest MTF near its nominal design wavelength (532 nm) and substantially reduced response away from it, (ii) the broadband metalens maintains relatively elevated MTF over a wider spectral range, (iii) our learned split-spectrum metalens shows pronounced MTF enhancement at the filter pass bands while suppressing response in the stop bands. Furthermore, comparing the MTF profiles at  $z = 0.045$  m (near depth) with those at  $z = \infty$  (far depth) reveals a spectral shift towards longer wavelengths. This observed wavelength shift experimentally validates the depth-wavelength symmetry.

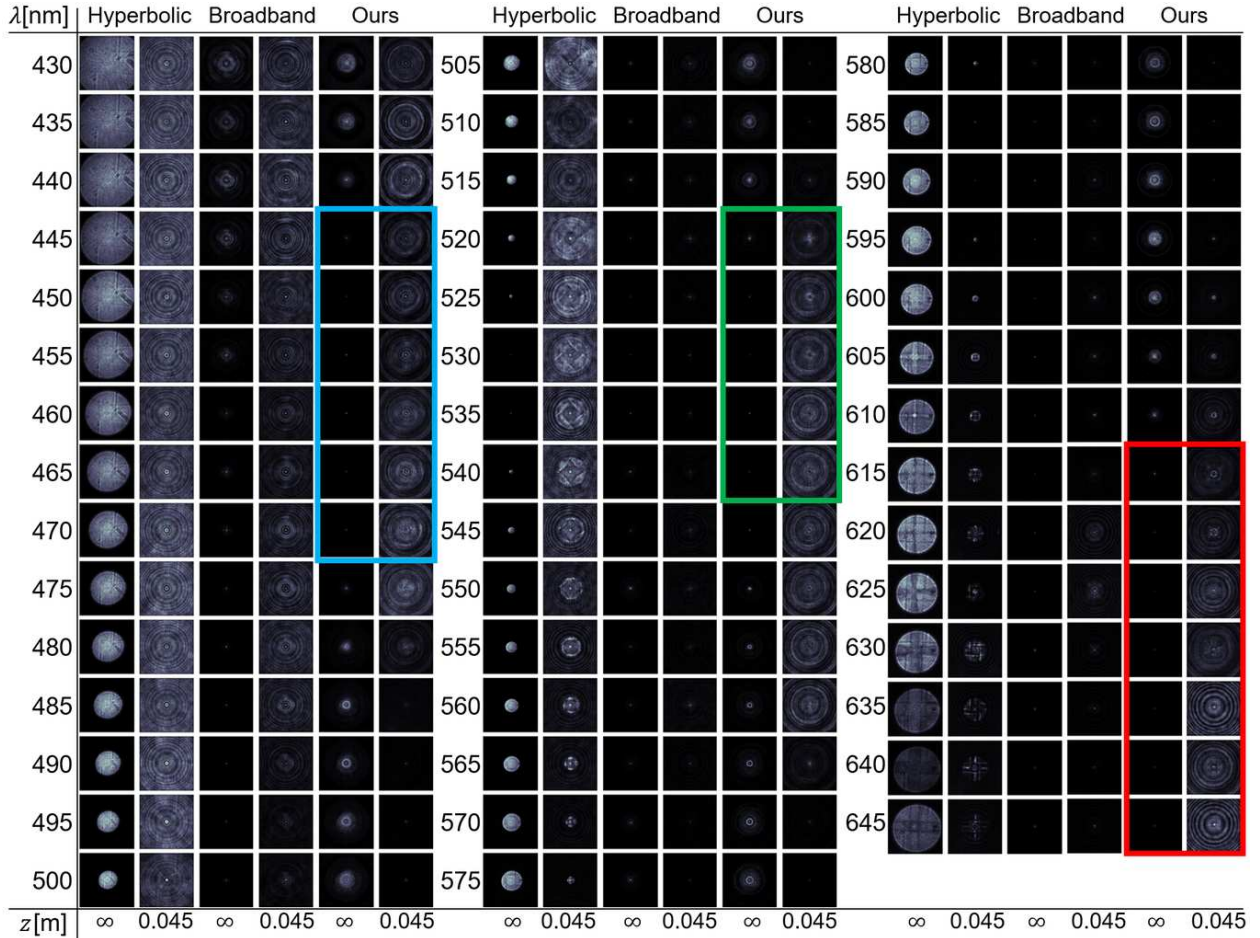


**Figure S23: Wavelength-dependent point spread functions (PSFs) at far and near depths.** We show 2D PSFs for far-depth and near-depth light sources for the three metalenses: hyperbolic phase metalens (Hyperbolic), learned broadband metalens without the split-spectrum strategy (Broadband), and the learned split-spectrum metalens (Ours, split-spectrum). The hyperbolic metalens shows the sharpest far-depth PSF near its nominal design wavelength, while the broadband metalens sustains sharp far-depth PSFs across a wider spectrum. Our far-depth PSFs remain sharp within the designated pass bands, highlighted by blue, green, and red boxes, enabling clear imaging of the background scene. Conversely, the near-depth PSFs within these same colored boxes are significantly blurred. This distinctive behavior—sharp far-depth PSFs and blurred near-depth PSFs within the pass bands—is central to our obstruction cloaking mechanism. We also observe a spectral shift in the focusing behavior as the depth of the incident light source changes; specifically, as the depth decreases (moving from far depth to near depth), the focused wavelengths shift toward the longer ones (red shift).

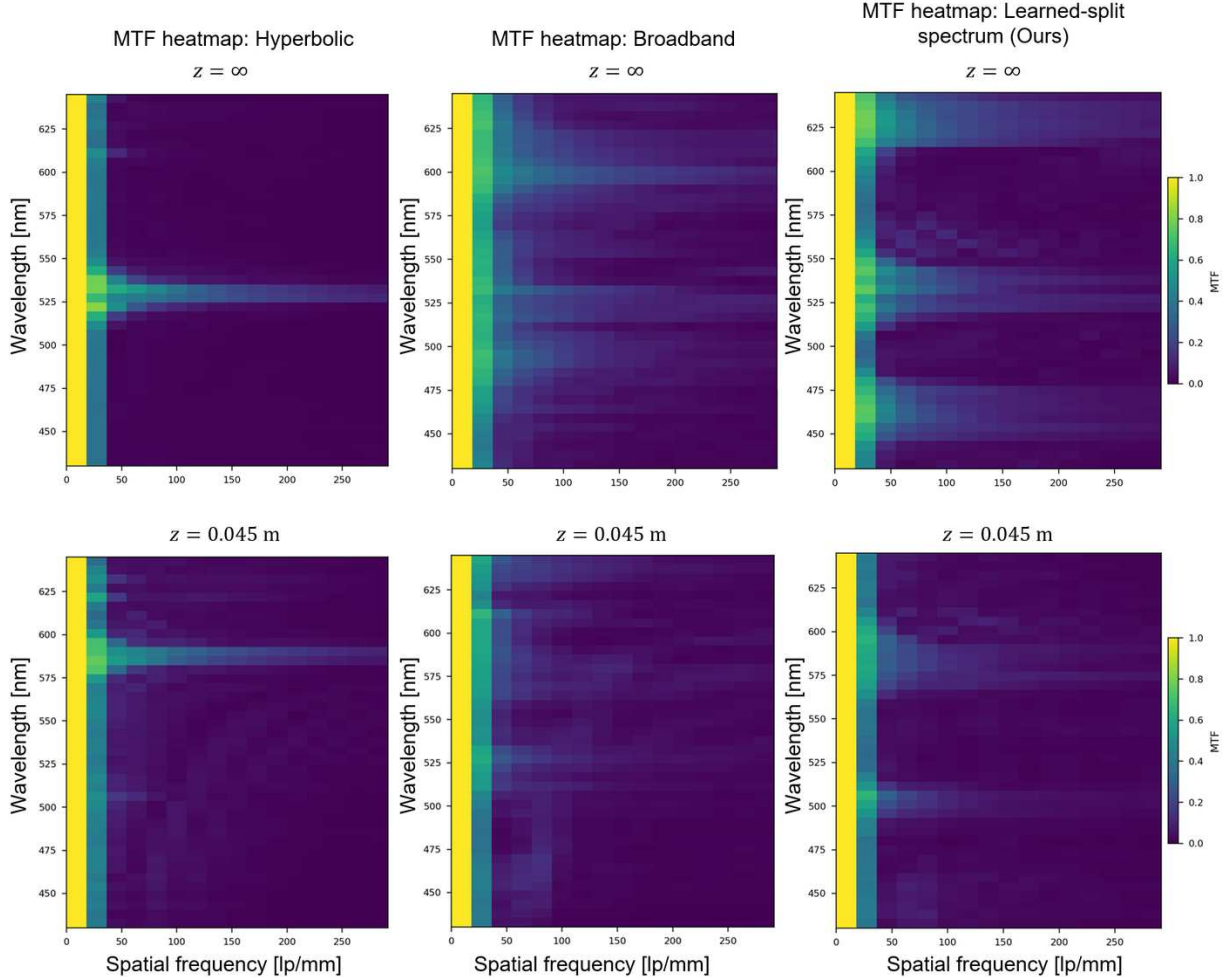


**Figure S24: PSF-based MTF heatmaps across wavelengths.** We show the MTF heatmaps of the near-depth PSFs and far-depth PSFs for three metalenses: hyperbolic phase metalens (Hyperbolic), learned broadband metalens without the split-spectrum strategy (Broadband), and the learned split-spectrum metalens (Ours, split-spectrum). The x-axis is spatial frequency (lp/mm) and the y-axis is wavelength (nm); color indicates MTF. The hyperbolic metalens shows the strongest response near its nominal design wavelength, while the broadband metalens sustains comparatively higher MTFs across a wider spectrum. Our learned split-spectrum metalens exhibits enhanced MTFs at the multi-band spectral filter pass bands and suppressed response in the stop bands, consistent with the split-spectrum acquisition strategy. The high-MTF regions in the far depth ( $z = \infty$ ) maps are spectrally shifted compared to the near depth ( $z = 0.045$  m) maps.

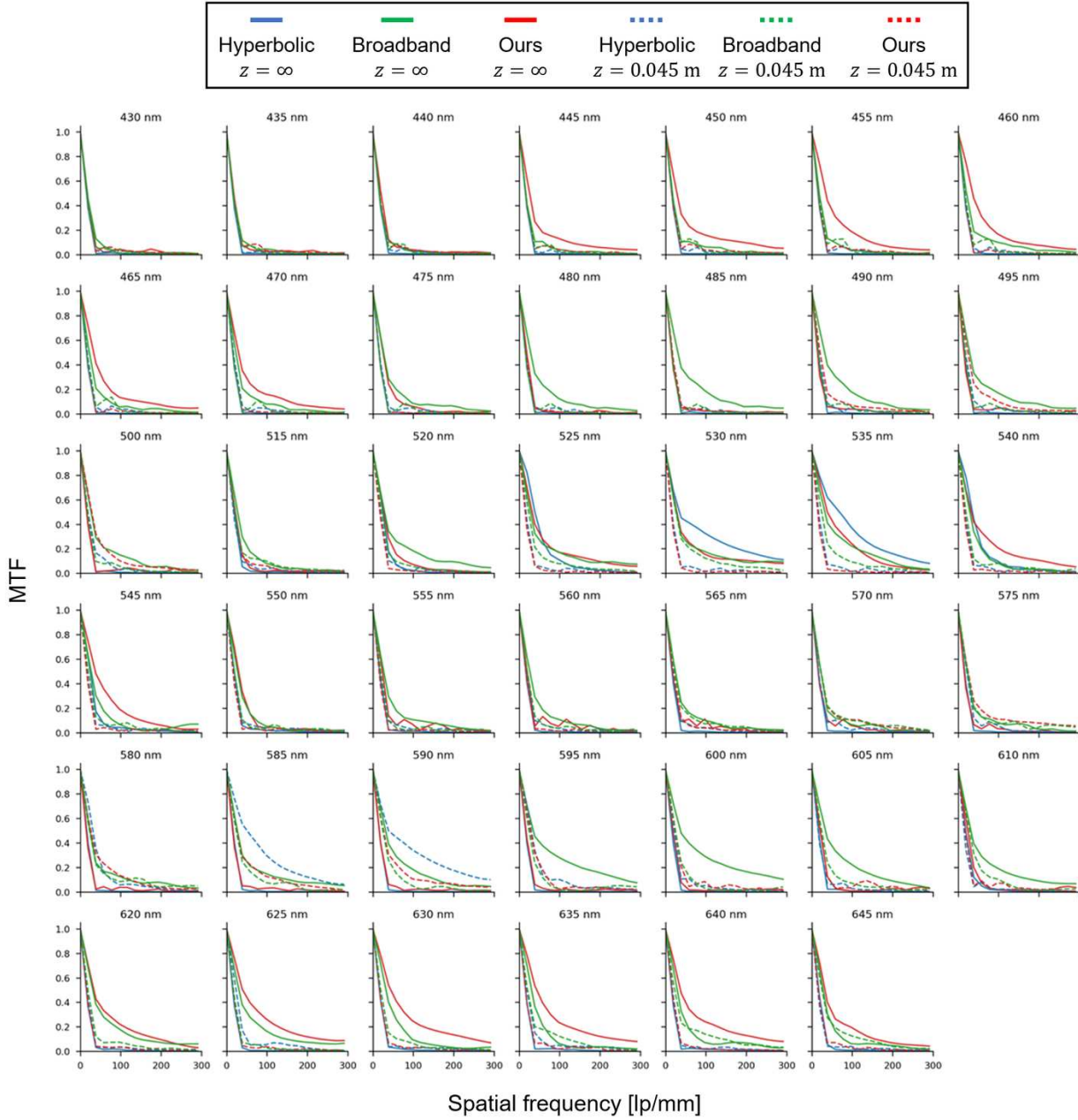


**Figure S25: Radially averaged MTF curves at each measured wavelength.** Each panel plots MTF versus spatial frequency for one wavelength, comparing the three metalenses: hyperbolic phase metalens (Hyperbolic), learned broadband metalens without the split-spectrum strategy (Broadband), and the learned split-spectrum metalens (Ours, split-spectrum). Across wavelengths, the hyperbolic metalens peaks near its design wavelength, the broadband metalens remains relatively consistent over the spectrum, and our split-spectrum metalens provides higher MTFs in the pass bands and suppressed MTFs in the stop bands. The discrepancy between the solid lines ( $z = \infty$ ) and dashed lines ( $z = 0.045$  m) indicates the wavelength shift inherent to the near-depth MTF, which is consistent with the depth-wavelength symmetry.

#### Supplementary Note 14: Slanted edge MTFs

We conduct MTF measurements using the slanted-edge method based on ISO 12233 to provide a comprehensive evaluation of our imaging systems' performance. Our imaging systems consist of a joint hardware-software architecture with an image reconstruction neural network backend. Therefore, PSF-based MTF measurement does not fully reflect our system's imaging contrast fidelity, because it can typically only characterize the optical front-end. Therefore, we measure the holistic performance of the metalens and the restoration network by measuring the MTF directly from the reconstructed images of a slanted edge for each color channel. For a fair comparison and to demonstrate the generalization capability of our system, the checkerboard pattern used for this evaluation was strictly excluded from the image reconstruction network's training dataset.

As shown in Figure S26, our approach is not only effective for obstruction-free imaging, but also excels in high-frequency imaging beyond occluded scenarios. Importantly, this performance is consistent across all color channels, confirming that the learned split-spectrum metalens effectively suppresses chromatic aberrations to enable robust broadband color imaging. In conclusion, the learned split-spectrum metalens can serve as a general-purpose compact camera.

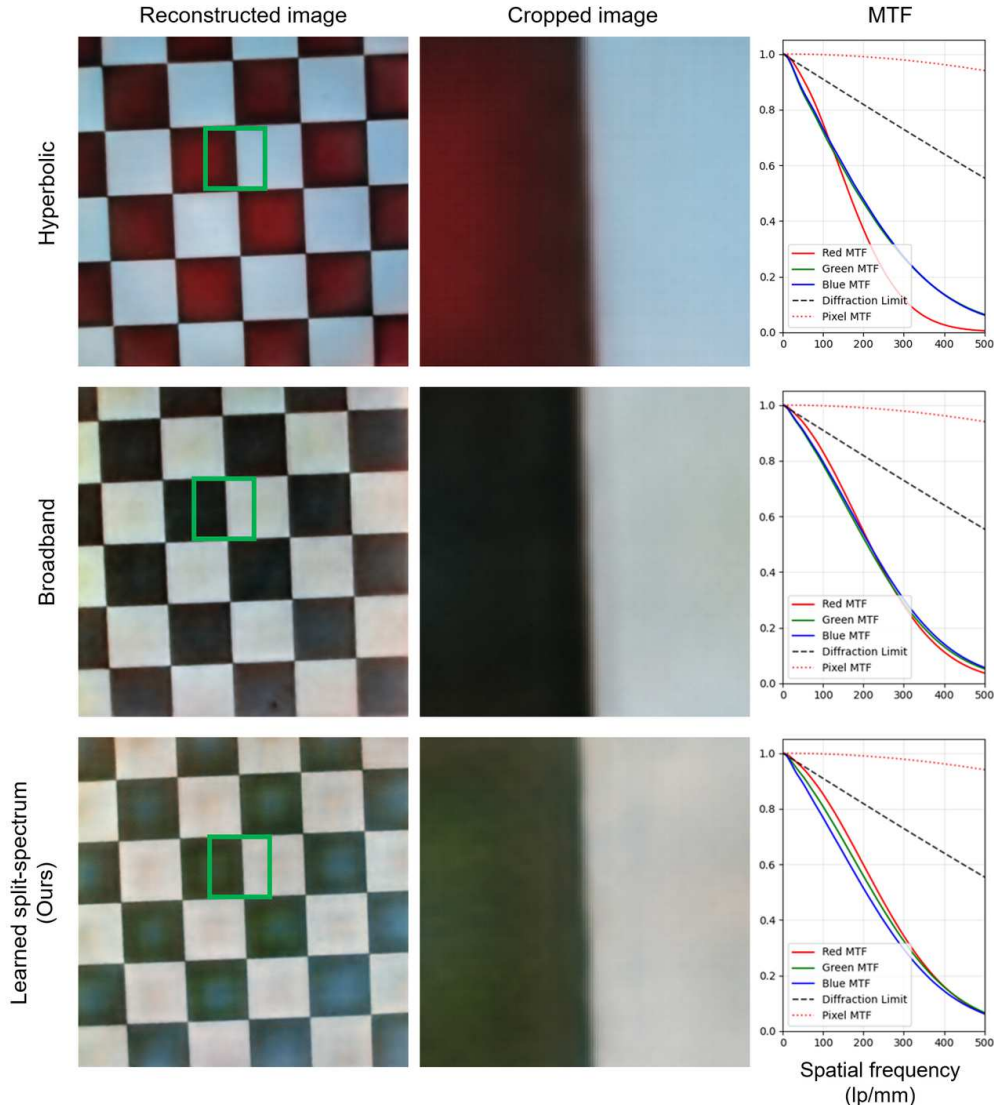


**Figure S26: End-to-end MTF evaluation using the slanted-edge method.** We compare the imaging performance of the three metalenses: hyperbolic phase metalens (Hyperbolic), learned broadband metalens without the split-spectrum strategy (Broadband), and the learned split-spectrum metalens (Ours, split-spectrum), for each color channel of the sensor. The reconstructed checkerboard images (left) and the magnified cropped edges (middle) qualitatively demonstrate the superior sharpness achieved by the joint metalens-neural network systems. The quantitative MTF curves (right) show that our metalens and broadband metalens system maintain higher contrast up to high spatial frequencies, whereas the traditional hyperbolic metalens designs suffer from significant contrast loss for the red channel, reflecting the impact of residual chromatic aberrations. These results confirm that our system delivers high-quality, sharp imaging even for unobstructed scenes. The diffraction limit in the graph refers to the MTF of the diffraction-limited lens of our NA at wavelength 450 nm. The pixel MTF is the Nyquist sampling limit of the imaging systems.

### Supplementary Note 15: Additional experimental imaging results

This section provides additional qualitative results from our experimental prototype, covering (i) high-resolution printed targets and (ii) real-world 3D scenes, or in-the-wild scenes. As discussed in the main text and Supplementary Note 5, we utilized high-resolution printed images from the DIV2K dataset for quantitative performance evaluation. Unlike digital display inputs (e.g., LCD or OLED screens), which typically exhibit narrow spectral peaks (Figure S8), printed images under LED illumination reflect a continuous and broader spectrum. This is essential for accurately evaluating broadband imaging capabilities. Figures S27 and S28 show the qualitative comparisons of these printed scene captures. To demonstrate the imaging capability of our system beyond planar targets, we further present imaging results on real-world 3D objects (in-the-wild scenes). Figure S29 shows the results captured under ambient indoor lighting conditions with near-depth obstructions.

As shown in the figures, the images captured by the hyperbolic and broadband metalenses exhibit severe chromatic aberrations and distinct artifacts from the obstructions, even after the image reconstruction. In contrast, our learned split-spectrum metalens effectively suppresses the obstruction artifacts in the raw capture, enabling the reconstruction network to recover high-fidelity details and accurate colors that closely match the ground truth.

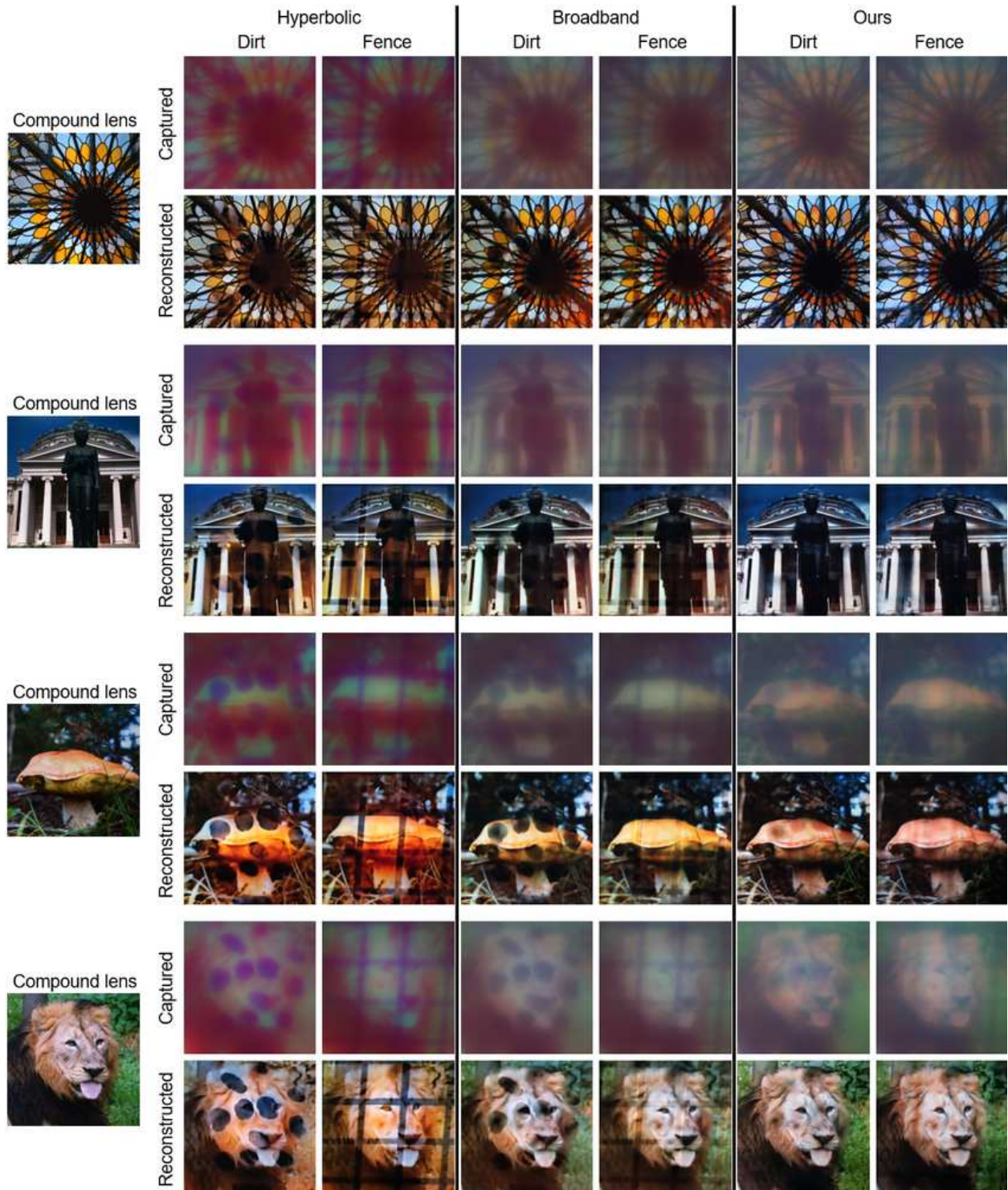


**Figure S27: Qualitative comparisons under representative obstructions (dirt and fence).** We visualize the captured raw metalens image under dirt/fence and the reconstructed output produced by the corresponding method.

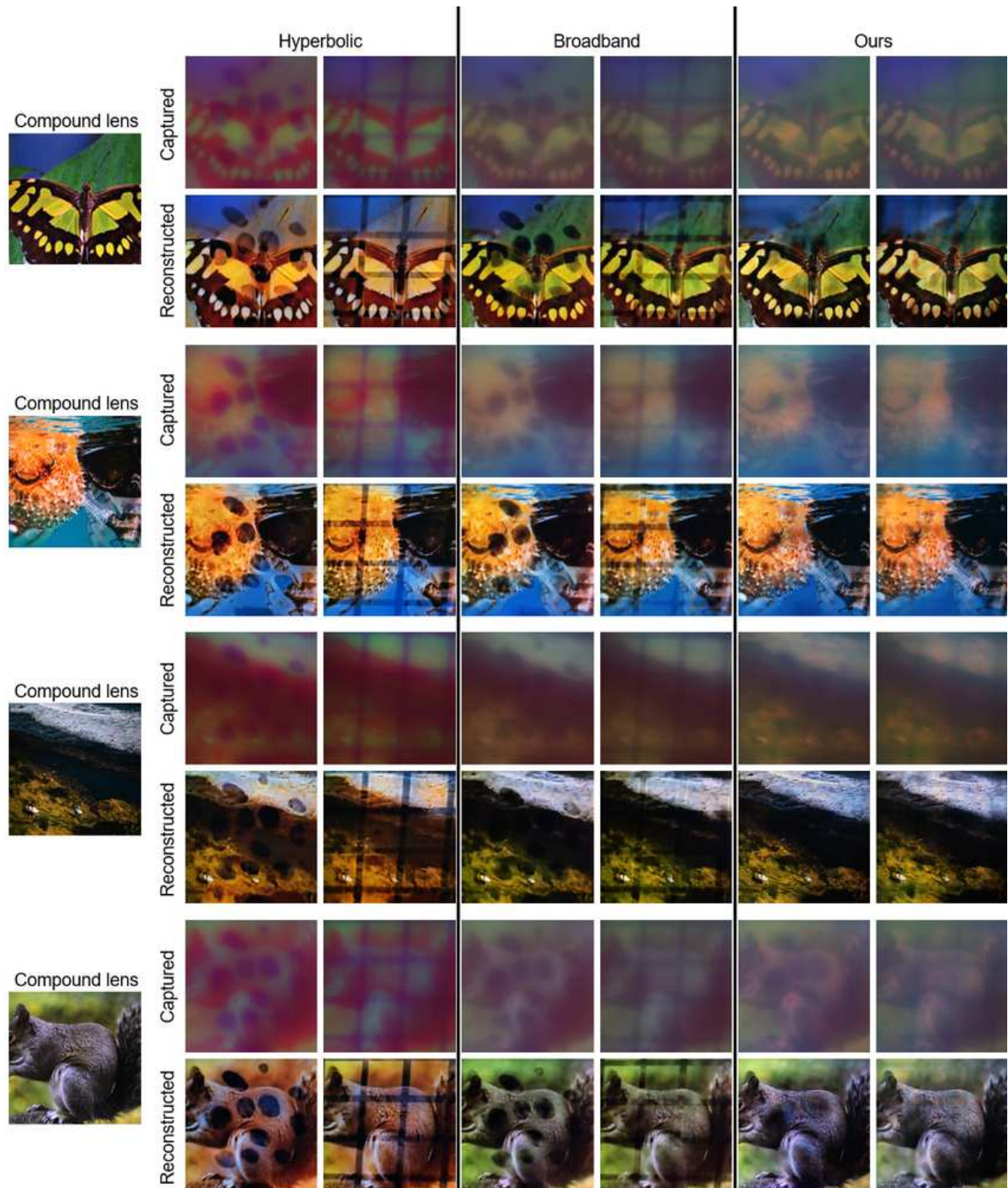


**Figure S28: Additional qualitative results for dirt and fence obstructions.** We visualize the captured raw metalens image under dirt/fence and the reconstructed output produced by the corresponding method.

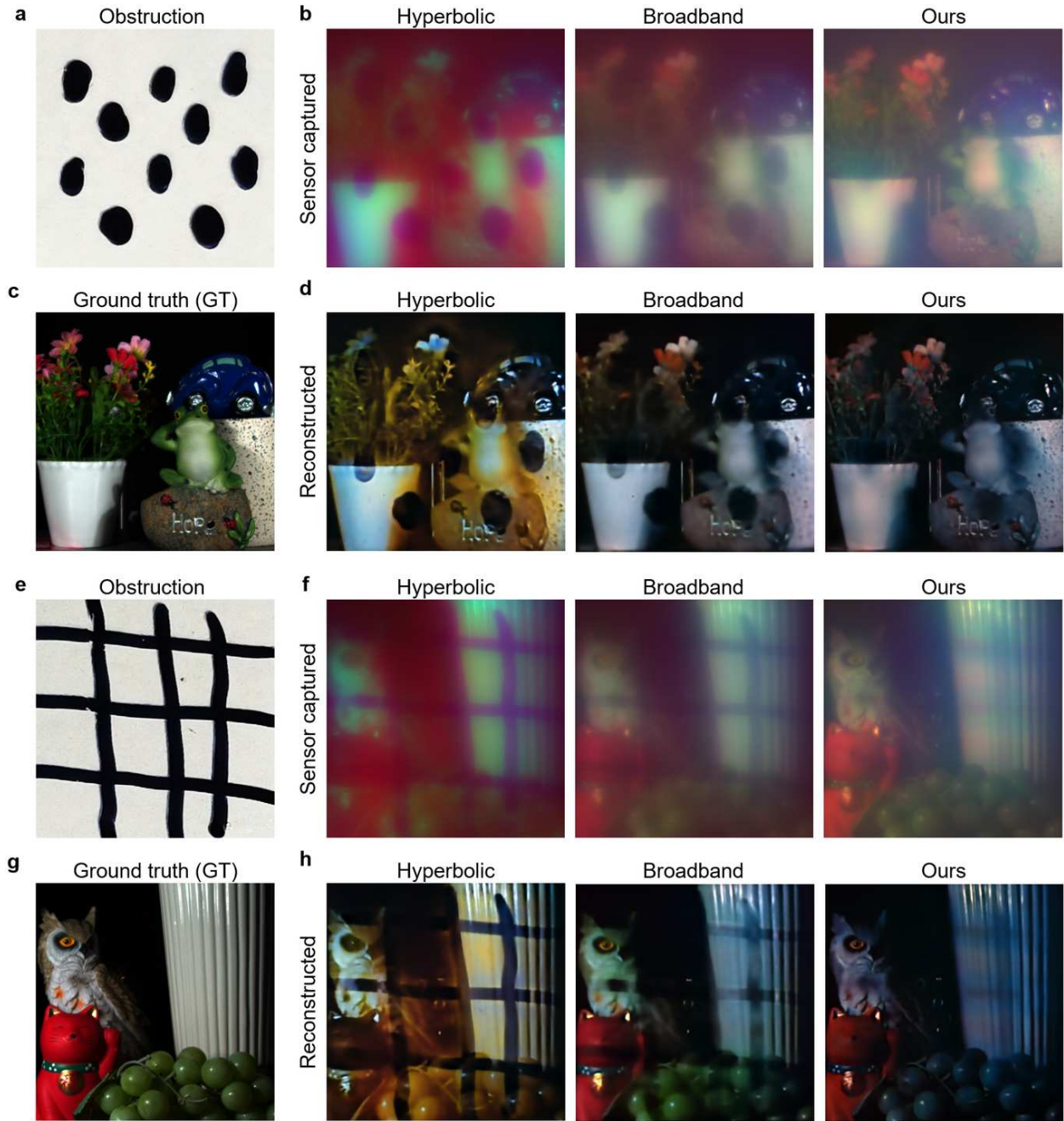


**Figure S29: Additional in-the-wild qualitative results.** **a, e** Near-depth obstruction patterns. **b, f** Raw sensor images captured under the obstruction for the three metalens designs. **c, g** Ground-truth (GT) unobstructed reference images captured with a compound lens with  $f = 8$  mm (two times longer than metalenses) for better object plane resolution. **d, h** Reconstructed images using the neural network trained for each metalens. **b, d, f, h** Our metalens achieves superior performance across all conditions.

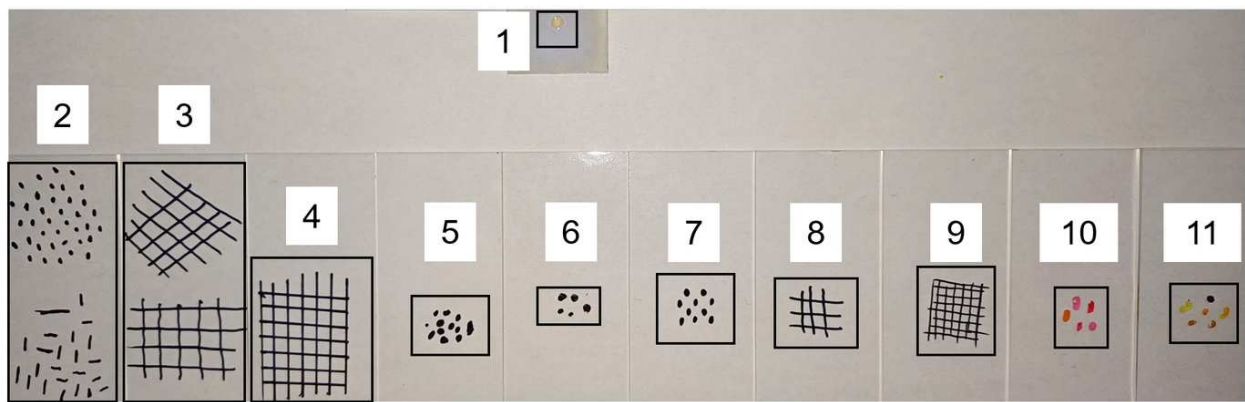


**Figure S30: Obstructions used for the evaluations and the neural network training.**  
 We show the images of obstructions used in this study. Our metalens is shown for the relative size comparison between the metalens and obstructions. **1** Our learned split-spectrum metalens for relative size comparison between the lens and obstructions. **2, 3** Obstructions used for the image reconstruction network training. **4, 5** Obstructions used for the image metric measurements. **6, 7, 8** Obstructions used for the in-the-wild scene imaging. **9, 10,** **11** Obstructions used for the computer vision tasks imaging.

## References

1. Matsushima, K. & Shimobaba, T. Band-limited angular spectrum method for numerical simulation of free-space propagation in far and near fields. *Optics express* **17**, 19662–19673 (2009).
2. Goodman, J. W. *Introduction to Fourier optics* (Roberts and Company publishers, 2005).
3. Chang, S. *et al.* Achromatic metalenses for full visible spectrum with extended group delay control via dispersion-matched layers. *Nature communications* **15**, 9627 (2024).
4. de Wit, J., Cussiol, F., Caglayan, H. & Gómez Rivas, J. Diffraction and dispersion effects on the wavelength dependence of the focal length of metalenses. *Applied Optics* **64**, 3598–3604 (2025).
5. Tseng, E. *et al.* Neural nano-optics for high-quality thin lens imaging. *Nature communications* **12**, 6493 (2021).
6. Colburn, S., Chu, Y., Shilzerman, E. & Majumdar, A. Optical frontend for a convolutional neural network. *Applied optics* **58**, 3179–3186 (2019).
7. Huang, L., Whitehead, J., Colburn, S. & Majumdar, A. Design and analysis of extended depth of focus metalenses for achromatic computational imaging. *Photonics Research* **8**, 1613–1623 (2020).
8. Fröch, J. E. *et al.* Beating spectral bandwidth limits for large aperture broadband nano-optics. *Nature communications* **16**, 3025 (2025).
9. Tan, S., Yang, F., Boominathan, V., Veeraraghavan, A. & Naik, G. V. 3d imaging using extreme dispersion in optical metasurfaces. *Acs Photonics* **8**, 1421–1429 (2021).
10. Xu, H. *et al.* A polarization-independent and broadband achromatic gallium nitride metalens based on extended depth of focus. In *Fourth International Computational Imaging Conference (CITA 2024)*, vol. 13542, 1029–1037 (SPIE, 2025).
11. Bayati, E. *et al.* Inverse designed extended depth of focus meta-optics for broadband imaging in the visible. *Nanophotonics* **11**, 2531–2540 (2022).
12. Shrestha, S., Overvig, A. C., Lu, M., Stein, A. & Yu, N. Broadband achromatic dielectric metalenses. *Light: Science & Applications* **7**, 85 (2018).
13. Presutti, F. & Monticone, F. Focusing on bandwidth: achromatic metalens limits. *Optica* **7**, 624–631 (2020).
14. Chen, W. T. *et al.* A broadband achromatic metalens for focusing and imaging in the visible. *Nature nanotechnology* **13**, 220–226 (2018).

15. Chen, W. T., Zhu, A. Y., Sisler, J., Bharwani, Z. & Capasso, F. A broadband achromatic polarization-insensitive metalens consisting of anisotropic nanostructures. *Nature communications* **10**, 355 (2019).
16. Hu, Y. *et al.* Asymptotic dispersion engineering for ultra-broadband meta-optics. *nature communications* **14**, 6649 (2023).
17. Hirohashi, Y. *et al.* Removal of image obstacles for vehicle-mounted surrounding monitoring cameras by real-time video inpainting. In *Proceedings of the IEEE/CVF Conference on Computer Vision and Pattern Recognition Workshops*, 214–215 (2020).
18. Zhang, J., Fukuda, T. & Yabuki, N. Automatic object removal with obstructed façades completion using semantic segmentation and generative adversarial inpainting. *IEEE Access* **9**, 117486–117495 (2021).
19. Jonna, S., Medhi, M. & Sahay, R. R. Deep generative adversarial network for occlusion removal from a single image. *arXiv preprint arXiv:2409.13242* (2024).
20. Jonna, S., Satapathy, S. & Sahay, R. R. Stereo image de-fencing using smartphones. In *2017 IEEE international conference on acoustics, speech and signal processing (ICASSP)*, 1792–1796 (IEEE, 2017).
21. Zhu, C., Wan, R., Tang, Y. & Shi, B. Occlusion-free scene recovery via neural radiance fields. In *Proceedings of the IEEE/CVF Conference on Computer Vision and Pattern Recognition*, 20722–20731 (2023).
22. Liu, Y.-L., Lai, W.-S., Yang, M.-H., Chuang, Y.-Y. & Huang, J.-B. Learning to see through obstructions. In *Proceedings of the IEEE/CVF Conference on Computer Vision and Pattern Recognition*, 14215–14224 (2020).
23. Xue, T., Rubinstein, M., Liu, C. & Freeman, W. T. A computational approach for obstruction-free photography. *ACM Transactions on Graphics (TOG)* **34**, 1–11 (2015).
24. Tsogkas, S., Zhang, F., Jepson, A. & Levinstein, A. Efficient flow-guided multi-frame de-fencing. In *Proceedings of the IEEE/CVF Winter Conference on Applications of Computer Vision*, 1838–1847 (2023).
25. Chugunov, I., Shustein, D., Yan, R., Lei, C. & Heide, F. Neural spline fields for burst image fusion and layer separation. In *Proceedings of the IEEE/CVF Conference on Computer Vision and Pattern Recognition*, 25763–25773 (2024).
26. Levoy, M. *et al.* Synthetic aperture confocal imaging. *ACM Transactions on Graphics (ToG)* **23**, 825–834 (2004).
27. Joshi, N., Avidan, S., Matusik, W. & Kriegman, D. J. Synthetic aperture tracking: Tracking through occlusions. In *2007 IEEE 11th International Conference on Computer Vision*, 1–8 (IEEE, 2007).

28. Pei, Z., Chen, X. & Yang, Y.-H. All-in-focus synthetic aperture imaging using image matting. *IEEE Transactions on Circuits and Systems for Video Technology* **28**, 288–301 (2016).
29. Pei, Z. *et al.* Occluded-object 3d reconstruction using camera array synthetic aperture imaging. *Sensors* **19**, 607 (2019).
30. Shi, Z. *et al.* Seeing through obstructions with diffractive cloaking. *ACM Transactions on Graphics (TOG)* **41**, 1–15 (2022).
31. Berry, M. V. Quantal phase factors accompanying adiabatic changes. *Proceedings of the Royal Society of London. A. Mathematical and Physical Sciences* **392**, 45–57 (1984).
32. Agustsson, E. & Timofte, R. Ntire 2017 challenge on single image super-resolution: Dataset and study. In *The IEEE Conference on Computer Vision and Pattern Recognition (CVPR) Workshops* (2017).
33. Perlin, K. An image synthesizer. *ACM Siggraph Computer Graphics* **19**, 287–296 (1985).
34. Chen, M., Zhao, S., Liu, H. & Cai, D. Adversarial-learned loss for domain adaptation. In *Proceedings of the AAAI conference on artificial intelligence*, vol. 34, 3521–3528 (2020).
35. Chen, L.-C., Zhu, Y., Papandreou, G., Schroff, F. & Adam, H. Encoder-decoder with atrous separable convolution for semantic image segmentation. In *Proceedings of the European conference on computer vision (ECCV)*, 801–818 (2018).
36. Loshchilov, I. & Hutter, F. Decoupled weight decay regularization. *arXiv preprint arXiv:1711.05101* (2017).
37. Loshchilov, I. & Hutter, F. Sgdr: Stochastic gradient descent with warm restarts. *arXiv preprint arXiv:1608.03983* (2016).
38. Kim, W. *et al.* Paramisp: Learned forward and inverse isps using camera parameters. In *Proceedings of the IEEE/CVF Conference on Computer Vision and Pattern Recognition (CVPR)*, 26067–26076 (2024).
39. Ronneberger, O., Fischer, P. & Brox, T. U-net: Convolutional networks for biomedical image segmentation. In *International Conference on Medical image computing and computer-assisted intervention*, 234–241 (Springer, 2015).
40. Woo, S., Park, J., Lee, J.-Y. & Kweon, I. S. Cbam: Convolutional block attention module. In *Proceedings of the European conference on computer vision (ECCV)*, 3–19 (2018).
41. Vaswani, A. *et al.* Attention is all you need. *Advances in neural information processing systems* **30** (2017).
42. Mildenhall, B. *et al.* Nerf: Representing scenes as neural radiance fields for view synthesis. *Communications of the ACM* **65**, 99–106 (2021).

43. Zhang, R., Isola, P., Efros, A. A., Shechtman, E. & Wang, O. The unreasonable effectiveness of deep features as a perceptual metric. In *Proceedings of the IEEE conference on computer vision and pattern recognition*, 586–595 (2018).
44. Engelberg, J. & Levy, U. Generalized metric for broadband flat lens performance comparison. *Nanophotonics* **11**, 3559–3574 (2022).
45. Potje, G., Cadar, F., Araujo, A., Martins, R. & Nascimento, E. R. Xfeat: Accelerated features for lightweight image matching. In *Proceedings of the IEEE/CVF Conference on Computer Vision and Pattern Recognition*, 2682–2691 (2024).
46. Fischler, M. A. & Bolles, R. C. Random sample consensus: a paradigm for model fitting with applications to image analysis and automated cartography. *Communications of the ACM* **24**, 381–395 (1981).
47. Khanam, R. & Hussain, M. Yolov11: An overview of the key architectural enhancements. *arXiv preprint arXiv:2410.17725* (2024).
48. Zhu, P. *et al.* Detection and tracking meet drones challenge. *IEEE Transactions on Pattern Analysis and Machine Intelligence* **44**, 7380–7399 (2021).
49. Zhao, X. *et al.* M2snet: Multi-scale in multi-scale subtraction network for medical image segmentation. *arxiv* 2023. *arXiv preprint arXiv:2303.10894* (2).
50. Pogorelov, K. *et al.* Kvasir: A multi-class image dataset for computer aided gastrointestinal disease detection. In *Proceedings of the 8th ACM on Multimedia Systems Conference*, 164–169 (2017).
51. Wang, W. *et al.* Internimage: Exploring large-scale vision foundation models with deformable convolutions. In *Proceedings of the IEEE/CVF conference on computer vision and pattern recognition*, 14408–14419 (2023).
52. Cordts, M. *et al.* The cityscapes dataset for semantic urban scene understanding. In *Proc. of the IEEE Conference on Computer Vision and Pattern Recognition (CVPR)* (2016).